Spring 1-1-2012

Resonant and Soliton Transport of Ultracold Atoms on Optical Lattices

Chester Philipp Rubbo
University of Colorado at Boulder, chester.rubbo@gmail.com

Resonant and Soliton Transport of Ultracold Atoms on Optical Lattices

by

Chester Philipp Rubbo

B.S., University of Virginia, 2005

A thesis submitted to the

Faculty of the Graduate School of the

University of Colorado in partial fulfillment

of the requirements for the degree of

Doctor of Philosophy

Department of Physics

2012

This thesis entitled:
Resonant and Soliton Transport of Ultracold Atoms on Optical Lattices
written by Chester Philipp Rubbo
has been approved for the Department of Physics

Ana Maria Rey

Murray J. Holland

Date

The final copy of this thesis has been examined by the signatories, and we find that both the content and the form meet acceptable presentation standards of scholarly work in the above mentioned discipline.

Rubbo, Chester Philipp (Ph.D., Physics)

Resonant and Soliton Transport of Ultracold Atoms on Optical Lattices

Thesis directed by Prof. Ana Maria Rey

In this thesis, we present a theoretical study of the dynamics of strongly interacting ultracold atoms in optical lattices. At ultracold temperatures, the dynamics cannot be described classically, but instead, must take into account quantum effects. Here, our focus is on transport and precision measurement. We use exact analysis of few-body systems and mean field analysis. For larger systems, we use a numerical approach called the density matrix renormalization group (DMRG) method which is considered an efficient computational tool for the quantum evolution of 1D systems.

After introducing basic concepts, we treat the motional properties of particles in a tilted lattice in a regime where the inter-particle interactions are resonant with the linear potential. In this regime, the dynamics is described by an Ising model with a transverse field which is a basic system to study quantum magnetism and quantum phase transitions. We introduce analytical and numerical methods to draw a simple picture of the dynamics. This helps us to formulate a slinky-like transport scheme that provides full control of the motional direction of particles.

After a study of transport on a tilted lattice, we treat the transport of nonlinear waves in strongly interacting systems. These nonlinear waves are called solitons, which are described as local perturbations of a medium that survive after collisions. We identify two species of classical soliton solutions in our system and study their stability under quantum evolution via DMRG.

We shift focus from the dynamics related to transport and turn to precision measurements in optical lattice clocks. Here, we investigate one aspect of their limitations which is due to collisions of atoms loaded onto a single site. These collisions introduce a frequency shift in the clock measurement. We provide a microscopic description of the origin of this frequency shift. Our results have motivated improvement in the accuracy and precision of next generation optical lattice clocks.

Dedication

To my family and friends.

Acknowledgements

I would like to acknowledge the people who have left an indelible mark during my stint in graduate school.

I would first like to thank my family for their constant encouragement and support. I also feel very blessed for having shared my most trying moments with Nicole. She has been a loving companion, confidant, and best friend. I have undoubtedly become a better man with her by my side. Special thanks go out to the Dallabettas and Sokols for being the best surrogate families in Colorado. In addition, I would like to thank my friends: I would like to thank Eduardo Calleja for the sweat and tears from the many golf and basketball duels over the years. I am grateful for having Hussain Zaidi endure my long-winded ramblings during our phone correspondence, and I would like to thank Brian Burke for his guitar mentorship.

I would also like to acknowledge Michael Dubson and the Physics department for providing a substantial part of my funding.

I am very grateful for the advisorship of Ana Maria Rey. I have the highest admiration for her extensive knowledge and expertise in the field. Finally, I would like to thank my colleagues. In particular, I am greatly indebted to Salvatore Manmana. His guidance has been the most influential. I attribute his tutelage and unrivaled meticulosity to the completion of the works presented in this thesis.

Contents

Chapter

Figures

Figure

Chapter 1

Introduction

When cooled to temperatures typically below a microkelvin a cloud of atoms can no longer be looked upon classically as acting like billiard balls. A picture dominated by quantum mechanics is necessary to model the behavior of these ultracold atoms. The study and exploration of this regime has advanced our knowledge of the emergence of quantum phases of matter, and furthermore, has led to the advancement in high precision metrology. For this reason, ultracold atoms have garnered excitement in the field. It is then important to study ultracold atomic systems which are created by advanced laser cooling and trapping methods [1]. In these systems, atoms are cooled and trapped until their inter-particle separation is comparable to their thermal de Broglie wavelength, resulting in the emergence of quantum phases of matter [2]. This was first demonstrated in the Bose-Einstein condensation (BEC) of a gas of bosonic atoms in 1995 [3]. Since then, also fermionic atomic systems have reached quantum degeneracy [4]. Beyond weak interactions featured in the gaseous condensates, more exotic quantum phases occur in strongly correlated systems. The strongly correlated regime is where mean field theory fails to describe the behavior of these systems and occurs when the mean interaction energy of the system is large compared to its kinetic energy. A way to reach this regime is by trapping atoms in an optical lattice: a periodic potential increases the atom's effective mass in dilute vapors, thereby reducing the kinetic energy and increasing the role of interactions.

In this thesis, we study the dynamics of ultracold atoms on optical lattices related to topics in transport and precision measurement. In particular, we investigate the motional dynamics

of strongly interacting bosons on a tilted optical lattice, the quantum evolution of solitons in a strongly interacting system, and the collision dynamics which occurs in optical lattice clocks. The pervading approach to studying the dynamics of these large many-body systens is to first develop a simple picture from either using approximate methods like mean field analysis or exact methods on small systems, and then due to analytical limitations, we apply numerical methods to simulate the dynamics of large many-body systems.

The thesis is structured as follows. In Chapter 2, we review the basic properties of optical lattices and the behavior of a single particle in the presence of a periodic potential. The dynamics of an atom trapped in an optical lattice simulates the physics of an electron in a periodic potential formed by an array of nuclei inside a crystal. However, ultracold atoms on optical lattices, as opposed to their condensed matter counterparts, are without the imperfections like defects and impurities typical for condensed matter systems. Furthermore, the parameters of an optical lattice are easily controlled: the periodicity of the lattice structure is given by the laser beam frequency and the depth of the lattice is controlled by the intensity of the laser beam. It was shown that the dynamics of ultracold bosonic atoms in an optical lattice can be described by a Bose-Hubbard model [5, 6]. This model, which captures the competition between the kinetic energy and the repulsive local interaction, displays a quantum phase transition between a superfluid ground state and a Mott insulator ground state. We present an overview of this model and the quantum phase transition associated with it. A seminal experiment using ^{87}Rb bosonic atoms in an optical lattice demonstrated this transition over a decade ago [7], and since then, the experiment has spurred theoretical investigations of ultracold atoms in optical lattices as quantum simulators of strongly correlated condensed matter systems [8, 9, 10, 11, 12].

In Chapter 3, we review two numerical computational methods that have facilitated the study of large many-body systems. An exact numerical analysis of many-body models is nearly impossible due to the exponentially large growth of the Hilbert space with system size. Therefore, it was important to devise a numerical approximation method for the study of many-body systems. We first describe one such method called the the density matrix renormalization group method

devised by S. R. White in 1992 for a nearly exact calculation of ground states of 1D systems [13, 14]. Though initially formulated for static calculations, the DMRG method was later extended for time-evolved dynamics. We then describe one successful time evolution method which was developed by Vidal, the so-called time-evolving block decimation (TEBD) algorithm [15, 16].

In Chapter 4, we first review the single particle picture of an electron in a periodic potential under the influence of externally applied static fields. The motion is described by periodic oscillations in momentum and position called Bloch oscillation (BO). However, due to dissipative effects from scattering events, BOs are difficult to observe in crystalline solids. Optical lattices, on the other hand, are free from these dissipative effects, thereby motivating much effort in using ultracold atomic systems to mimic the behavior of a charged particle in a periodic potential under an applied field. Since the atoms we consider here have neutral charge, alternative methods such as accelerating the optical lattice, orienting it vertically, or applying a magnetic field gradient are required to simulate the effect of an applied electric field on an electron. Employing these methods, BOs have been experimentally observed with ultracold atoms [17, 18]. Since the demonstration of this coherent motion, additional methods using time-varying applied fields have been developed to control transport of atoms on optical lattices [19, 20, 21, 22]. Transport in many-body systems has been another interesting area of study. For instance, recent developments in the simulation of electronic semiconductor devices (called atomtronics) required strong interactions in the proposed implementation of atom-based diodes and transistors [23, 24]. We will present a transport scheme in a strongly interacting system of atoms on an optical lattice modelled by the Bose-Hubbard model. After initially loading atoms in a selective manner afforded by the control of initial state preparation in these systems, we show that a periodically driven field can allow for directional control and enhancement in transport.

In Chapter 5, we present another aspect of transport in ultracold atomic systems. Instead of applying external fields to induce motion, we consider traveling wave solutions inherent in many-body systems. These wave solutions are called solitons, and nonlinearities in the system are necessary for their existence. They are described as being permanent, local perturbations which

remain fully intact after collisions. Solitons have been a rich topic of study and have applications in information transfer across systems relevant for fields like telecommunications and information processing [25, 26, 27]. Ultracold atomic systems exhibit nonlinear behavior due to the presence of interatomic interactions and have been shown to support solitons in BECs [28]. This has opened up an alternative approach to analyzing solitons in other nonlinear media [29]. We describe the mean field soliton solutions that exist in an inherently nonlinear system of strongly interacting particles on an optical lattice. We demonstrate the stability of the solitons when they are subjected to quantum fluctuations.

In Chapter 6, we shift focus from the study of transport to the study of dynamics related to precision measurement. The improvement of laser stability and the recent advancement of technology in fequency measurement [30, 31, 32] have increased the precision of optical clocks which now rival the precision of current Cesium-based fountain clocks that have been established since the 1960's. In an optical clock or Cesium-based fountain clock the transition frequency between two electronic states in an atom is used as a timekeeper. Alkaline-earth atoms have received much attention for their use in optical clocks because they possess a narrow, optical transition $^1S_0 \rightarrow {}^3P_0$ [33, 32]. Also, atoms in either of the two electronic states can be made to experience identical trapping potentials by using lasers at an appropriate wavelength (the "magic wavelength"). We will review an important process that contributes to the uncertainty in optical clock measurements: it is a collision induced frequency shift observed in optical lattice clock experiments. The many-body formalism shows how the frequency shifts arise during the spectroscopic process. This formalism also offers insight as to the methods of suppressing the collision induced frequency shift. It will be demonstrated that an increase in interaction strength between the atoms results in a counterintuitive supresssion of the frequency shift.

In the final Chapter, we summarize our results and motivate extensions presented in this body of work.

Chapter 2

Background and Concepts

The goal of this chapter is to introduce the physical principles that lay the conceptual groundwork for the remaining chapters. We begin by introducing the basic physics of light/atom interactions which provides the fundamental basis of how optical lattices work. We describe the theory of a single particle under the influence of a periodic potential followed by a discussion of interactions using basic scattering theory. This is motivated by the need to generalize to a many-body picture where we discuss the simplest of a variety of many-body quantum models, the Bose-Hubbard model.

2.1 Optical lattice in 1D

In crystals, electrons feel a periodic potential formed by arrays of ion cores. In atomic physics, a 1D periodic potential is formed from two interfering counter-propagating laser beams forming a standing wave of light. 2D and 3D optical lattices typically require two and three pairs of lasers, respectively. Optical lattices provide a crystal-like structure without defects. The freedom to change the laser configuration can lead to more complicated periodic structures than a simple cubic lattice or lead to structures that do not have simple discrete translational symmetry.

Consider a picture of an atom that consists of one electron and a nucleus. The Hamiltonian can be reformulated into two independent systems: one involving the center-of-mass motion and the other involving the relative motion. Neglecting the center-of-mass motion of the system, the Hamiltonian in the relative coordinates is

$$H = \frac{\vec{\mathbf{p}}^2}{2m} + U(\vec{\mathbf{r}}), \tag{2.1}$$

where m is the reduced mass and $U(\vec{\mathbf{r}})$ is the Coulomb potential. The minimal coupling Hamiltonian describes the behavior of an electron in the presence of a radiation field,

$$H = \frac{(\vec{\mathbf{p}} + e\vec{\mathbf{A}}(\vec{\mathbf{r}}, t))^2}{2m} + U(\vec{\mathbf{r}}), \tag{2.2}$$

where $\vec{\mathbf{A}}$ is the vector potential. The wavelength associated with optical fields is $\sim 10^{-6}$ m, whereas the size of the atom ($a_0 \sim 10^{-10}$ m) is typically four orders of magnitude smaller. Therefore, we can make the approximation that the vector potential is constant over typical atomic distances. This is known as the dipole approximation. Here, we can also neglect the $|\vec{\mathbf{A}}|^2$ term if we assume the radiation field is weak. Now by performing a substitution to the wave function, $\psi(\vec{r}, t) \rightarrow e^{-ie\vec{A}(t)\cdot\vec{r}/\hbar}\psi(\vec{r}, t)$, the resulting Hamiltonian is

$$H = \frac{\mathbf{p^2}}{2m} + U(\vec{\mathbf{r}}) + e\vec{\mathbf{E}} \cdot \vec{\mathbf{r}}, \tag{2.3}$$

where $\vec{\mathbf{E}} = -\dot{\vec{\mathbf{A}}}$. Therefore, the approximate interaction of the atom with the radiation field is given by a dipole interaction. Physically, the atom in the presence of an electric field acquires a dipole moment $\vec{\mathbf{d}} = -e\vec{\mathbf{r}}$. The interplay between the neutral atom and the optical lattice is then described by the interaction between the induced dipole and the electric field,

$$H_{\text{int}} = -\vec{\mathbf{d}} \cdot \vec{\mathbf{E}}. \tag{2.4}$$

The Hamiltonian of a two-level atom interacting with this field is

$$H = \frac{\hbar\omega_a}{2}\sigma_z + H_{\text{int}}, \tag{2.5}$$

where σ_z is the z component Pauli matrix and is defined by its action on the two levels $\sigma_z|e\rangle = |e\rangle$ and $\sigma_z|g\rangle = -|g\rangle$. ω_a is the angular frequency of the transition between the two atomic levels. The dipole operator couples the state $|g\rangle$ to the other state $|e\rangle$; however, the diagonal matrix elements of the dipole operator are zero since the atomic states are parity eigenstates. Assume an electric field of the form, $\vec{\mathbf{E}} = E_0 \cos(\omega t + \phi)\hat{\epsilon}$. For the following discussion, we assume the phase is $\phi = 0$. The Rabi frequency is defined by $\Omega = E_0\langle\vec{\mathbf{d}} \cdot \hat{\epsilon}\rangle/\hbar$, which can be a complex number due to E_0 or

the polarization vector. Again for simplicity, we assume Ω is real in the following discussion. The atom/light interaction part of the Hamiltonian is

$$H_{\text{int}} = -\frac{\hbar\Omega}{2}\sigma_x(e^{i\omega_c t} + e^{-i\omega_c t}). \tag{2.6}$$

In order to get rid of the explicit time dependence, one transforms the Hamiltonian by rotating into a new frame at an angular frequency of the laser field. Afterwards, the atom/light interaction contains terms with rapidly oscillating $\sim e^{\pm i(\omega+\omega_a)t}$ and slowly oscillating $e^{\pm i\delta t}$ parts. Assuming $\delta \ll \omega_a$, the rotating wave approximation consists of neglecting the rapidly oscillating terms. The final form $\tilde{H}$ is then obtained,

$$\tilde{H} = -\frac{\hbar\delta}{2}\sigma_z - \frac{\hbar\Omega}{2}\sigma_x, \tag{2.7}$$

where the detuning is $\delta = \omega - \omega_a$. In the case of a detuning $|\delta| \gg |\Omega|$, atomic transitions are suppressed. We can use second order perturbation to calculate the energy shift due to the dipole interaction,

$$E^{(2)}_{g,e} \sim \pm\frac{\hbar|\Omega|^2}{4\delta}. \tag{2.8}$$

The second order energy shift is called the AC Stark shift and the above expression represents the potential the neutral atom sees in the presence of an oscillating field. If we extend the above analysis to a spatially dependent electric field and still assume the dipole approximation is valid locally, the Rabi frequency obtains a spatial dependence. The Rabi frequency then is $\Omega(x) = \langle\vec{\mathbf{d}}\cdot\vec{\epsilon}\rangle u(x)/\hbar$, where $u(x)$ is the mode function of the electric field that satisfies the Helmholtz equation. As an example, consider two linearly polarized laser beams counter-propagating in the x-direction, $\vec{\mathbf{E}}_\pm = E_0\cos(kx \pm \omega t)\hat{\mathbf{z}}$. The total electric field is $\vec{\mathbf{E}} = \vec{\mathbf{E}}_+ + \vec{\mathbf{E}}_-$ and $u(x) = \cos(kx)$. The sign of the detuning, "blue" refering to the condition $\delta > 0$ and "red" when $\delta < 0$, affects whether the atom experiences a minimum potential at the light's lowest intensity or experiences a minimum potential at the highest intensity of the field. The force acting on the atom is proportional to the ratio of the intensity of the electromagnetic field and the detuning. The detuning can be adjusted for a fixed laser intensity in order to tune the depth of the lattice potential. However, one must be careful of the dissipative processes that occur in a real system. The excited state can decay due

to relaxation processes such as scattering or a finite radiative lifetime of the excited state. The decay from the excited state can be treated phenomelogically by introducing an imaginary term, $E_e \to E_e - i\Gamma_e/2$, to the energy shift in Eq. (2.8),

$$E_{g,e}^{(2)} \sim \pm\frac{\hbar\Omega^2}{4(\delta - i\Gamma_e/2)} = \pm\frac{\hbar\Omega^2}{4(\delta^2 + \Gamma_e^2/4)}(\delta + i\Gamma_e/2), \tag{2.9}$$

which introduces a real part in the energy shift that acts as an effective potential and an imaginary part that represents the finite lifetime of the excited state. From the imaginary term in Eq. (2.9), the rate of these dissipative processes ($\sim 1/\delta^2$) are reduced by large detunings.

After having described the atom/light interaction and the periodic potential provided by the optical lattice, we move on to describe the band theory that arises from the discrete translational symmetry of these systems. It will be shown that for sufficiently large lattice depths, a tight-binding model can be derived which is described by nearest neighbor atom tunneling.

2.2 Band Theory

Since the optical lattice is a periodic potential, we review the general theory of a single particle in the presence of a periodic potential. A thorough analysis can be found in references [34, 35]. The time-independent Schrödinger equation is,

$$\frac{-\hbar^2}{2m}\frac{\partial^2\psi(x)}{\partial x^2} + U(x)\psi(x) = E\psi(x) \tag{2.10}$$

where the potential possesses the discrete translational symmetry $U(x) = U(x + a)$ and a is the lattice spacing. If we consider the lattice potential to be $U(x) = U_0\cos^2(2\pi x/a)$ as formed from the lattice in the previous section, an exact analytic solution is provided in the form of Mathieu functions [36]. However, the Schrödinger equation with a general potential does not always easily admit an exact solution. A more general approach, amenable to straightforward approximations, is required to understand the band structure of more complicated periodic potentials. To simplify calculations, we assume periodic boundary conditions $\psi(x + L) = \psi(x)$. The wave function can

then be written in terms of a plane wave expansion of the form,

$$\psi(x) = \frac{1}{L}\sum_q a_q e^{iqx}, \tag{2.11}$$

where $q = 2\pi m/L$ and m an integer. Since the potential $U(x) = U(x+a)$ has periodicity of a lattice site, it can also be decomposed into a Fourier sum of plane waves $U(x) = \sum_K U_K e^{iKx}$ where K is a reciprocal lattice vector. Plugging these expressions back into Eq. (2.10) yields,

$$(\frac{\hbar^2 q^2}{2m} - E)a_q + \sum_K U_K a_{q-K} = 0. \tag{2.12}$$

For a given wave vector q, this equation provides a Hamiltonian that is an $M \times M$ matrix where M is the number of reciprocal lattice vectors and the n eigenvalues are the energy bands $E_{n,q}$. Given a wavevector q, we can re-express it as $q = k - K$ where k lies in the first Brillouin zone. The matrix equation becomes

$$(\frac{\hbar^2 (k-K)^2}{2m} - E)a_{k-K} + \sum_{K'} U_{K'-K} a_{k-K'} = 0. \tag{2.13}$$

Written in this form, it is apparent that the Bloch particle couples only to certain Fourier components of the lattice potential. Therefore, the eigenfunctions must have the form,

$$\psi(x) = \frac{1}{L}\sum_K a_{k-K} e^{i(k-K)x}. \tag{2.14}$$

where k lies within the first Brillouin zone. This is a restatement of Bloch's Theorem which states that given a potential with translational symmetry described above, the eigenfunctions have the form of a plane wave expansion

$$\psi_{nk}(x) = u_{nk}(x) e^{ikx}, \tag{2.15}$$

where the function $u_{nk}(x)$ shares the same periodicity as the potential. The band index n denotes the family of solutions that exists for each wave vector k. Furthermore, one denotes the quantity $\hbar k$ as the crystal momentum and it is not to be confused with the actual momentum of the particle, since $\psi_{nk}(x)$ is not an eigenstate of the momentum operator. We can apply perturbation theory for a weak potential U. However, non-degenerate perturbation theory breaks down at the zone

boundaries due to the near degeneracy of the energy levels for states $|k\rangle$ and $|k+K\rangle$. Writing $|\psi\rangle = A|k\rangle + B|k+K\rangle$, degenerate perturbation theory shows that a gap opens up with magnitude,

$$E_{gap} = 2\sqrt{\frac{(E_k^0 - E_{k+K}^0)^2}{4} + |U_K|^2}. \tag{2.16}$$

The energy gap plays a very important role in the dynamics of a particle on the lattice. For instance, the location of the Fermi energy and in a gapped system can determine whether a system of non-interacting fermions behaves as a metal or a band insulator. Furthermore, the accuracy of the single-band tight-binding model (which will be described in the next section) requires a sizable energy gap. Before introducing the tight-binding method, we work through an illustration of the use of Eq. (2.13) in obtaining the energy bands. Consider a lattice potential $V(x) = V_0\cos(kx) = V_0/2(e^{-ikx} + e^{ikx})$ where $k = 2\pi/a$ and N sites. Due to the periodicity of the lattice, the reciprocal lattice vector is $K = nk$, where n is an integer. Setting $\pi/a \equiv 1$, Eq. (2.13) for a given $k = (\pi/a)(2\ell - N)/N$ (where ℓ is an integer) within the first Brillouin zone looks like

$$((k-2n)^2)a_{k-n} - V_0/2(a_{k-(n+1)} + a_{k-(n-1)}) = Ea_{k-n}.$$

The above equation is an eigenvalue problem for a system of equations, $\mathbf{H_k a_k} = E_k\mathbf{a_k}$ for each k. The column vector $\mathbf{a_k}$ is an $M \times 1$ column vector, H_k is a tridiagonal $M \times M$ matrix, and M is the number of reciprocal lattice vectors. We plot E_k versus k for the first three bands in Fig. 2.2. A deeper lattice creates a larger energy gap at the edges consistent with the results from degenerate perturbation theory. Correspondingly, the zero quasi-momentum Bloch wavefunction in the lowest band exhibits localization at the lattice sites for a deep lattice.

2.3 Tight-Binding Hamiltonian

For a deep lattice the particle is localized at the lattice site indicated by the localization of the Bloch wavefunction (see Fig. 2.2). It is natural then to recast the Hamiltonian in terms of a set of localized wavefunctions. If an energy gap exists, we can expand the wave function in terms of orthogonal wave functions called Wannier orbitals which are nearly localized on a lattice site and

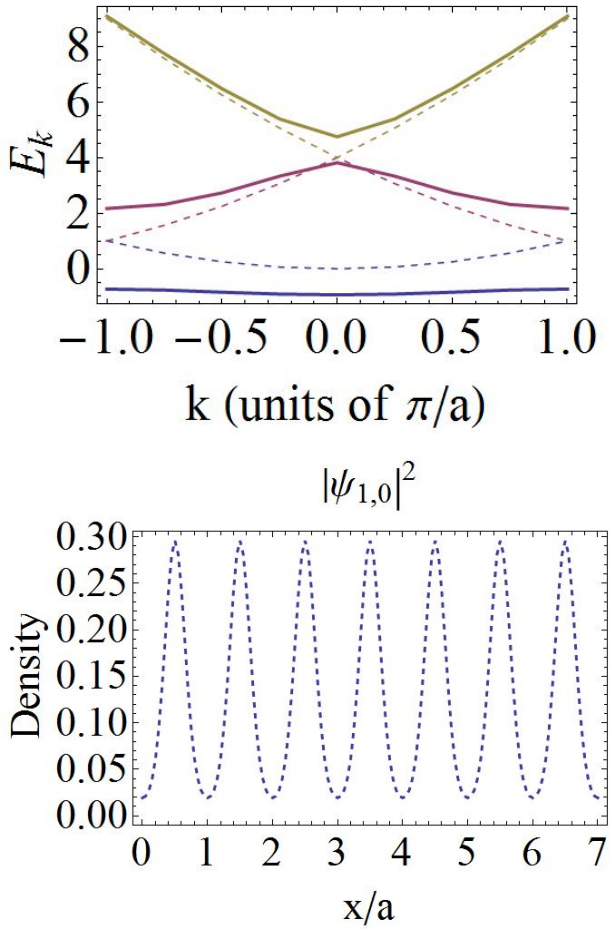

Figure 2.1: Band Structure of a periodic lattice of the form $V(x) = V_0 \cos(kx)$ which is shown on the top figure. The dispersion curve is plotted for $V_0 = 0$ (dashed) and for a deeper lattice $V_0 = 3E_R$ (solid). On the bottom, the corresponding zero quasi-momentum Bloch function is shown. As the lattice depth increases, the Bloch function becomes more localized on each site.

are given by,

$$w_n(x - x_i) = \frac{1}{\sqrt{N}} \sum_k e^{-ikx_i} \psi_{nk}(x),$$

where N is the number of sites and the sum is over the first Brillouin zone. We note that there is an arbitrary phase factor $e^{i\phi_{nk}}$ that is not unique to each Bloch wavefunction $\psi_{nk}(x)$ which must be accounted for when calculating optimally localized Wannier orbitals [37]. When the particle is well localized at each site, the dynamics is dominated by nearest-neighbor tunneling. Consider the Schrödinger equation of a particle in the presence of a lattice and external potential. If we assume

that the lattice is deep enough and that the external potential is too weak to induce interband transitions, we can make the approximation that the dynamics remains only in the lowest band. Henceforth, we drop the band index. Writing the Schrödinger equation in the Wannier orbital basis leads to a tight-binding model [35, 38]. This model represents a minimalistic portrait of a particle on a lattice potential. In the Wannier basis, the Hamiltonian is,

$$H_{\text{tight}-\text{binding}} = -J \sum_{\langle i,j \rangle} |i\rangle\langle j| + \sum_i |i\rangle V(x_i)\langle i|, \tag{2.17}$$

where

$$\begin{aligned} J &= -\int dx\ w(x-x_i)\left(\frac{-\hbar^2}{2m}\frac{d^2x}{dx^2} + U_{\text{lat}}\right)w(x-x_{i\pm1}), \\ V(x_i) &= \int dx\ w(x-x_i)V(x)w(x-x_i). \end{aligned} \tag{2.18}$$

As an example, assume a lattice spacing $a = 1$ with no external potential presnt. The tight-binding Hamiltonian can be solved by a Fourier transformation, resulting in an energy dispersion $E_k = -2J\cos k$. This energy dispersion approximates the first band shown in Fig. (2.2). In Chapter 3, we will encounter the tight-binding model of a particle in a lattice in the presence of an external linear potential. This model captures the dynamics of Bloch oscillations mentioned in Chapter 1.

We can gain insight as to how the tunneling strength depends on the lattice depth by performing the so-called harmonic approximation. For ultracold atoms in deep optical lattices, each site can be approximated by a harmonic oscillator potential, i.e., $V_0 \sin^2(kx) \approx V_0 k^2 x^2$. In this approximation, the Wannier orbitals are then harmonic oscillator eigenstates. If we consider the atoms to reside in the lowest vibrational state, the Wannier orbitals take the form of a Gaussian wave function. In this case, the tunneling strength can be calculated [6],

$$J \sim \left(\frac{V_0}{E_r}\right)^{3/4} E_r e^{-2\sqrt{V_0/Er}}. \tag{2.19}$$

Because the Gaussian wave function neglects the oscillations that exist in the actual Wannier wavefunctions, the tunneling amplitude is typically underestimated in this approximation. Though we have restricted our discussion to dynamics in a single-band, it is also important to mention that tight-binding models can be generalized to include interband dynamics.

After having described the single particle physics in a periodic potential, we now introduce interactions. At the many-body level, low energy s-wave collisions are the first approximation to atom-atom interactions. This approximation is adopted by the Bose-Hubbard Hamiltonian which will be discussed after we review the basic scattering theory which derives the form of the interaction.

2.4 Atom Interactions and the S-Wave Scattering Length

In this section, we review the treatment of interparticle interactions in a two-body scattering problem [39, 40, 41]. We closely follow the treatment found in Sakurai [39]. In this picture, it is first natural to consider a single particle in the presence of a scattering potential $U(\vec{r})$. Typically below microkelvin temperatures, the de Broglie wavelength of the atoms are long compared to the range of the scattering potential. In this case, the short range details of the potential are less important and one can then make the approximation that the potential is featureless and spherically symmetric. Furthermore, in this temperature regime, the atoms cannot overcome the centrifugal barrier of the effective potential in the radial Schrödinger equation and so interactions are then typically dominated by collisions in the lowest angular momentum (s-wave for bosons). After having formulated the relevant conditions in this scattering problem, we consider the asymptotic behavior of the wavefunction. Far beyond the extent of the scattering potential, the wavefunction is a sum of an incident plane wave and outgoing spherical wave,

$$\psi \sim e^{ikz} + \frac{f(\theta)}{r} e^{ikr}. \tag{2.20}$$

The quantity $f(\theta)$ is called the scattering amplitude and depends only on the angle θ between $\vec{r}$ and z. In the scattering problem, one tries to find an expression for the scattering amplitude. Consider the general Schrödinger equation,

$$(H_0 + U)|\psi\rangle = E|\psi\rangle \tag{2.21}$$

In the absence of the scattering potential, let $H_0|\vec{\mathbf{k}}\rangle = E|\vec{\mathbf{k}}\rangle$, where $E = \hbar^2 k^2/2m$. By this choice of E, we consider the condition of elastic scattering where the energy does not change. The general

solution of the wavefunction is given by the Lippman-Schwinger equation,

$$|\psi\rangle = \frac{1}{E - H_0 + i\epsilon} U|\psi\rangle + |\mathbf{k}\rangle. \tag{2.22}$$

The real space representation of the wavefunction is given by,

$$\psi(\vec{\mathbf{x}}) = \langle \vec{\mathbf{x}}|\vec{\mathbf{k}}\rangle - \frac{m}{2\pi\hbar^2} \int d^3\vec{\mathbf{y}} \frac{e^{ik|\vec{\mathbf{x}}-\vec{\mathbf{y}}|}}{|\vec{\mathbf{x}}-\vec{\mathbf{y}}|} U(\vec{\mathbf{y}})\psi(\vec{\mathbf{y}}). \tag{2.23}$$

If we consider the asymptotic behavior of the wavefunction at distances far away from the extent of the potential, the expression breaks up into a sum of an incoming plane and an outgoing spherical wave. By adopting the first order Born approximation where the scattered wavefunction in the integral is replaced by the incoming plane wave, we can find the expression for the scattering amplitude,

$$f(\theta) = -\frac{m}{k\sin(\theta/2)\hbar^2} \int_0^\infty dr\ rU(r)\sin(2kr\sin(\theta/2)). \tag{2.24}$$

The Born approximation says that the incoming particle should not be very different from the total wavefunction. This happens to be the case for low energy scattering only if the potential of the scatterer is too shallow to confine a particle within the range of the potential. Furthermore, considering low energy scattering $k \to 0$, the amplitude becomes,

$$f(\theta) = -\frac{2m}{\hbar^2} \int_0^\infty U(r)r^2 dr. \tag{2.25}$$

We return to the radial equation of the Schrödinger equation. In the limit of zero energy ($k \to 0$), at distances beyond the effect of the potential of the scatterer, and at an angular momentum $\ell = 0$, the wavefunction $\psi(r) = u(r)/r$ satisfies,

$$\frac{d^2}{dr^2}u(r) = 0 \quad \to \quad \psi(r) \sim 1 - a_s/r. \tag{2.26}$$

The quantity a_s is called the s-wave scattering length and represents a natural low energy scattering parameter. If we look at Eq. (2.25), we can relate the scattering length to the interaction by,

$$a_s = \frac{2m}{4\pi\hbar^2} U_0, \tag{2.27}$$

where U_0 is the zero momentum component of the three dimensional Fourier transform. We note that the mass m actually refers to the relative mass of the two-body scattering problem. In the case that the two masses are the same, the mass m used in the above discussion is replaced with the effective mass $m/2$. In coordinate space, the effective interaction now looks like an effective contact potential,

$$U(r-r') = \frac{4\pi\hbar^2}{m} U_0 \delta(r-r'). \tag{2.28}$$

This form of the interaction represents an approximation adopted in literature to represent the interaction between atoms. Generalizing beyond the first Born approximation, the effective interaction can be related to higher Born approximations. Furthermore, the scattering length of atoms can be controlled with external magnetic fields, in effect changing the interaction strength and even the sign [40]. We are now ready to review the many-body physics after having just discussed the rudiments of incorporating two-body interactions.

2.5 Many-Body Physics and the Bose-Hubbard Model

In many-body quantum mechanics, it is natural to use the second quantization formalism which is an efficient way of dealing with complicated many-body wavefunctions. In this formalism, one introduces the bosonic field operator $\hat{\psi}^\dagger(x)$ ($\hat{\psi}(x)$) which act on a state in the Hilbert space to create (annihilate) a particle at position x and satisfies the following commutation relations,

$$\begin{aligned} [\hat{\psi}(x), \hat{\psi}^\dagger(x')] &= \delta(x-x'), \\ [\hat{\psi}(x), \hat{\psi}(x')] &= 0, \\ [\hat{\psi}^\dagger(x), \hat{\psi}^\dagger(x')] &= 0. \end{aligned} \tag{2.29}$$

The many-body Hamiltonian operator of interacting bosons on a lattice plus external potential is written in the grand canonical ensemble as,

$$\hat{H} = \int d^3x \hat{\psi}^\dagger(x)(\frac{\hat{p}^2}{2m} + V_{\text{lat}}(x) + V_{\text{ext}}(x) - \mu)\hat{\psi}(x) + \frac{1}{2}\int\int d^3x d^3x' \hat{\psi}^\dagger(x)\hat{\psi}^\dagger(x')U(x,x')\hat{\psi}(x')\hat{\psi}(x), \tag{2.30}$$

where $V_{\text{lat}}(x)$ is the lattice potential, $V_{\text{ext}}(x)$ is an arbitrary external potential, $U(x, x')$ is a two-body potential created by interparticle interactions, and μ is a chemical potential which fixes the particle number. As an example, the external potential can be a harmonic trap or a linear potential (see Chapter 3). The interaction potential $U(x, x')$ is assumed to have the same form as the contact potential in Eq. (2.28). In addition, the field operators can be expanded in any orthonormal set of single-particle wave functions. From the discussion in Section 2.3, it is natural to expand the field operators in terms of Wannier orbitals because the system is on a lattice. If we assume the chemical potential is too weak to induce population of higher bands, we can then expand the field operator in terms of the first band Wannier orbitals,

$$\hat{\psi}(x) = \sum_i \hat{a}_i w_0(x - x_i). \tag{2.31}$$

The operator $\hat{a}_i$ annihilates a particle in the localized Wannier orbital centered on site i. From the closure property of the Wannier orbitals, $\sum_i w_0(x - x_i)w_0(x' - x_i) = \delta(x - x')$, the new operators satisfy the commutation relations,

$$\begin{aligned} [\hat{a}_i, \hat{a}_j^\dagger] &= \delta_{ij} \\ [\hat{a}_i, \hat{a}_j] &= 0, \\ [\hat{a}_i^\dagger, \hat{a}_j^\dagger] &= 0, \end{aligned} \tag{2.32}$$

and $\hat{n}_i = \hat{a}_i^\dagger \hat{a}_i$ is the number operator.

The field operator expansion can be substituted into Eq. (2.30), and if we consider only nearest neighbor tunneling, the result is known as the Bose-Hubbard Hamiltonian,

$$H = -J \sum_{\langle i,j \rangle} (\hat{a}_i^\dagger \hat{a}_j + \text{h.c.}) + \frac{U}{2} \sum_i \hat{n}_i(\hat{n}_i - 1) + \sum_i (V(i) - \mu)\hat{n}_i. \tag{2.33}$$

The first term describes tunneling of particles to nearest neighboring sites. The second term describes interparticle interactions which exist when at least two particles are on the same site. The tunneling strength J is an overlap integral similar to Eq. (2.18), and the interaction energy U is given by the overlap intergral,

$$U = \frac{4\pi a_s \hbar^2}{m} \int d^3x |w(x)|^4, \tag{2.34}$$

where from the harmonic approximation, it has the form

$$U \sim \left(\frac{U_0}{E_r}\right)^{3/4} k a_s E_r. \tag{2.35}$$

The Bose-Hubbard model (BHM) was introduced to describe the onset of superfluidity and superfluid dynamics in systems like He-4 on a substrate or Cooper pairs of electrons tunneling through Josephson arrays [5, 42]. It was later shown that it could describe ultracold bosonic atoms on an optical lattice [6]. The advantage of ultracold atoms is that the ratio of the tunneling strength to the interaction energy can be directly controlled by the intensity of the laser of the optical lattice. We now review the properties of the BHM, which has been thoroughly discussed in Ref. [5] and Ref. [42]. The BHM captures the competition between two competing energy scales: the kinetic energy and the interaction energy of the system. The kinetic energy term is minimized by a delocalized wavefunction. On the other hand, the interaction term serves to localize the particles. In experiments with ultracold atoms, an external harmonic potential is present. However, the properties conveyed in the translationally invariant system are not entirely conceptually different than when the external potential is present. Therefore, we will neglect the harmonic confinement in the following discussion. We consider two limits to this model: one where there are no interactions ($U/J = 0$) and the other when tunneling is frozen ($J/U = 0$). By adiabatically changing the parameters from $J/U = 0$ to a sufficiently large J/U, we would expect the ground state to change from a spatially localized state to a delocalized state. This is the description of the Mott insulator to a superfluid zero-temperature quantum phase transition. Let us proceed first by describing the ground state of the system at both extremes.

When $U/J = 0$, the Hamiltonian is diagonalized in momentum space by the typical Fourier transformation,

$$\hat{a}_j = \frac{1}{\sqrt{N}} \sum_k \hat{a}_k e^{ikj}, \tag{2.36}$$

where $\hat{a}_k$ satisfies the same bosonic commutation relations as $\hat{a}_j$. The Hamiltonian written in terms of the new operators is

$$H = \sum_k E_k^{(0)} \hat{n}_k \tag{2.37}$$

where the energy dispersion $E_k^{(0)} = -2J\cos(k)$. The excitation energy is gapless. The eigenstates are product states in the k basis and are given by,

$$|\phi_{\vec{k}}\rangle = \prod_i \frac{(\hat{a}_{k_i}^\dagger)^{n_{k_i}}}{\sqrt{n_{k_i}!}}|0\rangle \tag{2.38}$$

where the ith component of $\vec{k}$ labels the state of the ith particle. In the ground state, all particles occupy the quasi-momentum $k = 0$ state. This corresponds to a macroscopic occupation over a single particle wave function and the $k = 0$ wave function is equally spread out over the entire lattice, as can be seen in Eq. (2.36). The particles are therefore delocalized and also share a well-defined phase. In experiment, phase coherence in a superfluid is detected by releasing the system from the lattice and letting it expand. After expansion, phase coherence produces an interference pattern [7]. Another property of the superfluid is that the local number fluctuations have a Poissonian distribution. This feature has also been used to probe to the superfluid [43].

For a finite, but small U, the zero quasi-momentum state is still macroscopically occupied. However, the presence of the interaction energy induces fluctuations about this state. The Hamiltonian in momentum space is,

$$H = \sum_k (E_k^{(0)} - \mu)\hat{a}_k^\dagger \hat{a}_k + \frac{U}{2V}\sum_{k,k',q} \hat{a}_{k+q}^\dagger \hat{a}_{k'-q}^\dagger \hat{a}_{k'}\hat{a}_k \tag{2.39}$$

In the Bogoliubov method, the operator $\hat{a}_0^\dagger$ is replaced by $N_0 + \hat{a}_0^\dagger$, a c-number plus a fluctuation term. The c-number N_0 is the macroscopic occupation of the condensed state. Retaining terms to zeroth and second order in the fluctuations, the Hamiltonian is diagonalized by a Bogoliubov transformation [44],

$$\hat{a}_{\pm k} = u_k \hat{\alpha}_{\pm k} - v_k \hat{\alpha}_{\mp k}^\dagger, \tag{2.40}$$

where u_k and v_k are real coefficients and $\hat{\alpha}_p$ is a bosonic operator which annihilates a quasi-particle of momentum p. Due to the commutation relation of the original bosonic operators, the coefficients satisfy the condition $u_k^2 - v_k^2 = 1$. These new quasiparticle states are excitations of momentum k above the ground state. The excitation energy above the ground state is again gapless and is given

by,

$$E_k = \sqrt{(E_k^{(0)})^2 + 2U(N_0/L)E_k^{(0)}}. \tag{2.41}$$

As the interaction energy is increased, a macroscopic occupation of the zero quasi-momentum ground state should cease to exist and an energy gap should open. However, the Bogoliubov method does not predict this phenomenon. We must approach the transition from the opposite direction [44].

Consider the case when the tunneling strength J is zero. In this case, the particles are localized and the ground state minimizes the local interaction term in the Hamiltonian. For a commensurate filling of n particles per site, the ground state is a direct product of local Fock states,

$$|\phi_{\rm n}\rangle = \prod_{i=1}^{L} \frac{1}{\sqrt{n!}} (\hat{a}_i^\dagger)^n |0\rangle. \tag{2.42}$$

All available quasimomentum states are equally populated and because this many-body state is not a macroscopic occupation of a single particle wave function, phase coherence is lost. In experiment, no interference effects can be seen when the atoms in the Mott state are released from the trap [7]. In addition, local number fluctuations are greatly suppressed. The energy per site is given by $E_{\rm site} = Un(n-1)/2$ and the addition of a particle raises the energy per site by nU. One particle-hole excitations which describe the addition of a particle at a site and the removal of a particle at another site are the lowest lying excited states with energy U higher than the ground state. This energy gap and a quantized density are features of the Mott insulator phase. For small, but finite J the lowest lying excited states are single particle-hole excitations where the particle and the hole occupy adjacent sites. As J/U increases, we expect to observe a transition into a superfluid state. We review below the mean-field treatment of this phase transition.

2.5.1 Phase Transition

The phase diagram is illustrated in Fig. 2.5.1 which delineates the parameter regime when either the Mott insulator or the superfluid is the ground state of the BHM. There are two types

of transitions: one which is accompanied by a change in density and the other occuring at fixed density. First consider going upward on the phase diagram by increasing the chemical potential with J fixed. Suppose we start in one of the lobes of the Mott insulator phase. As the chemical potential μ increases (decreases), the energy cost of adding a particle (hole) is overcome by the kinetic energy of this additional particle. When this happens, the state returns to the superfluid phase. The other transition occurs at fixed integer density. By increasing J/U, the interaction energy is overcome by the kinetic energy of the particle-hole excitations. This again will bring the system back to a superfluid state.

The phase diagram in Fig. 2.5.1 is derived from a mean field theory. In this mean field theory, the interactions are treated exactly. Recall that when hopping is absent, the ground state is determined by minimizing the on-site energy,

$$E(n+1) - E(n) > 0 \text{ and } E(n-1) - E(n) > 0$$

where $E(n) = \frac{U}{2}n(n-1) - \mu n$. This implies that there are n_0 particles on each site where n_0 satisfies $n_0 - 1 \leq \mu/U \leq n_0$.

One investigates the quantum phase transition by adding a mean field term to the on-site interaction term of the orginial Hamiltonian that breaks the $U(1)$ symmetry of the original Hamiltonian,

$$H_{MF} = \sum_i -(\hat{a}_i^\dagger \psi^* + \hat{a}_i \psi) + \frac{U}{2}\hat{n}_i(\hat{n}_i - 1) - \mu \hat{n}_i. \tag{2.43}$$

The mean field value of the ground state energy is calculated by taking the expectation value of the original Hamiltonian with the ground state of H_{MF} which is a product of single-site wavefunctions,

$$E_0 = \langle H_{MF} + (H - H_{MF}) \rangle = E_{MF} + N(-zJ\langle \hat{a}^\dagger \rangle \langle \hat{a} \rangle + \langle \hat{a} \rangle \psi^* + \langle \hat{a}^\dagger \rangle \psi), \tag{2.44}$$

where the coordination number z is the number of nearest-neighbors connected to an arbitrary site i. For example, $z = 2$ in 1D. The phase boundary is numerically calculated by minimizing the above equation with respect to the order parameter ψ. However, the phase boundary can be determined analytically using the Landau argument for continuous phase transitions. In the Landau theory,

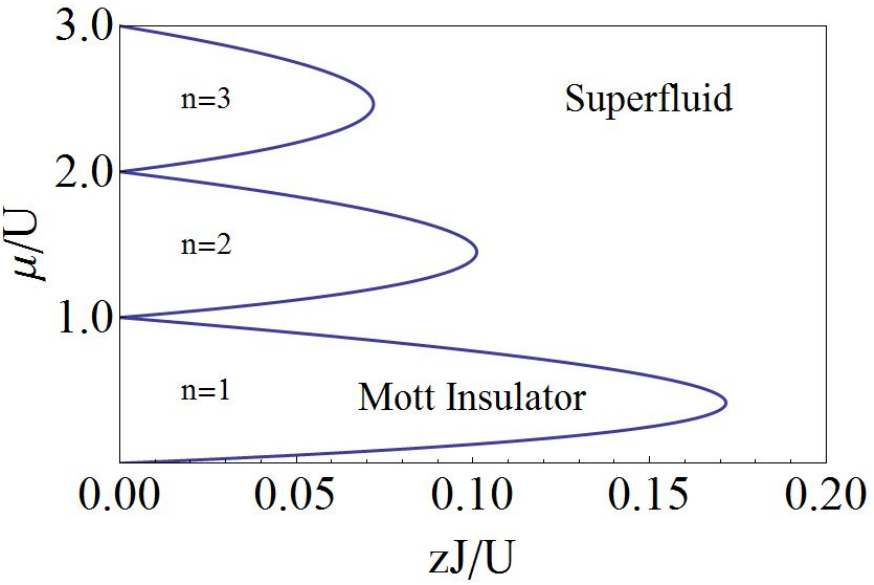

Figure 2.2: Zero Temperature phase diagram of the Bose-Hubbard Model derived from mean field theory.

the energy can be expanded as $E_0 = E(n_0, U, \mu) + \alpha|\psi|^2 + \mathrm{O}(|\psi|^4)$, where α changes sign across a phase boundary. When $\alpha > 0$ the minimum of E_0 is obtained when the order parameter $\psi = 0$ and when $\alpha < 0$, $\psi \neq 0$. The coefficient α is calculated from second order perturbation theory, $E^{(2)}_{MF} = |\psi|^2 \sum_{m \neq n_0} \frac{|\langle \phi_m | (\hat{a}^\dagger + \hat{a}) | \phi_{n_0} \rangle|^2}{E(n_0) - E(m)}$ and therefore,

$$\frac{E_0}{N} = \frac{U}{2} n_0(n_0 - 1) - \mu n_0 - \chi(1 - zJ\chi)|\psi|^2, \tag{2.45}$$

where $\chi = \frac{n_0+1}{Un_0 - \mu} + \frac{n_0}{\mu - U(n_0 - 1)}$. From setting $\alpha = 0$, the phase boundary is given by,

$$zJ = \frac{(n_0 - \frac{\mu}{U})(\frac{\mu}{U} - n_0 + 1)}{n_0(n_0 - \frac{\mu}{U}) + (n_0 + 1)(\frac{\mu}{U} - n_0 + 1)}. \tag{2.46}$$

In the following section, we review another strongly correlated system that is described by the BHM and which has also been observed in experiment [45]. In the Tonks-Girardeau (TG) regime [46], the on-site interaction $U \to \infty$ and prevents the occupation of more than one boson per site. In effect, the particles are said to fermionize because the forbidden double occupancy acts

like the Pauli exclusion principle. We motivate the discussion now because in Ch. 4 and Ch. 5, we will come across the dynamics of this system.

2.5.2 Hard core Limit

In the regime where the on-site interaction parameter $U \to \infty$, double occupancy of a site is energetically forbidden. This parameter regime is described as the hard core boson (HCB) limit and in some sense the particles have fermionized. The Hamiltonian for the system is

$$H = -J \sum_{\langle i,j \rangle} (\hat{a}_i^\dagger \hat{a}_j + h.c.) + \sum_i V_i \hat{n}_i, \tag{2.47}$$

where the bosonic creation ($\hat{a}_i^\dagger$) and annihilation ($\hat{a}_i$) operators satisfy the same commutation relations as before, but the forbidden double occupancy is enforced by imposing the additional constraint $(\hat{a}_i^\dagger)^2 = (\hat{a}_i)^2 = 0$. Due to the hard-core constraint, the local Hilbert space is reduced to two states: an occupied site $|1\rangle$ and an empty site $|0\rangle$. The available states in the local Hilbert space allow the system of bosons to map to a spin-1/2 system. The mapping convention is

$$\begin{aligned} |1\rangle &\to |\uparrow\rangle, \\ |0\rangle &\to |\downarrow\rangle, \\ \hat{a}_i^\dagger &\to \sigma_i^+, \\ \hat{a}_i &\to \sigma_i^-. \end{aligned} \tag{2.48}$$

The Hamilontian in the spin-1/2 representation then is

$$H = -2J \sum_i (\sigma_i^x \sigma_j^x + \sigma_i^y \sigma_j^y) + \sum_i V_i (\sigma_i^z + 1)/2. \tag{2.49}$$

Although the new representation is sufficient for calculating local observables like the density in the dynamics of HCBs (which will be demonstrated in the later chapters), the mapping is nevertheless incomplete. The on-site commutation relations of the Pauli matrices are in fact different from the bosonic commutation relations leading to a discrepancy in the calculation of various correlations [47]. In order to solve the Hamiltonian in 1D, HCBs are mapped to spinless fermions through the

Jordan-Wigner transoformation [48],

$$\begin{aligned} \hat{a}_i^\dagger &= \hat{c}_i^\dagger \prod_{j=1}^{i-1} e^{-i\pi \hat{c}_j^\dagger \hat{c}_j}, \\ \hat{a}_i &= \prod_{j=1}^{i-1} e^{i\pi \hat{c}_j^\dagger \hat{c}_j} \hat{c}_i, \end{aligned} \tag{2.50}$$

where $\hat{c}_i^\dagger$ ($\hat{c}_i$) is the creation (annihilation) operator for a spinless fermion on site i, and the operators satisfy the anticommutation relations. The Hamiltonian then transforms to

$$H = -J \sum_{\langle i,j \rangle} (\hat{c}_i^\dagger \hat{c}_j + h.c.) + \sum_i V_i \hat{n}_i, \tag{2.51}$$

where the number operator $\hat{n}_i = \hat{c}_i^\dagger \hat{c}_i$ is written in terms of the fermionic creation and annihilation operators. Therefore, the energy spectrum of the HCB system in 1D is identically the same as the non-interacting spinless fermions. However, the momentum distribution is different from the inspection of the off-diagonal elements of the single particle density matrix $\langle \hat{b}_i^\dagger \hat{b}_j \rangle$ [49]. The momentum distribution shows a peak population of the $k = 0$ state whereas a system of fermions do not share this property due to the Pauli exclusion principle. The population of the $k = 0$ state does not represent a true condensation since the population scales as the square root of the number of particles. We will come back to the HCB system when we study transport properties and soliton stability in strongly interacting bosonic systems in chapters 4 and 5.

Chapter 3

Time Evolution Block Decimation and Density Matrix Renormalization Group Methods

Exactly solvable quantum many-body problems are the exception rather than the rule. However, various theoretical techniques like perturbation theory, mean field approximation, and variational methods were developed to study properties of systems which could not be exactly solved. In many cases, these approximate tools are preferred over exactly solvable methods like the Bethe ansatz [50], since the results of approximate methods can offer more physical insight than the exact solution itself. Along with the inability to obtain analytical solutions for every model, exact computational methods in the form of exact diagonalization have proven difficult to implement due to the exponential growth of the Hilbert space with system size. For example, the Hilbert space dimensions of systems composed of N bosons on L sites, N spinless fermions on L sites, and an L spin-1/2 chain are $\binom{L+N-1}{N}$, $\binom{L}{N}$, and 2^L respectively. A system of 20 bosons on 20 sites has a Hilbert space dimension of approximately 70 billion. Matrix computations of this size, which require more than one hundred gigabytes of memory to store the wave function, are already too expensive with regards to memory in current classical computers. Other powerful numerical methods like quantum Monte Carlo suffer from problems which constrain them to be applied to a subset of many-body systems [51]. For instance, the quantum Monte Carlo treatment of fermionic systems is severely limited due to the notorious sign problem. It is therefore important to develop efficient algorithms which accurately simulate quantum many-body systems.

One numerical method which quickly became known as a reliable and precise tool for many-

body simulation is the density matrix renormalization group (DMRG) method. It was inspired by the real space numerical renormalization group (NRG) introduced by Wilson for the study of the Kondo problem [52]. DMRG, proposed by White in 1992 [13], was first used to accurately calculate properties (like correlation functions and the Haldane gap to near machine precision) of 1D Heisenberg models [13, 53]. These were properties that could not be accurately computed with the NRG method. The success of the DMRG algorithm is attributed to the property that the reduced density matrix eigenstates with the greatest weight provide an optimal representation of the state. We will describe the steps that comprise the method later in the chapter. Although the DMRG algorithm was initially developed to compute static properties, the algorithm was later extended to methods of time evolution [14].

One of the successful extensions of the algorithm to time evolution came from Vidal [15, 16] and is called the time-evolving block decimation algorithm (TEBD). The TEBD method is a variation of the DMRG method. Using the same truncation method of the density matrix eigenstates, the TEBD method begins with an efficient matrix product decomposition of a state which characterizes the whole system (the form of the matrix product decomposition will be explained later in the chapter). The elements in the decomposition are then dynamically updated under the premise that the entanglement of the state during the time evolution does not change drastically. Although initially constructed for 1D systems, the application of the TEBD algorithm has been extended to more complicated geometries [54] like ladder systems [55, 56] and tree networks [57].

The idea of this chapter is to review the basics of the ground state computation and the dynamics simulation in these two methods. The methods will then be applied to many-body systems presented in later chapters. This chapter consists of mainly two parts. In the first part, Section 3.2 aims to describe the steps that comprise the DMRG algorithm. The discussion is followed by a widely used extension of the DMRG algorithm to time evolution which is called the adaptive time-dependent DMRG (adpative t-DMRG). In the second part, Section 3.3 we go into more detail to describe the properties of the TEBD algorithm. Section 3.3.1 describes the matrix product representation of the quantum state used in the TEBD method. Section 3.3.2 describes how

the dynamical updating of the the matrix product representation is performed when an operator acts on the many-body state in the TEBD method. Section 3.3.3 introduces the Trotter-Suzuki time evolution of a state of the system. Before we undertake a review of the two algorithms, we begin by introducing a linear algebra result which forms the backbone of both numerical methods.

3.1 Schmidt Decomposition

The approximation scheme of a many-body state determines the efficiency of a numerical algorithm. The question one naturally asks is: how can one approximately, but accurately, represent a many-body wave function with a restricted subset of basis elements of a large Hilbert space? The answer to this question comes from the singular value decomposition (SVD) which states that an $m \times n$ matrix H can be factorized into the form,

$$\begin{aligned} H &= U\lambda V^{\dagger}, \\ H_{ij} &= \sum_{\alpha=1}^{\min(m,n)} U_{i\alpha}\lambda_{\alpha\alpha}V^{*}_{j\alpha}, \end{aligned} \tag{3.1}$$

where U is an $m \times m$ unitary matrix, V is an unitary $n \times n$, and λ is a positive diagonal $m \times n$ matrix whose diagonal elements (called singular values) are arranged in decreasing sequence, $\lambda_{\alpha\alpha} \geq \lambda_{\alpha+1\,\alpha+1}$. The columns of U are eigenstates of $HH^{\dagger}$ and the columns of V are eigenstates of $H^{\dagger}H$ which share the same eigenvalues, $\lambda^2_{\alpha\alpha}$. The SVD hints at a truncation scheme controlled by choosing the singular vectors associated with the largest singular values in the representation. This low-rank approximation of H with a rank r matrix H' is proven to minimize the Frobenius norm of their difference, a result known as the Eckart-Young Theorem [58].

Another result from linear algebra, important to our numerical methods, is derived from the SVD factorization. The Schmidt decomposition refers to a particular way that a wave function can be represented. Consider a state $|\Psi\rangle$ in a composite system $A \otimes B$,

$$|\Psi\rangle = \sum_{i,j} c_{i,j}|a^A_i\rangle|b^B_j\rangle,$$

where the set of vectors $|a^A_i\rangle$ correspond to the basis elements of system A of dimension m and $|b^B_j\rangle$ correspond to the basis elements of system B of dimension n. As an example, A and B can

correspond to the left and right block of sites which arise from a bipartition of a single 1D chain. The coefficients c_{ij} are viewed as elements of an $m \times n$ matrix and the SVD of the matrix,

$$c_{ij} = \sum_{\alpha} U_{i\alpha} \lambda_{\alpha\alpha} [V^{\dagger}]_{\alpha j}. \tag{3.2}$$

Denoting the Schmidt rank $\chi = \min(m, n)$, we can rewrite the state $|\Psi\rangle$,

$$|\Psi\rangle = \sum_{i,j} c_{i,j} |a_i^A\rangle |b_j^B\rangle = \sum_{i,j} \sum_{\alpha}^{\chi} U_{i\alpha} \lambda_{\alpha\alpha} V_{j\alpha}^* |a_i^A\rangle |b_j^B\rangle \equiv \sum_{\alpha}^{\chi} \lambda_{\alpha} |\phi_{\alpha}^A\rangle |\phi_{\alpha}^B\rangle. \tag{3.3}$$

This is called the Schmidt decomposition where λ_αs are called the Schmidt coefficients and follow the ordering $\lambda_\alpha \geq \lambda_{\alpha+1}$. The Schmidt coefficients satisfy the norm property $\sum_\alpha |\lambda_\alpha|^2 = 1$ due to the normalization of $|\Psi\rangle$. The Schmidt vectors, $|\phi_\alpha^A\rangle = \sum_i U_{i\alpha} |a_i^A\rangle$ and $|\phi_\alpha^B\rangle = \sum_j V_{j\alpha}^* |b_j^B\rangle$, are eigenvectors associated with eigenvalues λ_α^2 of the reduced density matrix $\hat{\rho}_{A(B)} = \mathrm{Tr}_{B(A)} |\Psi\rangle\langle\Psi|$. The Schmidt decomposition asserts that $|\Psi\rangle$ in a composite system $A \otimes B$ is a sum over a single index of bi-orthogonal terms where the index α spans the smallest dimensionality of the two subspaces. The approximation scheme of a state $|\Psi\rangle$ consists of keeping the first $m < \chi$ Schmidt vectors and the associated Schmidt coefficients while discarding the rest.

In quantum information theory, the Schmidt rank χ is an entanglement measure. A strongly entangled state necessarily has a large Schmidt rank while a zero-entanglement state (a product state) has $\chi = 1$. Therefore, weakly entangled states can be more accurately approximated with $m < \chi$ Schmidt vectors than a strongly entangled state. This approximation scheme, which will be implemented when we discuss DMRG and TEBD, is further motivated by two observations [16]. The first is that the Schmidt coefficients of ground states of many one-dimensional Hamiltonians (far away from any critical points) decay exponentially [59]. Secondly, the entanglement of a state does not drastically change during its time evolution [60]. The tenor is that the DMRG and TEBD algorithms are efficient for computing ground states which are weakly entangled and simulating dynamics when the state remains weakly entangled.

As an example, consider a state of three spins on a spin-1/2 chain,

$$|\Psi\rangle = \frac{|\uparrow\downarrow\uparrow\rangle - |\downarrow\uparrow\uparrow\rangle}{\sqrt{2}}.$$

Due to a bipartition at the link between the second and third site, the state $|\Psi\rangle$ can be rewritten as a product state $|\Psi\rangle = |\Sigma\rangle \otimes |\uparrow\rangle$, where $|\Sigma\rangle$ is a singlet state. The Schmidt decomposition of $|\Psi\rangle$ (or the SVD of the 4×2 matrix c) leads to the Schmidt rank $\chi = 1$. Product states which have zero entanglement always have a Schmidt rank of one and although the entire system contains a highly entangled singlet, the subsystems created from this particular bipartition are not entangled with each other. In contrast, consider a bipartition between the first and second sites. In terms of the ordered basis $\{|\uparrow\rangle, |\downarrow\rangle\}$ for the first subsystem and $\{|\uparrow\uparrow\rangle, |\uparrow\downarrow\rangle, |\downarrow\uparrow\rangle, |\downarrow\downarrow\rangle\}$ for the second subsystem, the 2×4 matrix c and its SVD are

$$c = \begin{pmatrix} 0 & 0 & 1/\sqrt{2} & 0 \\ -1/\sqrt{2} & 0 & 0 & 0 \end{pmatrix} = \begin{pmatrix} 0 & 1 \\ 1 & 0 \end{pmatrix} \begin{pmatrix} 1/\sqrt{2} & 0 & 0 & 0 \\ 0 & 1/\sqrt{2} & 0 & 0 \end{pmatrix} \begin{pmatrix} -1 & 0 & 0 & 0 \\ 0 & 0 & 0 & 1 \\ 0 & 1 & 0 & 0 \\ 0 & 0 & 1 & 0 \end{pmatrix}.$$

The Schmidt rank $\chi = 2$ is due to the fact that the biparition occurs at the link connecting the spin singlet. In this case, we have maximal entanglement which is defined when the singular values are nonzero and degenerate.

The difficulty in the aforementioned truncation stems from efficiently approximating highly entangled states. Consider the von Neumann entropy between two subystems,

$$S^{vN} = -\sum_{\alpha=1}^{\chi} \lambda_\alpha^2 \log \lambda_\alpha^2. \tag{3.4}$$

The singular values λ_α are calculated from the reduced density matrix of either of the subsystems. S^{vN} is a quantum information theory measurement of the entanglement between two subsystems and it establishes a lower bound on the number of singular values $\chi \geq e^{S^{vN}}$ required to express the state. In 1D, the von Neumann entropy of gapped systems saturates at a finite value resulting in weak entanglement [59]. However, conformal field theory arguments show that the von Neumann entropy of critical systems exhibits a logarithmic divergence with the system size [61]. We can then expect less efficiency in approximating states of critical systems using the truncation method. Furthermore, for systems at higher dimensions, S^{vN} generally scales with the boundary area of the

subsystem and is considerably larger than the logarithm scaling in 1D. This is the reason why it is so difficult to formulate an efficient approximation scheme for a many-body state of a system at higher dimensions.

3.2 Density Matrix Renormalization Group (DMRG) Method

3.2.1 Algorithm

We recapitulate the main points of the DMRG algorithm as used in calculating the zero temperature ground state of an infinite system with open boundary conditions followed by a discussion of the implementation for a finite system [53]. We direct the reader to Ref. [14, 62] for a thorough review of the DMRG method.

DMRG evolved from the numerical renormalization group (NRG) method of calculating ground states of many-body systems [63]. As an illustration of the NRG approach, we form a Hamiltonian H_{BB} with two blocks of the same size. The blocks are labeled B and the block Hamiltonian is H_B, which contains terms only involving sites contained in B. The Hamiltonian H_{BB} contains terms involving both blocks including inter-block interactions. If we assume that H_B is represented by m many-body states, the Hamiltonian H_{BB} is represented by m^2 many-body states. After the diagonalization of H_{BB}, the m lowest lying eigenstates are kept while the others are discarded. The remaining eigenstates are used as an effective basis for the newly formed larger block $BB \rightarrow B'$. Equivalently, the Hamiltonian H_{BB} is transformed into a Hamiltonian describing a collective single block, $H_{B'}$ via an $m^2 \times m$ transformation matrix O,

$$H_{B'} = O^{\dagger} H_{BB} O. \tag{3.5}$$

The NRG procedure is repeated until the system is sufficiently large. Although the NRG method was successfully applied to impurity systems, it failed to produce accurate results for many other systems. A notorious failure involved the ground state calculation of a single particle in a box. Consider constructing a system with two equal subsystems A, as shown in Fig. 3.1. The eigenstates of system A vanish at the edges. No possible linear combination of the eigenstates of A on the

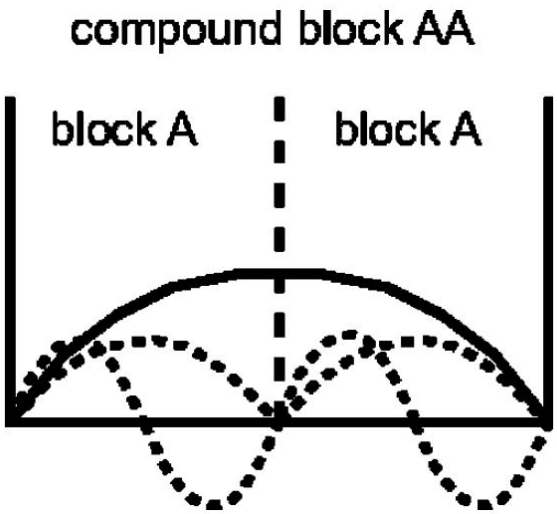

Figure 3.1: Failure of the NRG algorithm to construct the single particle wave function in a box. The eigenstates of the smaller block A vanish at its edges. Therefore, they cannot be used to contstruct the ground state of block AA [Taken from U. Schollwöck, Rev. Mod. Phys. **77**, 259 (2005).]

left can be glued to the eigenstates of A on the right in order to form the true ground state of the system AA. The need for the improvement of the NRG method due to its shortcomings helped to initiate the development of DMRG.

The DMRG method for a 1D infinite system with reflection symmetry begins with a block B_ℓ of ℓ sites and Hamiltonian H_{B_ℓ} which contains local and interaction terms involving only sites belonging to block B_ℓ. One then enlarges the system by constructing a superblock $B_\ell \bullet \bullet B_\ell^R$ and corresponding Hamiltonian: the superblock of size $2\ell + 2$ is formed by connecting to B_ℓ two additional sites and another block B_ℓ^R, which is a reflection of B_ℓ. The Hamiltonian of this superblock is diagonalized, using for example the Lanczos algorithm described in Appendix (A.1), and the ground state is obtained (or "targeted") $|\psi_{\rm gr}\rangle$. We assume that the superblock is chosen to be small enough that the Hamiltonian can be diagonalized. The following step is at the core of the DMRG method. The system is partitioned between the two free sites. The reduced density matrix of the enlarged left block $B_\ell\bullet$ is formed from the ground state,

$$\rho_{\ell+1} = \mathrm{Tr}_{\bullet B_\ell^R} |\psi_{\rm gr}\rangle\langle\psi_{\rm gr}|, \tag{3.6}$$

where the degrees of freedom of the right enlarged block (called "environment block") $\bullet B_\ell^R$ are traced out. After the diagonalization of the reduced density matrix, a fixed number $m < \dim(B_\ell \bullet)$ of eigenstates associated with the largest eigenvalues are kept. In effect, the Hilbert space is truncated and the states removed in the procedure introduce a "discarded weight", $\sum_{\alpha>m} \lambda_\alpha^2$, of the ground state computation. Indeed, the speed of the computation is determined by how many states are kept. In the DMRG algorithm, one has the choice to either fix the truncation to m states or fix the discarded weight at every iteration. The m eigenstates now form a new basis of the enlarged block $B_\ell \bullet \rightarrow B_{\ell+1}$ and Hamiltonian $\overline{H}_{B_{\ell+1}} = \mathbf{O}^\dagger H_{B_{\ell+1}} \mathbf{O}$, where $\mathbf{O}$ is a $\dim[B_\ell \bullet] \times m$ rectangular transformation matrix containing the density-matrix eigenstates kept. The DMRG method is now iterated by using the new block $B_{\ell+1}$ to form the superblock configuration with system size $2\ell + 4$. The beginning steps of the DMRG algorithm are illustrated in figure 3.2.

When reflection symmetry is no longer assumed, the build-up process of the DMRG algorithm is different. In this case, one begins with a block B of ℓ sites and forms, for example, a superblock configuration $B\bullet\bullet\bullet$ of $\ell+3$ sites. The system is partitioned such that the two individual sites located to the right of the enlarged block $B_\ell \bullet \rightarrow B_{\ell+1}$ now form the environment block. Each subsequent iteration then involves growing the system size by adding an environment block consisting of two sites. When the build-up procedure stops at a finite size, there is no guarantee that the algorithm resulted in a good approximation of the ground state wave function. In order to obtain a better ground state approximation, the procedure can be adapted for systems of fixed size while the bipartition point is shifted at each iteration.

As an illustration of the finite system method, we assume reflection symmetry even though the method can be generalized to systems lacking this symmetry. Suppose we start at $\ell = 1$. During the build-up process, all block Hamiltonians $\overline{H}_{\mathrm{B_1}}$,..., $\overline{H}_{\mathrm{B_{L/2}}}$ are saved to memory along with all the basis transformations $\mathbf{O}$ and interaction operators that connect the blocks. The finite system procedure then continues by forming a superblock configuration $B_{L/2} \bullet \bullet B_{L/2-2}^R$ using the reflection of $B_{L/2-2}$ saved during the infinite system build-up. The algorithm proceeds as described above in obtaining $B_{L/2+1}$, *i.e.*, calculating the reduced density matrix eigenstates, performing the

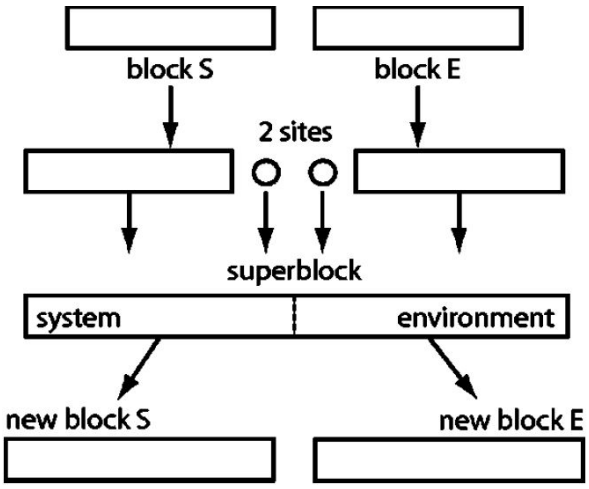

Figure 3.2: The first several steps of the DMRG algorithm are illustrated above. In this illustration, the algorithm grows the system by adding two free sites. This forms a superblock configuration $S\bullet\bullet E$. This is followed by an exact diagonalization of the superblock hamiltonian in order to obtain the ground state $|\psi_G\rangle$. The reduced density matrix of the extended left block (which consists of the left block and the next site over) is calculated and only m eigenstates are chosen. The chosen eigenstates are then used to as the basis for the enlarged blocks. [Taken from U. Schollwöck, Rev. Mod. Phys. **77**, 259 (2005).]

truncation, and transforming the basis. One then continues by moving the bipartition point (a process called "sweeping") across the system of fixed size forming superblock configurations $B_i \bullet \bullet B^R_{L-i-2}$, where $i = 1, \ldots, L-3$. One full sweep occurs when the points of bipartition move from one end of the system to the other and back. Typically, it takes five to ten sweeps for good results. Afterwards, the final wave function can be used to calculate all observables and correlation functions.

In the discussion above, we focused on the calculation of the ground state. However, the algorithm can be extended to the calculation of excited states. After the diagonalization of the superblock Hamiltonian during each iteration, multiple states rather than just $|\psi_G\rangle$ can be used to construct the density matrix,

$$\rho = \sum_n w_n |\psi_n\rangle\langle\psi_n|, \tag{3.7}$$

where the target states $|\psi_n\rangle$ are weighted with the factor w_n which must satisfy the normalization, $\sum_n w_n = 1$. In practice, the weights usually are equal. In addition, more reduced density-matrix

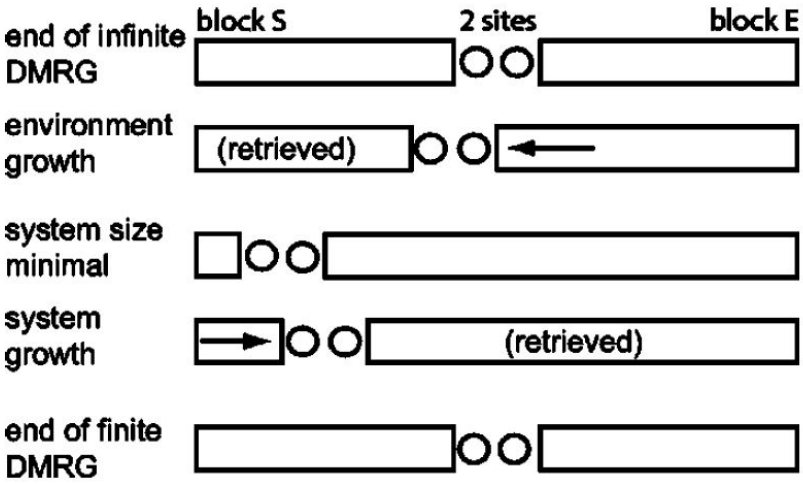

Figure 3.3: A half sweep of the finite system DMRG procedure is illustrated above. [Taken from U. Schollwöck, Rev. Mod. Phys. **77**, 259 (2005).]

eigenstates are needed during the procedure to accurately represent the target states (i.e., maintain a similar discarded weight). In general, approximately the same number of density-matrix eigenstates are needed for every additional target state. For example, 1D Hubbard systems with open boundary conditions for one target state and size $L = 768$ have been implemented in reference [62]. Keeping up to $m = 800$ density-matrix eigenstates resulted in a discarded weight of $< 10^{-6}$. In order to maintain a similar discarded weight for three target states, the same Hubbard system was implemented up to size $L = 256$. We will see below that a widely used DMRG method of the time evolution of a wave function requires multiple target states.

3.2.2 Adaptive Time-Dependent DMRG

Consider at time t_0, the ground state $|\psi(t_0)\rangle$ of a finite system is computed using the standard DMRG procedure. We are now interested in calculating the wave function at some later time t, which has evolved under a different time-dependent Hamiltonian $\hat{H}(t)$ of which $|\psi(t_0)\rangle$ is no longer an eigenstate. The time evolution of a quantum state is given by the time-dependent Schrödinger

equation,

$$i\frac{d}{dt}|\psi(t)\rangle = \hat{H}(t)|\psi(t)\rangle. \tag{3.8}$$

The equation can be numerically integrated using for example Runge-Kutta, Crank-Nicholson, or Lanczos schemes [64] to determine the state $|\psi(t)\rangle$ at some later time. Alternatively, one can explicitly construct the propagator $\hat{U}$, where

$$|\psi(t)\rangle = \hat{U}|\psi(t)\rangle. \tag{3.9}$$

We will defer the latter treatment of the time evolution to the section discussing the TEBD algorithm below. One of the first extensions of the DMRG algorithm to time evolution consisted of evolving the ground state, which was computed from the standard DMRG method, by numerically integrating the Schrödinger equation at a fixed basis [65]. Recall that the restricted Hilbert space was generated by the last DMRG step of the ground state computation. In performing the numerical integration, one must assume that the time-evolved state $|\psi(t)\rangle$ is accurately approximated within the same restricted Hilbert space at times from t_0 to the final time t. This method did not work very well since it was restricted to very short times before states outside the restricted Hilbert space are evoked during the dynamics.

An improvement of this method was suggested by Luo *et al.* [66, 67]. In this new method, the target states spanned the entire evolution time during each DMRG step. However, increasing the number of targets states required increasing the number of density matrix eigenstates in order to keep a low discarded weight. The approach was too computationally slow as it required a large basis for the whole evolution to be performed at every DMRG step. An additional improvement to the method of time evolution is called the adaptive time-dependent DMRG. In this method, the wave function is targeted at multiple times between t_0 and $t_0 + \delta t$ of a single time step. This way the density matrix basis is optimized to represent the state at time t_0 and at later times. The restricted Hilbert space is then updated by the density matrix,

$$\rho = \sum_{i=0}^{n} w_i |\psi(t_0 + i\delta t/n)\rangle\langle\psi(t_0 + i\delta t/n)|, \tag{3.10}$$

for the time interval δt. The weights w_i are typically chosen to be equal ($w_i = 1/n$). As an illustration of the time evolution procedure, we choose to advance the time step δt after each half sweep by using the Lanczos method. At each step of the half sweep, (*i.e.*, over a single bipartition) the targeted states are $|\psi(t_0)\rangle$ and $|\psi(t_0+\delta t)\rangle$. The additional target state is calculated by evolving the state $|\psi(t_0)\rangle$ in the Lanczos basis [see appendix A.1 for definitions],

$$|\psi(t_0+\delta t)\rangle = V_m(t_0)e^{-i\delta t T_m(t_0)}V_m^T(t_0)|\psi(t_0)\rangle. \tag{3.11}$$

The density matrix is then calculated using Eq. (3.10) and a chosen amount m of density matrix eigenstates are kept. Only after all the steps of the half sweep are completed, the wave function advances over an interval δt.

Another method for time evolution was developed by Vidal and is called time-evolving block decimation (TEBD). This method, which used insight from quantum information theory, represented an adaptive method (in the DMRG language) of time evolution [68]. During the time evolution, the propagator $\hat{U}(t)$ is decomposed in such a way suitable for dynamically updating the elements of the matrix product state representation of the many-body state. In the next section, we review this matrix product state representation.

3.3 Time Evolution Block Decimation Algorithm (TEBD)

3.3.1 Matrix Product State

In this section, we review the state decomposition in a system of n sites based on the arguments presented in Ref. [15, 69]. The matrix product decomposition allows for an efficient and transparent computation of the operations acting on the state. When we later consider the time evolution by expanding the propagator, the matrix product decomposition becomes a natural representation to work with. The decomposition is made by taking SVDs after successive partitions made at each bond. Consider a 1D chain of n sites. A state in general can be written in the basis

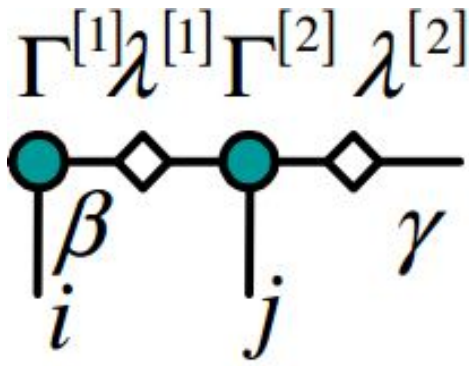

Figure 3.4: Illustration of the matrix product state essential in the TEBD algorithm. The Gamma tensors, Γ, rest on sites and the lambdas, λ, rest on bonds. [Taken from G. Vidal, Phys. Rev. Lett. **98**, 070201 (2007).]

of the direct product of all the single-site basis states,

$$|\Psi\rangle = \sum_{i_1,i_2,\ldots,i_n} c_{i_1 i_2 \ldots i_n} |i_1\rangle \otimes |i_2\rangle \otimes \ldots \otimes |i_n\rangle,$$

where we will let d denote the single-site Hilbert space dimension. The $c_{i_1 i_2,\ldots}$ coefficients can then be decomposed as a product of tensors,

$$c_{i_1 i_2 \ldots i_n} = \sum_{\alpha_1,\ldots,\alpha_2} \Gamma^{[1]i_1}_{\alpha_1} \lambda^{[1]}_{\alpha_1} \Gamma^{[2]i_2}_{\alpha_1\alpha_2} \lambda^{[2]}_{\alpha_2} \Gamma^{[3]i_3}_{\alpha_2\alpha_3} \cdots \Gamma^{[n]i_n}_{\alpha_{n-1}}, \tag{3.12}$$

where the indices α_j take values from 1 to the Schmidt rank χ, the Γ's are tensors that correspond to each site, and the singular values λ are obtained from a Schmidt decomposition of the state performed at every bond. The illustration of the decomposition is shown in Fig. 3.4. The derivation starts with a partition between the first $|i_1\rangle$ and second sites $|i_2 \ldots i_n\rangle \equiv |j^{[2\ldots n]}\rangle$ followed by a Schmidt decomposition,

$$|\Psi\rangle = \sum_{\alpha_1}^{\chi} \lambda^{[1]}_{\alpha_1} |\phi^{[1]}_{\alpha_1}\rangle |\phi^{[2\ldots n]}_{\alpha_1}\rangle, \tag{3.13}$$

where the Schmidt vectors $|\phi^{[1]}_{\alpha_1}\rangle = \sum_{i_1} \Gamma^{[1]i_1}_{\alpha_1} |i_1\rangle$ and $|\phi^{[2\ldots n]}_{\alpha_1}\rangle = \sum_j V^*_{j\alpha_2} |j^{[2\ldots n]}\rangle$. The $\Gamma^{[1]} = U$ and $V^\dagger$ are derived from the SVD of $c_{i_1,j}$. We rewrite the second Schmidt vector in terms of a partition between the second and third site thereby isolating the second site,

$$|\phi^{[2\ldots n]}_{\alpha_1}\rangle = \sum_{i_2} |i_2\rangle |\tau^{[3\ldots n]}_{i_2\alpha_1}\rangle. \tag{3.14}$$

We can write the unnormalized vector $|\tau_{i_2\alpha_1}^{[3\ldots n]}\rangle$ as a linear combination of Schmidt vectors and corresponding singular values,

$$|\tau_{i_2\alpha_1}^{[3\ldots n]}\rangle = \sum_{\alpha_2} \Gamma_{\alpha_1\alpha_2}^{[2]i_2} \lambda_{\alpha_2}^{[2]} |\phi_{\alpha_2}^{[3\ldots n]}\rangle. \tag{3.15}$$

In terms of the new coefficients, the many-body state now has the following form,

$$|\Psi\rangle = \sum_{\alpha_1\alpha_2}^{\chi} \Gamma_{\alpha_1}^{[1]i_1} \lambda_{\alpha_1}^{[1]} \Gamma_{\alpha_1\alpha_2}^{[2]i_2} \lambda_{\alpha_2}^{[2]} |i_1\rangle|i_2\rangle|\phi_{\alpha_2}^{[3\ldots n]}\rangle. \tag{3.16}$$

The procedure continues until $c_{i_1\ldots i_n}$ is of the form in Eq. (3.12). The above argument provides a proof of existence of the matrix product state representation of c; however, it does not explicitly provide a computational recipe for calculating the Γ tensors. Also, if the singular values determined from a SVD are found to be degenerate, the matrix product state representation is no longer unique. The computation of the Γ's is performed by computing the SVD of all possible bipartitions of the state. As an example, suppose we consider the SVD of the bipartition at the second and third sites,

$$|\Psi\rangle = \sum_{\alpha_2} \lambda_{\alpha_2}^{[2]} \Gamma_{\alpha_2}^{[12]i_1i_2} |i_1i_2\rangle \Gamma_{\alpha_2}^{[3\ldots n]i_3\ldots i_n} |i_3\ldots i_n\rangle, \tag{3.17}$$

where by notation, $\Gamma^{[12]}$ and $\Gamma^{[3\ldots n]}$ correspond to the U and $V^\dagger$ matrices respectively when we introduced the SVD. When we compare this representation for the bipartition at the second and third sites to Eq. (3.16), we obtain the equality,

$$\Gamma_{\alpha_2}^{[12]i_1i_2} = \sum_{\alpha_1}^{\chi} \Gamma_{\alpha_1}^{[1]i_1} \lambda_{\alpha_1}^{[1]} \Gamma_{\alpha_1\alpha_2}^{[2]i_2}. \tag{3.18}$$

From the unitary property of $\Gamma^{[1]}$, the above can be inverted to find the matrix elements $\Gamma_{\alpha_1\alpha_2}^{[2]i_2}$. The other Γ's in Eq. (3.12) can be similarly computed.

To further illustrate the matrix product state representation, we consider an example by expressing the spinwave state on a chain of 4 spins:

$$|\Psi\rangle = \frac{|\uparrow\uparrow\uparrow\downarrow\rangle + |\uparrow\uparrow\downarrow\uparrow\rangle + |\uparrow\downarrow\uparrow\uparrow\rangle + |\downarrow\uparrow\uparrow\uparrow\rangle}{2}$$

We bipartition the system between first and second site, $|\Psi\rangle = \sum_{i_1,j} c_{i_1,j} |i_1\rangle |j^{[234]}\rangle$. Therefore, the c matrix in the ordered basis $\{|\uparrow\rangle, |\downarrow\rangle\}$ and $\{|\uparrow\uparrow\uparrow\rangle, |\uparrow\uparrow\downarrow\rangle, |\uparrow\downarrow\uparrow\rangle, |\uparrow\downarrow\downarrow\rangle, |\downarrow\uparrow\uparrow\rangle, |\downarrow\uparrow\downarrow\rangle, |\downarrow\downarrow\uparrow\rangle, |\downarrow\downarrow\downarrow\rangle\}$

is given by,

$$c = \begin{pmatrix} 0 & 1/2 & 1/2 & 0 & 1/2 & 0 & 0 & 0 \\ 1/2 & 0 & 0 & 0 & 0 & 0 & 0 & 0 \end{pmatrix}. \tag{3.19}$$

From the SVD of c the following are determined,

$$U^{[1]} = \begin{pmatrix} 1 & 0 \\ 0 & 1 \end{pmatrix}, \tag{3.20}$$

where $\Gamma^{[1]i_1}_{\alpha_1} \equiv U^{[1]}_{i_1\alpha 1}$. The right singular vectors are

$$V^{[2]} = \begin{pmatrix} 0 & 1 & 0 & 0 & 0 & 0 & 0 & 0 \\ 1/\sqrt{3} & 0 & 0 & 0 & -1/\sqrt{2} & 0 & 0 & -1/\sqrt{6} \\ 1/\sqrt{3} & 0 & 0 & 0 & 0 & 0 & 0 & \sqrt{2/3} \\ 0 & 0 & 0 & 0 & 0 & 0 & 1 & 0 \\ 0 & 0 & 0 & 0 & 0 & 1 & 0 & 0 \\ 1/\sqrt{3} & 0 & 0 & 0 & 1/\sqrt{2} & 0 & 0 & -1/\sqrt{6} \\ 0 & 0 & 0 & 1 & 0 & 0 & 0 & 0 \\ 0 & 0 & 1 & 0 & 0 & 0 & 0 & 0 \end{pmatrix}, \tag{3.21}$$

where $\Gamma^{[234]j}_{\alpha_1} = [V^{[2]\dagger}]_{\alpha_1 j}$. The Schmidt coefficients are $\lambda^{[1]} = \{\sqrt{3}/2, 1/2\}$. In general for large systems when the entanglement is low between the blocks of a partition, the singular values generally decrease exponentially. Now consider the bipartite splitting at the second and third sites, $|\Psi\rangle = \sum_{j,j'} c_{jj'} |j^{[12]}\rangle |j'^{[34]}\rangle$. The c matrix is

$$c = \begin{pmatrix} 0 & 1/2 & 1/2 & 0 \\ 1/2 & 0 & 0 & 0 \\ 1/2 & 0 & 0 & 0 \\ 1/2 & 0 & 0 & 0 \end{pmatrix}. \tag{3.22}$$

The singular vectors are

$$U^{[2]} = \begin{pmatrix} 1 & 0 & 0 & 0 \\ 0 & 1/\sqrt{2} & 0 & -1/\sqrt{2} \\ 0 & 1/\sqrt{2} & 0 & 1/\sqrt{2} \\ 0 & 0 & 1 & 0 \end{pmatrix}, \tag{3.23}$$

where $\Gamma_{\alpha}^{[12]j} = U_{j\alpha}^{[2]}$ and

$$V^{[2]} = \begin{pmatrix} 0 & 1 & 0 & 0 \\ 1/\sqrt{2} & 0 & 0 & -1/\sqrt{2} \\ 1/\sqrt{2} & 0 & 0 & 1/\sqrt{2} \\ 0 & 0 & 1 & 0 \end{pmatrix}, \tag{3.24}$$

where $\Gamma_{\alpha}^{[34]j} = [V^{[2]\dagger}]_{\alpha j}$. The Schmidt coefficients are $\lambda^{[2]} = \{1/\sqrt{2}, 1/\sqrt{2}, 0, 0\}$. As can already be seen in this example, entanglement present in this state has led to degenerate singular values. In general, more states must be kept in a truncation sheme when entanglement is large. From Eq. (3.18) and the unitary property of the singular matrices, $\Gamma_{\alpha_1\alpha_2}^{[2]i_2}$ is obtained from the inversion,

$$\sum_{i_1} U_{\alpha_1 i_1}^{[1]\dagger} U_{\{i_1 i_2\}\alpha_2}^{[2]} = \lambda_{\alpha_1}^{[1]} \Gamma_{\alpha_1\alpha_2}^{[2]i_2} \tag{3.25}$$

The rest of the Γ's and λ's are obtained similarly. By considering the next partition between sites 3 and 4, $\lambda_{\alpha_3}^{[3]}$ and $\Gamma_{\alpha_3}^{[4]i_4}$ are immediately obtained from the SVD. The final $\Gamma_{\alpha_2\alpha_3}^{[3]i_3}$ is obtained by inverting the expression,

$$\Gamma_{\alpha_3}^{[123]i_1 i_2 i_3} = \sum_{\alpha_2} \Gamma_{\alpha_2}^{[12]i_1 i_2} \lambda_{\alpha_2}^{[2]} \Gamma_{\alpha_2\alpha_3}^{[3]i_3}. \tag{3.26}$$

3.3.2 Local and Two-Site Operators

If the Hamiltonian of the system consists of an external potential and two-body interactions, the time evolution of an initial state can be formulated as a sequence of one-site and two-site operations acting on the state. Before we consider the time evolution, we consider the effect of

one-site and two-site operators on the matrix product representation of the state. When a one-site operator $\hat{A} = \sum_{i_\ell, j_\ell} A_{i_\ell j_\ell} |i_\ell\rangle\langle j_\ell|$ acts on the site ℓ, $\Gamma^{[\ell]}$ is simply modified in the following way,

$$\tilde{\Gamma}^{[\ell] i_\ell}_{\alpha_{\ell-1}\alpha_\ell} = \sum_{j_\ell}^{d} A_{i_\ell j_\ell} \Gamma^{[\ell] j_\ell}_{\alpha_{\ell-1}\alpha_\ell}. \tag{3.27}$$

The two-site operator is in general of the form,

$$\hat{V} = \sum_{i_a, j_b, k_a, m_b} V^{i_a j_b}_{k_a m_b} |i_a j_b\rangle\langle k_a m_b|. \tag{3.28}$$

We will consider only the case when the two sites are adjacent. When the two-site operator acts on two adjacent sites ℓ and $\ell+1$, the new state is computed by first isolating the basis states $|i_\ell\rangle$ and $|i_{\ell+1}\rangle$ from the rest of the system,

$$\begin{aligned} |\Psi'\rangle &= \hat{V}|\Psi\rangle, \\ |\Psi'\rangle &= \sum_{\alpha_{\ell-1}, \alpha_{\ell+1}} \sum_{i_l, i_{l+1}} \Theta^{i_\ell i_{\ell+1}}_{\alpha_{\ell-1}\alpha_{\ell+1}} |\phi^{[1\ldots\ell-1]}_{\alpha_{\ell-1}} i_\ell i_{\ell+1} \phi^{[\ell+2\ldots n]}_{\alpha_{\ell+1}}\rangle, \end{aligned} \tag{3.29}$$

where

$$\Theta^{i_\ell i_{\ell+1}}_{\alpha_{\ell-1}\alpha_{\ell+1}} = \sum_{\beta=1}^{\chi} \sum_{k,l}^{d} V^{i_\ell i_{\ell+1}}_{kl} \lambda^{[\ell-1]}_{\alpha-1} \Gamma^{[\ell] i_\ell}_{\alpha_{\ell-1}\alpha_\ell} \lambda^{[\ell]}_{\alpha_\ell} \Gamma^{[\ell+1] i_{\ell+1}}_{\alpha_\ell \alpha_{\ell+1}} \lambda^{[\ell+1]}_{\alpha_{\ell+1}}. \tag{3.30}$$

The idea is to form a new set of Γ tensors and λ vectors via the SVD. The procedure begins by normalization, $\sum_{\alpha_\ell, i_\ell, i_{\ell+1}, \alpha_{\ell+1}} |\Theta^{i_\ell i_{\ell+1}}_{\alpha_{\ell-1}\alpha_{\ell+1}}|^2 = 1$. Explicit normalization is required for non-unitary operations, for example in the case of the imaginary-time evolution discussed below to compute ground states. The fourth-rank tensor is restructured into a $\chi d \times \chi d$ matrix followed by a SVD, retaining the χ largest singular values $\tilde{\lambda}^{[\ell]}_{\alpha_\ell}$. The truncation error acquired in this step is

$$\epsilon = 1 - \sum_{\alpha_\ell}^{\chi} (\tilde{\lambda}^{[\ell]}_{\alpha_\ell})^2. \tag{3.31}$$

The retained singular values are then normalized $\tilde{\lambda}^{[\ell]}_{\alpha_\ell} \to \frac{\tilde{\lambda}^{[\ell]}_{\alpha_\ell}}{\sqrt{\sum_{\alpha_\ell}^{\chi} (\tilde{\lambda}^{[\ell]}_{\alpha_\ell})^2}}$. The third-rank tensors $\tilde{\Gamma}^{[\ell]}_{\alpha_{\ell-1}\alpha_\ell}$ and $\tilde{\Gamma}^{[\ell+1]}_{\alpha_\ell\alpha_{\ell+1}}$ are the left and right singular vectors of the SVD, respectively.

3.3.3 Time Evolution

Consistent with the discussion of the two-site operators, the time evolution of the many-body state using the TEBD algorithm is restricted to Hamiltonians (possibly time-dependent)

containing only an on-site term and nearest neighbor coupling. These Hamiltonians have the form $\hat{H} = \sum_{\text{odd}i}(h_{i,i+1} + h_i) + \sum_{\text{even}i}(h_{i,i+1} + h_i) \equiv \hat{G} + \hat{F}$ where $[\hat{G}, \hat{F}] \neq 0$. The time evolution of a state is

$$|\Psi(t)\rangle = e^{-i\hat{H}t}|\Psi_{\text{initial}}\rangle. \tag{3.32}$$

While the propagator has non-commuting terms, it can be separated while incurring a second-order Trotter error,

$$e^{-i\hat{H}t} = e^{-i\hat{F}t/2}e^{-i\hat{G}t}e^{-i\hat{F}t/2} + \mathrm{O}[t^2]. \tag{3.33}$$

The expansion is called a second order Suzuki-Trotter decomposition [70] and the Trotter error can be controlled by performing a higher order decomposition or decreasing the time step. The expansion of the propagator in this way is useful since all the terms in $\hat{F}(\hat{G})$ commute with each other, thereby simplifying the computation for the matrix elements of the propagator. The propagation is then depicted by a sweep across the system. Particularly, the even terms are updated at half a time step followed by the odd terms by a whole time step. The even terms are then updated again over the remaining half time step. The action of each of these terms represents the action of a nearest neighbor two-site operator described in the previous section. The operator acting on the state has been shown to update the matrix product decomposition in such a way that the basis states change. In the DMRG language, the basis states are adapted after each step of the sweep. Although we have described the propagation method in the context of a real-time evolution, ground state calculations of a Hamiltonian $\hat{H}$ can be performed via an imaginary-time evolution of a random state $|\psi_0\rangle$ which has significant overlap with the ground state,

$$|\Psi_{\text{gs}}\rangle = \lim_{\tau\to\infty} \frac{e^{-\hat{H}\tau}|\psi_0\rangle}{||e^{-\hat{H}\tau}|\psi_0\rangle||}. \tag{3.34}$$

In the implementation, the ground state energy is assumed to be positive. Otherwise, one can introduce a constant energy shift so that this condition is satisfied. Over the course of the imaginary time evolution, the ground state becomes the dominating term over sufficiently long times because the term with the smallest weight $e^{-E_{\text{gs}}t}$ decays the slowest. The initial random state can be

prepared as a product state of all state configurations weighted equally, $c_{i_1 \ldots i_n} = 1/\sqrt{d}^n$ for all i_ℓs resulting in a decomposition,

$$\begin{aligned} \Gamma^{[\ell]}_{\alpha_{\ell-1}\alpha_\ell} &= \frac{1}{\sqrt{d}} \delta_{\alpha_{\ell-1},1} \delta_{\alpha_\ell,1}, \\ \lambda^{[\ell+1]}_{\alpha_\ell} &= \delta_{\alpha_\ell,1}. \end{aligned} \tag{3.35}$$

In practice, the implementation of the imaginary-time evolution is different from that of the real-time evolution. The real-time evolution consists of unitary operations which preserve the orthonormality of the the Schmidt vectors $\{|\phi^{[\ell]}_\alpha\rangle\}$ and $\{|\phi^{[\ell+1]}_\alpha\rangle\}$. However, the imaginary-time evolution is not a unitary operation and, furthemore, it is more inclined to not conserve quantum numbers like, magnetiziation and particle number. There are two approaches to deal with the former issue. One solution is tailored specifically for imaginary-time evolution, while the other approach is a solution to dealing with any non-unitary operation. The former approach is a reordering of the imaginary-time evolution. In the second order Trotter-Suzuki decomposition of the propagator, the sweep across the system begins with $(1,2)$, $(3,4)$, $(5,6)$, and so on. During the imaginary-time evolution, the two-site operation acting on sites ℓ and $\ell+1$ only explicitly orthogonalizes the set of Schmidt vectors $\{|\phi^{[1\ldots\ell]}_{\alpha_\ell}\}$ and $\{|\phi^{[\ell+1\ldots n]}_{\alpha_\ell}\}$. However, orthogonality is lost in the states $\{|\phi^{[1\ldots\ell+1]}_{\alpha_\ell}\}$. So that in the next step of the sweep, when the operator acts on $\ell+2$ and $\ell+3$, the previous Schmidt vectors are no longer orthogonal [69]. By reordering the evolution to a time sweep $(1,2)$, $(2,3)$, $(3,4)$, and so on, the Schmidt vectors remain orthogonal in the previous step of the sweep and are explicitly orthogonalized in the current step. The second approach is a general method for all nonunitary operations. Nonunitary operations different from that presented in the above discussion are swapping techniques required for systems with periodic boundary conditions [54]. Suppose we have a nonorthogonal splitting,

$$|\Psi\rangle = \sum_{\alpha_\ell} |\phi^{[1\ldots\ell]}_{\alpha_\ell}\rangle |\phi^{[\ell+1\ldots n]}_{\alpha_\ell}\rangle, \tag{3.36}$$

such that $\langle\phi^{[1\ldots\ell]}_{\alpha'_\ell}|\Psi\rangle = A_{\alpha_\ell,\alpha'_\ell}$ and $\langle\phi^{[\ell+1\ldots n]}_{\alpha'_\ell}|\Psi\rangle = B_{\alpha_\ell,\alpha'_\ell}$. After performing a SVD of both matrices $A = U^{[A]}\lambda^{[A]}V^{[A]\dagger}$ and $B = U^{[B]}\lambda^{[B]}V^{[B]\dagger}$, the state $|\Psi\rangle$ can be written in terms of the new set of

vectors,

$$|\Psi\rangle = \sum_{nm} (X^T Y)_{nm} |e_n\rangle |f_m\rangle, \tag{3.37}$$

where $|e_n\rangle = \sum_\alpha X^\dagger_{n\alpha} |\phi^{[A]}_\alpha\rangle$ and $|f_m\rangle = \sum_\alpha Y^\dagger_{m\alpha} |\phi^{[B]}_\alpha\rangle$ are orthonormal vectors. From this representation, one performs a SVD of the matrix $X^T Y$ to obtain the new orthogonal Schmidt vectors.

3.4 Summary

In this chapter, we discussed the mechanisms underlying the DMRG and TEBD algorithms. In the ensuing chapters, we will present results mostly obtained from the adaptive t-DMRG method when applied to the 1D Bose-Hubbard and spin systems.

In Chapter 4, we will analyze the transport properties of a lattice system of strongly interacting bosons in a strong linear potential. Different approaches for the treatment of the dynamics of the Bose-Hubbard system will be applied. For systems small enough, the computation of the time evolution is obtained by fully diagonalizing the Hamiltonian matrix. For larger systems, a Krylov-space approach is made to the time evolution in the framework of exact diagonalization (Krylov-ED). For the largest system sizes treated, we apply the Krylov-space variant of the adaptive t-DMRG. In all cases, a cutoff is made in the local bases on the lattice sites of up to 3 bosons per site. In the Krylov-ED approach [71, 72, 73, 74], we approximate the time evolution operator in a basis of $m = 10$ Lanczos vectors and use a time step of $\Delta t = 0.0005$ for the Bose-Hubbard model. The resulting error on the time scales treated is typically of the order of machine precision, and we can treat systems up to 15 sites with 8 particles. With the adaptive t-DMRG, we aim for a discarded weight $< 10^{-9}$ and keep up to $m = 500$ density-matrix eigenstates during the time evolution. For the BHM, we use a time step $\Delta t = 0.0005$ and find at the end of the time evolutions a discarded weight $\lesssim 10^{-7}$. The effective spin models are much easier to treat, and we apply a time step of $\Delta t = 0.005$, resulting in a discarded weight of $< 10^{-9}$ at the end of the time evolution for our largest system size of $L = 50$ sites.

In Chapter 5, we investigate soliton stability under quantum fluctuations in a lattice system of

strongly interacting particles. We compute the time evolution by applying a Krylov-space variant of the adaptive t-DMRG of the system represented by an XXZ-spin Hamiltonian. During the evolution, we keep up to 1000 density-matrix eigenstates for systems with up to L = 100 sites. We apply a time step of $\Delta t = 0.05$, resulting in a discarded weight of $< 10^{-9}$ at the end of the time evolution. We estimate the error bars at the end of the time evolution to be smaller than the size of the symbols in the displayed plots in both, Chapters 4 and 5.

Chapter 4

Resonant non-Equilibrium Dynamics under a Strong Linear Potential

This chapter is based on C. Rubbo *et. al.*, Phys. Rev. A 84, 033638 (2011).

In this chapter, we investigate the tunneling dynamics of ultracold bosons loaded on a tilted 1-D optical lattice, with the goal of introducing a transport scheme of atoms in these systems. The system is described by the Bose-Hubbard model (BHM) introduced in Chapter 2 with an external linear potential. The dynamics for sufficiently small systems are obtained via analytic and time-dependent exact diagonalization. In particular, when the systems are too large for exact analysis, the numerical results are obtained via density matrix renormalization group methods discussed in Chapter 3.

Previous studies aiming to enhance transport on optical lattices have mainly focused on the regime of weak interactions in which the particles are delocalized along the system [75, 76, 77, 78]. One reason for this is that strong interactions tend to localize particles and thus inhibit transport. In this case, the tunneling energy cannot overcome particle interactions and transport is forbidden due to energy conservation. Nevertheless, quantum transport in the strongly interacting regime has attracted some interest [79, 80, 81, 82]. This chapter addresses directly the problem of enhancing transport of particles through a lattice system by considering the strongly interacting regime of the repulsive BHM with an external linear potential. By resonantly tuning the strength of the linear potential, by adjusting the bias between adjacent wells to allow tunneling within the lowest band, it is possible to highly control and understand, even analytically, the complicated many-body dynamics. The assumption is made of a deep enough lattice with suppressed interband tunneling

due to a large band gap. Based on this understanding, an approach is proposed for enhancing transport, which is called the 'slinky scheme' due to the peculiar nature of the resulting motion.

In addition to studying BO and transport properties, strongly interacting bosons on a tilted lattice at commensurate fillings have been predicted to be a very fruitful system for the investigation of quantum magnetism in Ising models and quantum phase transitions [83]. The underlying idea is to map the doublon-hole excitations of a Mott insulator onto an effective spin degree of freedom when the applied tilt is tuned resonantly to the doublon interaction energy. Just recently the observation of the associated quantum Ising transition has been reported in the laboratory [84], leading to proposals for the realization of other systems, *e.g.*, quantum dimer models [83, 85]. These experiments also motivate the study of the time evolution in the resulting spin systems which is done here by comparing dynamics of the center of mass (CM) oscillations of both the BHM and the effective Ising system.

The chapter is organized as follows: In Section 4.1, we introduce the non-equilibrium set-up and the mechanisms underlying the BO. In Sections 4.2 and 4.3 we discuss the center of mass motion at commensurate and incommensurate fillings of the lattice, respectively. In particular, we first provide a pedagogical example of resonantly enhanced tunneling on a double well system and then generalize the analysis to larger systems at commensurate filling using the effective spin mapping (Section 4.2). We then explain how the spin mapping can be indirectly applied to describe the incommensurate case dynamics by projecting onto small clusters (Section 4.3). In Section 4.4 we discuss the numerical results obtained via exact diagonalization and adaptive t-DMRG. We discuss a possible signature of the critical point of the spin system in the amplitude of the CM oscillations in Section 4.4.2. In Section 4.5 we discuss an enhanced transport scheme.

4.1 Bloch Oscillations

The model is the BHM with an external tilt applied to the lattice,

$$H = -J \sum_{\langle i,j \rangle} \hat{a}_i^\dagger \hat{a}_j + \frac{U}{2} \sum_i \hat{n}_i (\hat{n}_i - 1) + \Omega \sum_i i\, \hat{n}_i , \tag{4.1}$$

with Ω the strength of the tilting potential. The properties of this model with only the first and second terms were studied in Chapter 2. In the first term, the angled brackets $\langle\rangle$ represent a sum over nearest neighbors. This single-band model with a linear potential represents a good approximation in the presence of a deep lattice which prevents inter-band transitions and decay of the atoms out of the lattice [86]. There are several ways of realizing the tilted lattice in experiments. For example, it is possible to exploit the gravitational potential by creating a vertical optical lattice, or to detune the counter-propagating laser-beams forming the optical lattice. In the latter case, a time dependent detuning $\delta\mu(t)$ can lead to an acceleration in the lattice depending on the induced velocity $v(t) = \lambda\delta\mu(t)/2$ [21], with λ the wavelength of the laser. A detuning that linearly depends on time will provide a constant acceleration of the lattice. In another method to create a linear potential, a magnetic field gradient is created [84] so that the energy shift $\sim \mu \cdot B$ of the atom is position dependent.

An important observable for the treatment of the Bloch oscillations is the time evolution of the center of mass (CM) position

$$x_{\rm cm}(t) = \frac{1}{N}\sum_{j}^{L} j\,\langle n_j(t)\rangle, \tag{4.2}$$

with N the total number of particles on the lattice with L sites, and $x_{\rm cm}$ is measured in units of the lattice spacing, *i.e.*, the lattice spacing d in all subsequent calculations, unless otherwise specified, is set to unity. Measuring $x_{\rm cm}$ in the experiments [87, 88, 89, 90, 91] provides not only information on the CM motion and the associated current ($\dot{x}_{\rm cm}(t) = -i\langle[\hat{x}, H]\rangle$, where $\hbar$ is equal to one throughout the chapter) significant to transport properties, but can also provide insights into relevant energy scales in the system. For instance, the CM motion in Bloch oscillations has proven to be an accurate tool for metrology [92, 93, 94].

We review the main properties of a single particle on a tight-binding chain while being subjected to a linear tilt. The wave function in the Wannier basis has the general form $|\phi\rangle = \sum_\ell f_\ell|\ell\rangle$, where $|\ell\rangle$ is the Wannier wave function localized on site ℓ. Plugging this form into Schrödinger's equation with the Hamiltonian given by Eq. (4.1), results in an equation for the

coefficients f_ℓ,

$$-i\frac{df_\ell}{dt} = -J(f_{l+1} + f_{l-1}) + \Omega\ell f_\ell. \tag{4.3}$$

Recall that in the case $\Omega = 0$ and periodic boundary conditions, the coupled equations can be solved by the expression $f_\ell = f_\ell^q e^{-iE_q t}$ where $f_j^q = e^{iqj}/\sqrt{L}$ are Bloch waves. The corresponding tight-binding energy is $E_q = -2J\cos(q)$. For open boundary conditions, $f_j^q = \frac{1}{L+1}\sin(\frac{q\pi j}{L+1})$. For a non-zero Ω, and ansatz $f_\ell = \tilde{f}_\ell e^{-iEt}$, Schrödinger's equation is,

$$\frac{\ell - E/\Omega}{J/\Omega}\tilde{f}_\ell = \tilde{f}_{\ell+1} + \tilde{f}_{\ell-1}. \tag{4.4}$$

The recursion relation of the $\tilde{f}$ is the same as the Bessel function recursion relation,

$$J_{\ell-1}(x) + J_{\ell+1}(x) = \frac{2\ell}{x}J_\ell(x), \tag{4.5}$$

where the Bessel function of the first kind $J_\ell(x)$ should not be confused with the tunnel coupling. The recursive formula establishes the relation

$$\tilde{f}_\ell^n = J_{\ell - E_n/\Omega}(2J/\Omega). \tag{4.6}$$

The associated energy levels are discrete $E_n = \Omega n$ (n is an integer). The eigenstates are called Wannier-Stark states [95, 86], and they are given by $|\phi_n\rangle = \sum_j J_{j-n}(2J/\Omega)|j\rangle$ in the Wannier basis. Due to the properties of the Bessel functions, the nth Wannier-Stark state is localized in the region $|j - n| < 2J/\Omega$. Due to the harmonic-oscillator like spectrum, an initial state centered at $x_{\rm cm}(0)$ [96] exhibits periodic CM oscillations with frequency Ω,

$$x_{\rm cm}(t) = x_{\rm cm}(0) - \frac{2J}{\Omega}\left(1 - \cos\Omega t\right). \tag{4.7}$$

The same behavior is also captured by a semiclassical picture in which the linear potential is treated as a constant force dragging the particle through the Brillouin zone. This treatment leads to a time-dependent value of k and hence to a group velocity and to corresponding CM oscillations of the form

$$\begin{aligned} \dot{k} = \Omega \Rightarrow k(t) = k_0 + \Omega t, \\ v_g(t) = \frac{\partial E(k(t))}{\partial k} \Rightarrow x_{\rm CM}(t) \sim \frac{2J}{\Omega}\cos\Omega t, \end{aligned} \tag{4.8}$$

with $E(k) = -2J\cos(k)$ the dispersion of the system without the external potential.

A system of many non-interacting bosons on the lattice will show the same dynamics. Inter-particle interactions, in contrast, tend to dampen the CM motion. In the weakly interacting regime, interactions lead to underdamped dynamics (see Appendix B.1) [97, 98], while in strong fields they can yield a multitude of interesting phenomena, *e.g.*, BO at interaction-induced frequencies or so-called quantum carpets [99, 100]. In the strongly interacting regime, the CM oscillations are almost completely suppressed. However, time-dependent interactions can in principle stabilize them [101].

In the limit $U \to \infty$, a hard-core constraint is realized which mimics the Pauli exclusion principle since double occupancy is suppressed. As discussed in Chapter 2, in this fermionized regime it is then possible to introduce a Jordan-Wigner transformation which reduces the Hamiltonian to a tight-binding model for non-interacting spinless fermions. Any local observable such as the CM position is identical for spinless fermions and hard-core bosons. If we denote by $|\psi^q(0)\rangle$ the initially populated single particle state with $q = 1, \cdots N$, the evolution of each of them in the basis of Wannier-Stark states reads $|\psi^q(t)\rangle = \sum_n f_n^q\, e^{-in\Omega t}\, |\phi_n\rangle$, with $f_n^q = \langle\phi_n|\psi^q(0)\rangle$. Using the recurrence relation of Bessel functions (see Appendix B.2) for the CM oscillations of N hard-core bosons on an infinite lattice, one obtains

$$x_{\rm cm}(t) = \bar{x} + \frac{2J}{N\Omega} \sum_{q=1}^{N} \sum_n \mathrm{Re}\left[e^{i\Omega t}\, f_n^q\, f_{n+1}^{q*}\right], \tag{4.9}$$

with the average position $\bar{x} = \frac{1}{N}\sum_q \sum_n n|f_n^q|^2$. We find that at larger fillings the motion is suppressed, as demonstrated in Figure 4.1. The simple physical picture for this effect is that as the filling increases, hard-core bosons have on average less space for free motion before they encounter each other. As the system approaches unit filling, particle transport gets fully suppressed along the lattice.

4.2 Resonant Dynamics

In this section we study the CM oscillations at commensurate filling ($N = L$), introduce the concept of resonant dynamics and compare it to the BO. We start the discussion with the

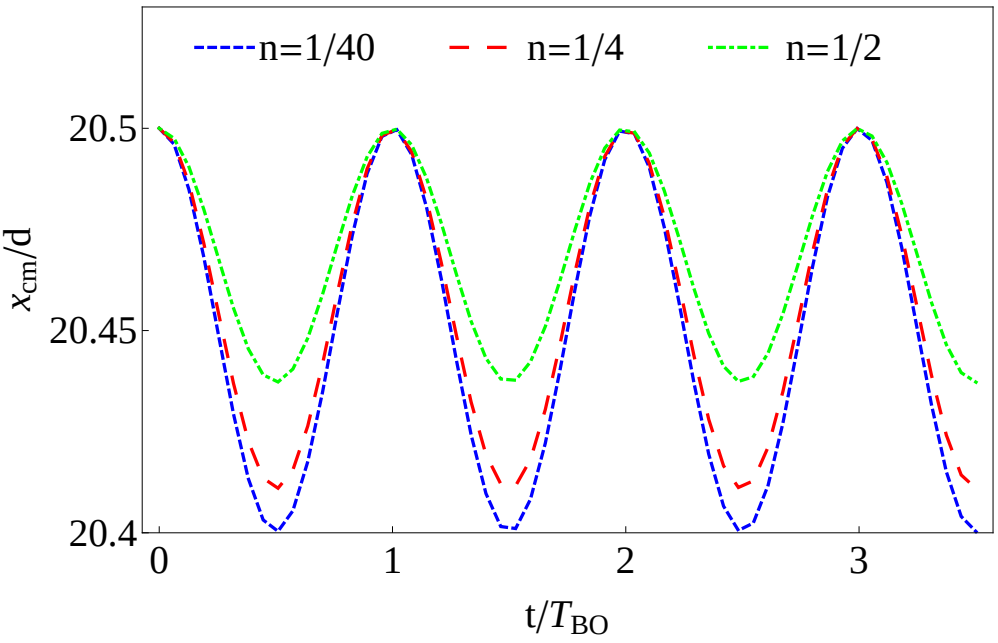

Figure 4.1: Center-of-mass motion due to Bloch oscillations for the BHM Eq. (4.1) in the hard-core limit for different fillings $n = N/L$, where $L = 40$ sites and $\Omega = 40J$. The time evolution is obtained by diagonalizing the corresponding single-particle Hamiltonian and we show results for $n = 1/40$ (Blue, short dashes), $n = 1/4$ (Red, long dashes) and $n = 1/2$ (Green, dashed-dotted line).

pedagogical example of a double-well system with strong interactions $U \gg J$.

4.2.1 A double well potential

We assume that the system is initially in a unit-filled state $|0\rangle \equiv |11\rangle$ with one particle in each well. In the absence of a bias, this "Mott insulating" state is to a good approximation the ground state for $U \gg J$. Excited states are obtained by moving one particle to the other well, *i.e.*, we obtain particle-hole excitations with two particles on one site and no particles in the other. When applying a tilt, the lowest lying excitation is the one in which the two bosons are in the lower potential well. This situation can be modeled by the operator $\hat{d}_i^\dagger = \frac{1}{\sqrt{2}} a_i^\dagger a_{i+1}$, which creates a dipole when applied to the unit-filled ground state of the untilted potential. For a generic bias $\Omega < U$, the particles remain localized on each site, since the hopping can overcome the energy cost of neither the potential nor of the on-site interaction (see the inset of Figure 4.2). However, near resonance ($U = \Omega$), the unit-filled state and the dipole state are nearly degenerate, and so

tunneling from one well to the other is possible.

The time evolution of the double-well system is given by $|\psi(t)\rangle = c_0(t)|11\rangle + c_1(t)|20\rangle + c_2(t)|02\rangle$, and can be obtained analytically by an approach similar to the adiabatic elimination of a non-resonantly coupled excited state in a three-level lambda system [102, 103]. At resonance, perturbation theory shows that the population of the off-resonant state $|02\rangle$ is $\sim J^2/\Omega^2$ and hence for $\Omega \gg J$ remains vanishingly small during the time evolution (see Appendix B.3). To lowest order, the CM motion is approximated by

$$\begin{aligned} x_{\rm cm}(t) &= \frac{(3|c_0(t)|^2 + 2|c_1(t)|^2 + 4|c_2(t)|^2)}{2} \\ &\approx \frac{5}{4} + \frac{1}{4}\cos(2\sqrt{2}Jt) \\ &- \frac{J^2}{8\Omega^2}\left(1 + 7\cos(2\sqrt{2}Jt) + 4\cos(\sqrt{2}Jt)\cos(2\Omega t)\right). \end{aligned} \tag{4.10}$$

The high frequency oscillation $\sim \Omega$ is due to the population of the non-resonant state separated by a large energy difference from the other states (Figure 4.2). Since the population of this state is strongly suppressed, setting $c_2(t) = 0$ is a good approximation. Therefore, all terms $\sim J^2/\Omega^2$ are neglected, including the high frequency oscillations.

This simple double well case illustrates that the time evolution of the system can be obtained in a good approximation by neglecting contributions from non-resonant states. This approximaton will be adopted throughout the rest of the chapter.

4.2.2 Generic case

We now study the behavior of the CM oscillations as a function of U while keeping J and $\Omega \gg J$ fixed. Figure 4.3 summarizes the main results. At $U = 0$ the CM shows BO with amplitude $4J/\Omega$ and frequency Ω. For our choice of J and $\Omega \gg J$ even at $U = 0$ the BO's amplitude is less than one lattice spacing. Upon increasing U, first the amplitude of the BO *decreases* by a factor of more than 2 for $U/\Omega = 0.5$, in accordance with the general expectation that BOs are suppressed in the presence of interactions. However, further increasing U and tuning the system to resonance, $U = \Omega$, leads to *enhanced* CM oscillations. The period of these oscillations scales as J rather than

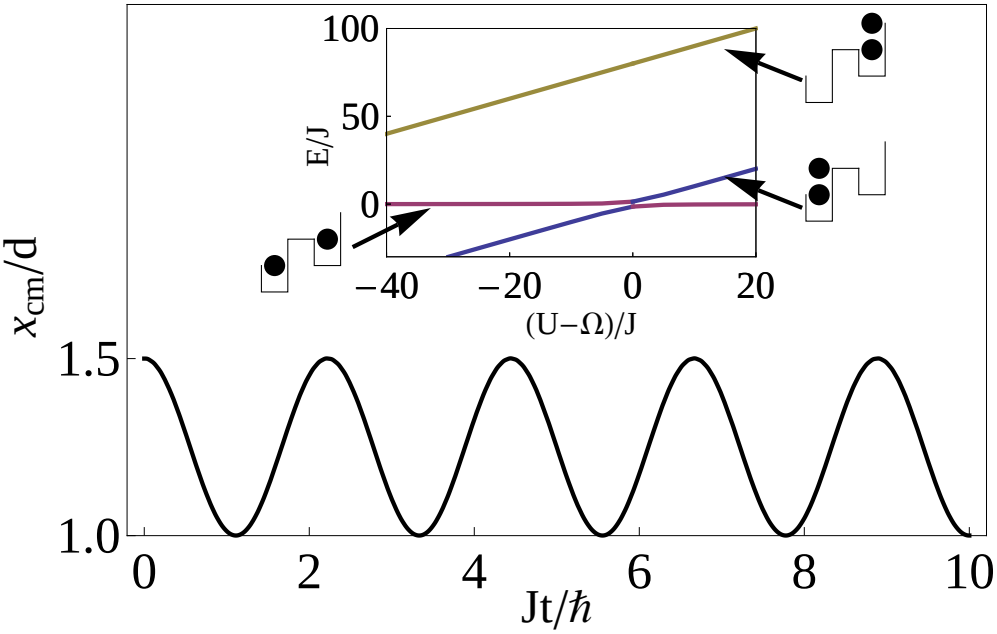

Figure 4.2: CM motion of a double well system at resonance. The inset shows the energy levels of the different states as a function of detuning $(U - \Omega)/J$.

Ω, as in the case of BOs, indicating that the mechanism underlying the dynamics is very different from the one of the BOs [104]. Note that even though the amplitude of the CM oscillations is maximal at resonance, it is $\leq 1/2$ lattice spacings, regardless of the system size. This is due to the fact that the bosons are restricted to hop only between nearest neighboring sites. Since we analyze the resonance situation deep in the Mott-insulating regime, we require strong fields $\Omega \gg J$.

4.2.3 Resonance and the Effective spin model

At resonance the dynamics is obtained by restricting to the set of dipole excitations that are degenerate in energy to zeroth order in the hopping. We display an example for such a resonant family of states in Figure 4.4. Interestingly, these states have a representation in terms of an effective spin language which we discuss below. In this picture, the resonant states map to all spin configurations, excluding the ones containing two adjacent $|\uparrow\rangle$ states. The equilibrium properties of this resonant family of states have been derived in Ref. [83]. For the sake of clarity, we summarize them below.

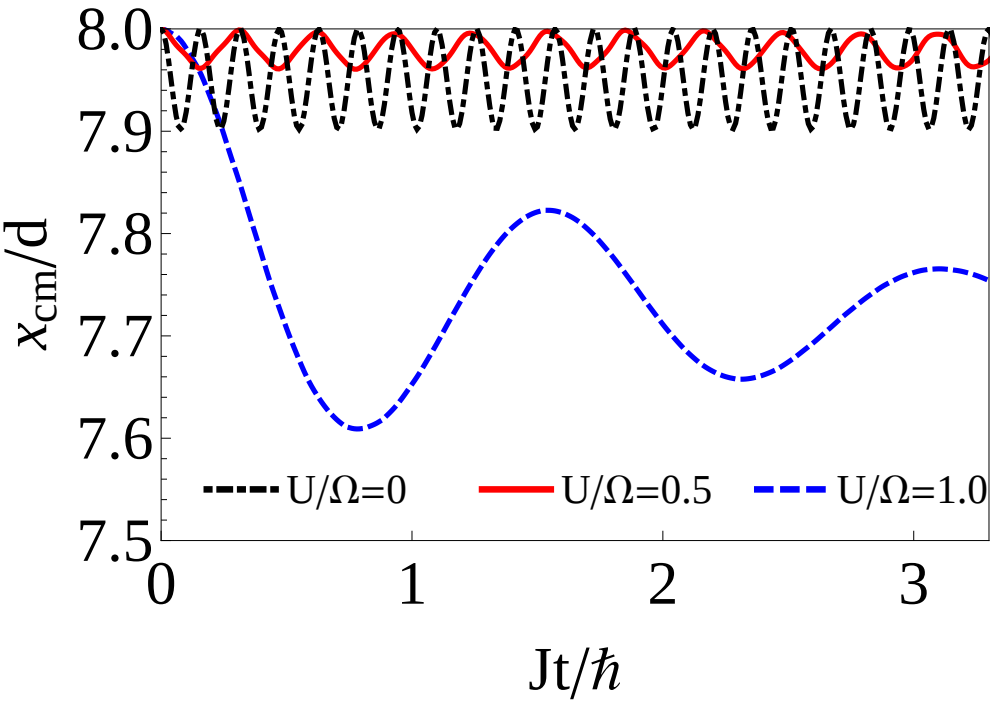

Figure 4.3: CM motion for a BHM at commensurate filling with $L = 15$ lattice sites for $J = 1$, $\Omega = 40$ and three different values of U. The results at $U = 0$ are obtained by diagonalizing the single particle problem, the results at finite U are obtained by adaptive t-DMRG, with a discarded weight $< 10^{-9}$ at the end of the time evolution. The results for the non-interacting system show the frequency Ω and the amplitude $2J/\Omega$ of the BO, while at resonance the frequency is $\sim J$ and the amplitude gets strongly enhanced.

We work in the effective basis obtained by all possible coverings of the system by dipoles, spanned by all combinations $|M;\vec{k}\rangle = \prod_{i=1}^{M} \hat{d}^{\dagger}_{k_i}|0\rangle$, where $|0\rangle$ is the initial Mott-insulating state with one particle per site and M the number of dipoles in the system; the vector $\vec{k}$ contains the positions of the M dipoles on the system. Note that two hard-core constraints appear: first, by construction, two dipoles cannot occupy the same site, leading to an on-site hard-core constraint. Second, it is not possible to realize two dipoles on adjacent sites, since the creation of the second dipole would destroy the first one, leading to a nearest-neighbor hard-core constraint. Taking both constraints into account, the effective Hamiltonian [83]

$$H_{\text{eff,dip}} = -J\sqrt{2}\sum_i (\hat{d}^{\dagger}_i + \hat{d}_i) + (U-\Omega)\sum_i \hat{d}^{\dagger}_i \hat{d}_i \tag{4.11}$$

is obtained. This model can be further mapped to a $S = 1/2$ Ising model in a longitudinal and

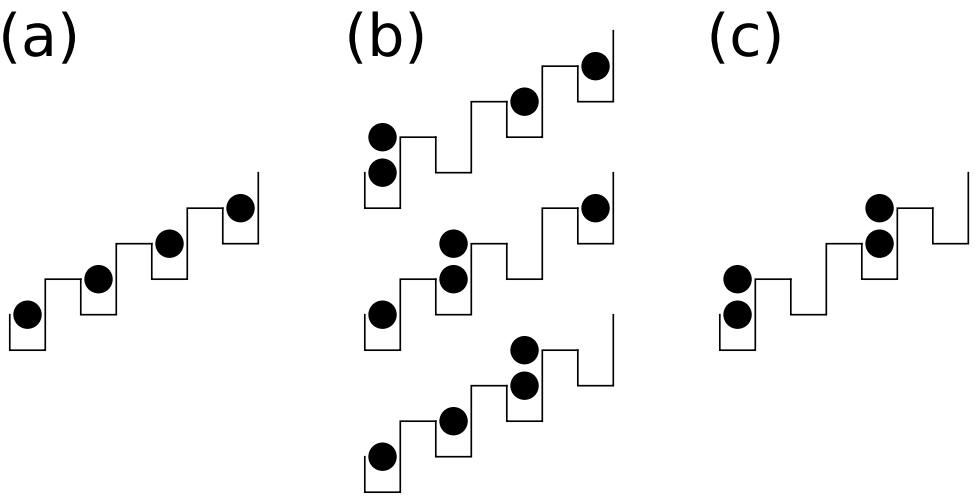

Figure 4.4: Connected resonant family of states for a system with $L = 4$ lattice sites at commensurate filling. The Mott-insulating state in (a) is degenerate in energy to zeroth order in J to the state configurations with one dipole excitation in (b) and the state configuration with two dipole excitations in (c). In the spin representation, the unit filled state in (a) is represented by $|\downarrow\downarrow\downarrow\rangle$. The configurations in (b) from top to bottom are represented by $|\uparrow\downarrow\downarrow\rangle$, $|\downarrow\uparrow\downarrow\rangle$, and $|\downarrow\downarrow\uparrow\rangle$ respectively. The configuration in (c) is represented by $|\uparrow\downarrow\uparrow\rangle$. Note that in the resonant family of states configurations with two adjacent $|\uparrow\rangle$ states are excluded.

transverse external magnetic field,

$$\begin{aligned} H_{\text{eff}} = &-J\sqrt{2}\sum_i \sigma_i^x + (U-\Omega)\sum_i (\sigma_i^z+1)/2 \\ &+ \Delta\sum_i (\sigma_i^z+1)(\sigma_{i+1}^z+1), \end{aligned} \tag{4.12}$$

by introducing pseudospin raising and lowering operators via the mapping $\hat{d}_l^\dagger \rightarrow \sigma_l^+$ (σ_i^x and σ_i^z are the corresponding Pauli matrices for the spin on site i). This mapping captures the on-site hard-core constraint. The nearest-neighbor hard-core constraint is captured by choosing Δ sufficiently large, so that two neighboring spins cannot simultaneously point up. The quantum critical behavior of this system is governed by a single parameter, $\lambda = \frac{U-\Omega}{J}$, and possesses an Ising critical point at $\lambda_c \approx -1.85$ at which the system undergoes a phase transition from a paramagnet to an antiferromagnet, as discussed in Ref. [83].

In this mapping, the spins are located on the bonds between two sites. In addition, the dimension of the Hilbert space needed to obtain the time evolution via this effective model is

reduced to $\dim(\mathcal{H}) = \sum_{M=0}^{\lfloor L/2 \rfloor} N_M^{(L)} = F(L+1)$, where $N_M^{(L)} = \binom{L-M}{M}$ is the number of states in a system of L sites containing M dipoles and $F(L)$ denotes the L^{th} Fibonacci number. Indeed, the form of $N_M^{(L)}$ is derived from counting the number of combinations of S singly occupied states and M dipoles satisfying the property $2M + S = L$. Therefore,

$$N_M^{(L)} = \binom{M+S}{M} = \binom{L-M}{M}. \tag{4.13}$$

This has to be contrasted with the dimension of the Hilbert space of the original model, $\dim(\mathcal{H}) = \binom{N+L-1}{N}$. Note that due to the hard-core constraints the maximum number of possible dipoles in a system is the floor function applied to half the system size, $\lfloor L/2 \rfloor$.

4.2.3.1 Dynamics in a basis of symmetric states

One of the goals is to identify possibly simple analytical approaches to the dynamics of the tilted Mott insulator. In the preceding section, we have already achieved a substantial simplification by mapping the complicated bosonic system to a relatively simple effective spin model. However, due to the hard-core constraint, the model in Eq. (4.12) is a many-body model with competing interactions, so that obtaining the dynamics is still a challenging task. One must further emphasize that even the effective spin model approximately governs the dynamics of the system in the Mott-insulator regime. This is because the spin dynamics neglects the virtual tunnelling processes that occur for finite, albeit large on-site interactions. In other words, higher order tunneling processes are completely neglected. In this section, we will discuss how the short time dynamics can be obtained analytically by introducing further approximations, and how the validity of this approximation can be enlarged by properly accounting for the hard-core constraint. The simplest approach is to completely neglect the Δ-term in Eq. (4.12). This term essentially excludes the basis states with two adjacent $|\uparrow\rangle$. For an initial state in which all spins point downwards, for times short enough, these basis states will remain unpopulated and neglecting the hard-core constraint should be a good approximation. This treatment should also be a better approximation for larger detunings ($|U - \Omega| \gg J$). In this case, dipoles become more energetically costly to populate and the system

remains in the no dipole or a single dipole manifold in which the hard-core constraint is not relevant. This is a favorable situation: without the Δ-term, we are dealing with a non-interacting system which can be treated exactly. The dynamics in this case is obtained in a basis of Dicke states [105], which are the set of spin states with maximum total spin. In this approximation, the Hamiltonian can be rewritten as $H^S_{\text{eff}} \approx -2J\sqrt{2}\,\hat{S}^x_{\text{total}} + (U-\Omega)\,\hat{S}^z_{\text{total}}$ with collective spin operators $\hat{S}^\alpha_{\text{total}} = \frac{1}{2}\sum_i \sigma^\alpha_i$. The dynamics is then described as a rotation of the Bloch vector of the collective spin state manifold, $S_{\text{total}} = (L-1)/2$. It can be obtained by solving the equations of motion for the total spin components with initial condition $\langle \hat{S}^z_{\text{total}}(0)\rangle = -(L-1)/2$. Defining $\omega_0 \equiv \sqrt{8J^2 + (U-\Omega)^2}$, one then obtains:

$$\begin{aligned}
\langle \hat{S}^z_{\text{total}}(t)\rangle &= -\frac{(L-1)}{2}\frac{(U-\Omega)^2 + 8J^2\cos(\omega_0 t)}{\omega_0^2},\\
\langle \hat{S}^x_{\text{total}}(t)\rangle &= \frac{\sqrt{2}J(L-1)(U-\Omega)(1-\cos\omega_0 t)}{\omega_0^2},\\
\langle \hat{S}^y_{\text{total}}(t)\rangle &= -\frac{\sqrt{2}J(L-1)\sin(\omega_0 t)}{\omega_0}.
\end{aligned} \tag{4.14}$$

Using the mapping discussed later in Eq. (4.24), the CM motion is,

$$x_{\text{cm}}(t) = \frac{1+L^2}{2L} - \frac{1}{L}\langle \hat{S}^z_{\text{total}}(t)\rangle. \tag{4.15}$$

When comparing the result of Eq. (4.15) to the exact results of Figure 4.5, we find good agreement up to times $Jt \approx 0.3$. As discussed above, the larger the detuning from resonance, the better the qualitative agreement.

This approximation hence leads to a closed expression for the CM motion. However, neglecting the Δ-term is a very rough approximation. A more accurate treatment can be obtained by excluding all states with two adjacent $|\uparrow\rangle$. In this way, we account for the hard-core constraint but stay within the collective spin manifold. This basis we refer to as the set of symmetric states (see Appendix B.4). It is desirable to estimate how long the system can remain in this symmetric space due to the fact that the symmetric states are not eigenstates of the Hamiltonian and that we have reduced the the size of the Hilbert space from the full one to a space of dimension $\lfloor L/2 \rfloor$. For a two site system (one spin), the Dicke and symmetric states are trivially the same and the time-

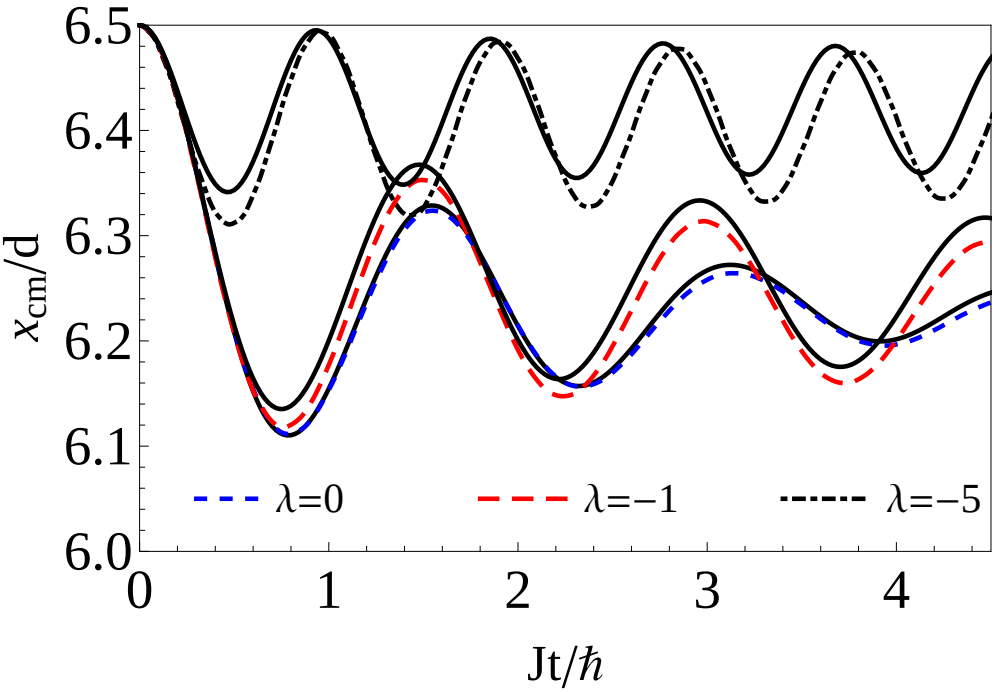

Figure 4.5: Numerical results (Krylov-ED) for the CM motion in a system with $L = 12$ sites for three different values of $\lambda \equiv (U-\Omega)/J$, where $J = 1$ and $\Omega = 40$. The solid lines show the evolution of the effective spin model, while the dashed lines show the exact evolution of the BHM. As the parameters are tuned off resonance, the amplitude decreases, indicating less participation of higher dipole excitations.

evolved state is spanned by either set, since the hard-core constraint does not come into play. For a three site system (two spins), the dynamics obtained in the symmetric states is exact. However, in the general case, the hard-core constraint leads to a time-dependent phase for the different spin configurations, and the system decays out of the subspace of symmetric states. Despite the decay, for times short enough most of the weight of the many-body wavefunction is on the symmetric manifold and one can treat the dynamics on this time scale to a good approximation. This is done numerically. As expected, we find that the result is a better approximation than the treament in the Dicke states, the dynamics being comparable to the exact treament for longer times. Nevertheless, the decay out of the symmetric manifold grows, in lowest order, as $P_{\text{asym}} \sim N_2^{(L)} J^6 t^6$ and therefore the time interval in which this approximation is valid shrinks with increasing system size.

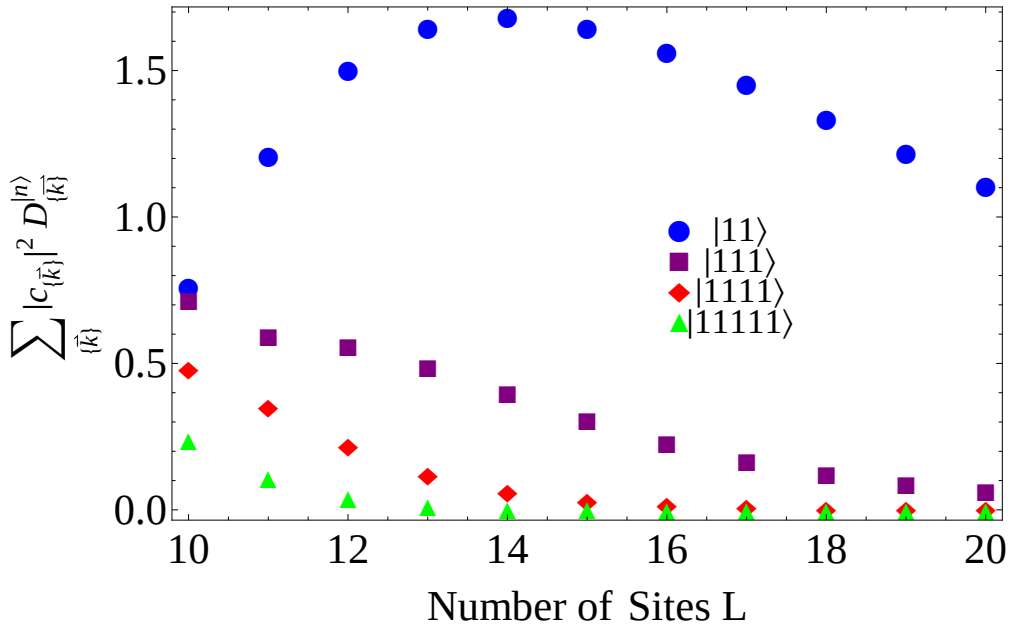

Figure 4.6: Weighted sums of the coefficients of the ground state of the BHM, Eq. (4.1) in the hard-core limit $U \to \infty$ for fixed $N = 8$ as a function of system size L. We consider configurations that possess $n = 2$, 3, 4, and 5 adjacently occupied sites (clusters), and weight the coefficients by the number of occurrences $D^{|n\rangle}_{\{\vec{k}\}}$ of the cluster which are obtained numerically as described in Appendix B.5.

4.3 Center of Mass Oscillations: Incommensurate Filling

We now develop an approximate analytical solution to the dynamics of the system at incommensurate fillings, $N < L$, at which the spin model is not valid. We begin with an illustrative example by considering a lattice of six sites initially prepared in the Fock state $|110111\rangle$. Suppose we time evolve this state at resonance, $U = \Omega$, with U, $\Omega \gg J$. As we discussed before, the particles explore configurations degenerate in energy to the initial state in zeroth order in J. The family of states which needs to be considered during the time evolution is given by the states

$$
\begin{aligned}
|\alpha_1\rangle &\equiv |110111\rangle, \\
|\alpha_2\rangle &\equiv |200111\rangle, \\
|\alpha_3\rangle &\equiv |110201\rangle, \\
|\alpha_4\rangle &\equiv |110120\rangle, \\
|\alpha_5\rangle &\equiv |200201\rangle, \\
|\alpha_6\rangle &\equiv |200120\rangle.
\end{aligned}
\tag{4.16}
$$

The time evolution of the system in the initial state $|\alpha_1\rangle$ is then

$$
\begin{aligned}
&|\psi(t)\rangle = \\
&\cos\left(\sqrt{2}Jt\right)\cos\left(2Jt\right)\,|\alpha_1\rangle + \frac{i\sin\left(\sqrt{2}Jt\right)\cos\left(2Jt\right)}{\sqrt{2}}\,|\alpha_2\rangle \\
&+ \frac{i\cos\left(\sqrt{2}Jt\right)\sin\left(2Jt\right)}{\sqrt{2}}\,|\alpha_3\rangle + \frac{i\cos\left(\sqrt{2}Jt\right)\sin\left(2Jt\right)}{\sqrt{2}}\,|\alpha_4\rangle \\
&- \frac{\sin\left(\sqrt{2}Jt\right)\sin\left(2Jt\right)}{\sqrt{2}}\,|\alpha_5\rangle - \frac{\sin\left(\sqrt{2}Jt\right)\sin\left(2Jt\right)}{\sqrt{2}}\,|\alpha_6\rangle.
\end{aligned}
\tag{4.17}
$$

This results in the CM motion

$$
x_{\mathrm{cm}}(t) = \frac{1}{10}\left[34 + \cos\left(2\sqrt{2}Jt\right) + \cos\left(4Jt\right)\right]. \tag{4.18}
$$

The form of $x_{\mathrm{cm}}(t)$ indicates that the dynamics is governed by the two subspaces spanned by the resonant families of the $|11\rangle$ and $|111\rangle$ states. Projected onto those subspaces the effective Hamiltonian becomes

$$
\begin{aligned}
\hat{H}' = \hat{P}_D\hat{H}_{eff}\hat{P}_D &= -\sqrt{2}J\left(\hat{d}_1 + \hat{d}_4 + \hat{d}_5 + h.c.\right) \\
&\equiv \hat{H}_1 + \hat{H}_{4,5},
\end{aligned}
\tag{4.19}
$$

where the operator $\hat{P}_D$ projects onto the resonant families. Due to the fact that $[\hat{H}_1, \hat{H}_{4,5}] = 0$, the time evolution takes place in independently evolving subspaces,

$$
\begin{aligned}
|\alpha_1(t)\rangle &= e^{-i\hat{H}'t}|\alpha_1\rangle \\
&= e^{-i\hat{H}_1 t}e^{-i\hat{H}_{4,5}t}|11\rangle\otimes|0\rangle\otimes|111\rangle \\
&= e^{-i\hat{H}_1 t}|11\rangle\otimes|0\rangle\otimes e^{-i\hat{H}_{4,5}t}|111\rangle,
\end{aligned}
\tag{4.20}
$$

and the total CM dynamics reduces to the direct sum of the CM evolution in each of the clusters:

$$\begin{aligned} x_{\mathrm{cm}}(t) &= \frac{1}{N}\sum_j j\langle\alpha_1(t)|n_j|\alpha_1(t)\rangle \\ &= \frac{1}{N}\langle 11|e^{i\hat{H}_1 t}(n_1+2n_2)e^{-i\hat{H}_1 t}|11\rangle \\ &+ \frac{1}{N}\langle 111|e^{i\hat{H}_{4,5}t}(4n_4+5n_5+6n_6)e^{-i\hat{H}_{4,5}t}|111\rangle \\ &= \frac{1}{10}\left[5+\cos\left(2\sqrt{2}Jt\right)+29+\cos\left(4Jt\right)\right]. \end{aligned} \tag{4.21}$$

We have thus demonstrated that the resonant dynamics of a larger system can be treated by considering the time evolution of smaller decoupled systems. In order to use this approach for a system of arbitrary size, we have to consider configurations of particles which are sparse and spread out over the lattice. For simplicity we will assume the atoms are prepared in the ground state in the absence of a tilt, *i.e.* $\Omega = 0$, we assume open boundary conditions and that at time $t = 0$ the system is suddenly tilted close to resonance, $U \sim \Omega \gg J$.

To be more quantitative, we rewrite the initial wave function in a more tractable, albeit approximate way:

$$|\psi_0\rangle \sim \sum_{\{\vec{k}\}} c_{\{\vec{k}\}} \prod_{\substack{\{k_i\},\{k_j\} \\ \{k_m\},\{k_l\}}} a^\dagger_{k_l}\hat{\alpha}^\dagger_{k_i}\hat{\beta}^\dagger_{k_j}\hat{\gamma}^\dagger_{k_m}|0\rangle, \tag{4.22}$$

where the summation extends over all permutations of the positions $\{k_i\}$,$\{k_j\}$, $\{k_m\}$, and $\{k_l\}$; the coefficients $c_{\vec{k}}$ are derived in Appendix B.5. $|0\rangle$ is the vacuum state and the operators $a^\dagger_{k_l}$, $\hat{\alpha}^\dagger_{k_i}$, $\hat{\beta}^\dagger_{k_j}$, and $\hat{\gamma}^\dagger_{k_m}$ create configurations $|1\rangle$, $|11\rangle$, $|111\rangle$, and $|1111\rangle$, respectively, with a given weight determined by the coefficient $c_{\{\vec{k}\}}$. We use the convention that the components of $\vec{k}$ denote the particle positions and the subscripts attached to the creation operators denote the location of the leftmost site of the cluster. We account for subspaces up to only $|1111\rangle$ because the configurations containing larger clusters can be presumed to carry negligible weight (sparse filling condition, see Figure 4.6). This can be understood in the hard-core regime where the atoms in the initial many-body ground state want to spread out symmetrically with respect to the center of the lattice in order to maximize their kinetic energy, thus avoiding the energetically forbidden double occupancy. Hence, at low filling factors, the configurations that most significantly contribute to the ground state

are those clusters with the lowest number of contiguous occupied sites (see Figure 4.6). During the course of the time evolution, each cluster evolves independently within its resonant manifold, allowing us to treat the time evolution of the full system by computing the time evolution of each of the small clusters and their associated resonant families. In addition, the configurations $|1\rangle$ do not contribute to the dynamics since the resonance condition is significant only if at least two adjacent sites are occupied.

We denote the number of n-particle clusters of a basis state which has particles at positions $\vec{k}$ by $D_{\vec{k}}^{|n\rangle}$. Then we obtain for the CM motion in this approximation

$$\begin{aligned} 2Nx(t) \sim \sum_{\{\vec{k}\}} |c_{\{\vec{k}\}}|^2 \Big\{ & D_{\{\vec{k}\}}^{|11\rangle} \cos\left(2\sqrt{2}Jt\right) \\ & + D_{\{\vec{k}\}}^{|111\rangle} \cos\left(4Jt\right) \\ & + \frac{D_{\{\vec{k}\}}^{|1111\rangle}}{34} \Big[\left(1-\sqrt{17}\right) \cos\left(2\sqrt{5-4\sqrt{17}}Jt\right) \\ & + \left(1+\sqrt{17}\right) \cos\left(2\sqrt{5+4\sqrt{17}}Jt\right) \\ & + 64 \cos\left(\sqrt{5+4\sqrt{17}}Jt\right) \cos\left(\sqrt{5-4\sqrt{17}}Jt\right) \Big] \Big\}, \end{aligned} \tag{4.23}$$

where we denote by $\{\vec{k}\}$ all permutations of the positions of N particles. At low enough fillings, it represents a good approximation to the time evolution of systems of arbitrary size and number of particles and predicts the dynamics of tilted Mott insulators at resonance away from the commensurable case. In the next section, we will test the accuracy of this approach.

4.4 Comparison of numerical results to the effective spin model and the analytical treatment

In this section, we compare the time evolution obtained via the effective spin model Equation (4.12) to the exact one governed by the BHM Equation (4.1). In addition, we analyze the dynamics of the effective spin model Equation (4.12) as a function of λ and find that the amplitudes of the BOs possess a maximum at λ_c.

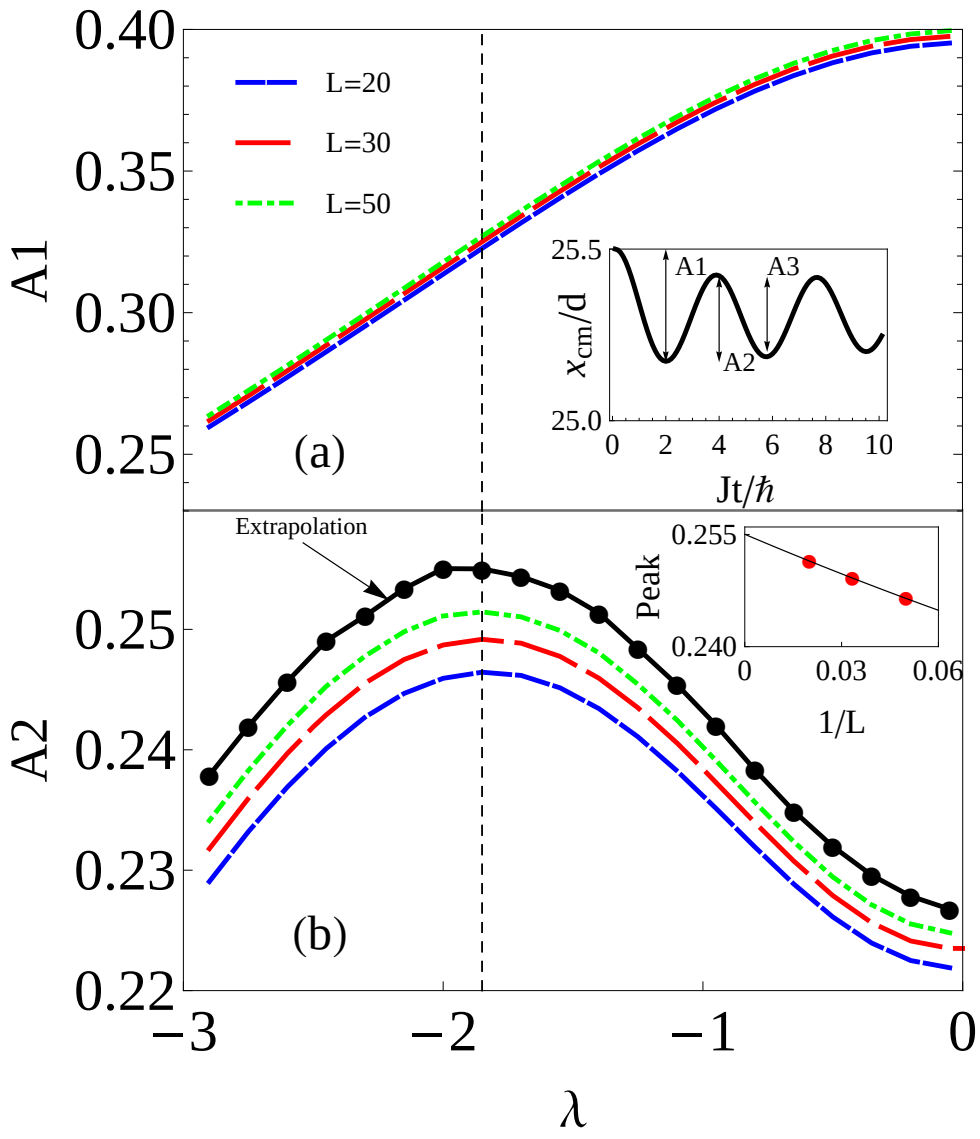

Figure 4.7: Amplitudes of the CM motion as obtained in the effective spin model and as defined in the inset in (a), which shows the evolution at resonance. The results shown are for systems with $L = 20$, 30 and 50 lattice sites and are obtained using the adaptive t-DMRG. The amplitudes are obtained from interpolating the discrete data points of the CM motion. (a) Difference $A1$ (measured in units of lattice spacings) between the initial CM position and the first minimum as a function of λ. (b) The second amplitude $A2$ (measured in units of lattice spacings) as a function of λ. The inset shows the finite size extrapolation at $\lambda = -1.85$, and the black circles show $A2(\lambda)$ after finite size extrapolation. We estimate the error of the extrapolation to be of the order of the symbol size.

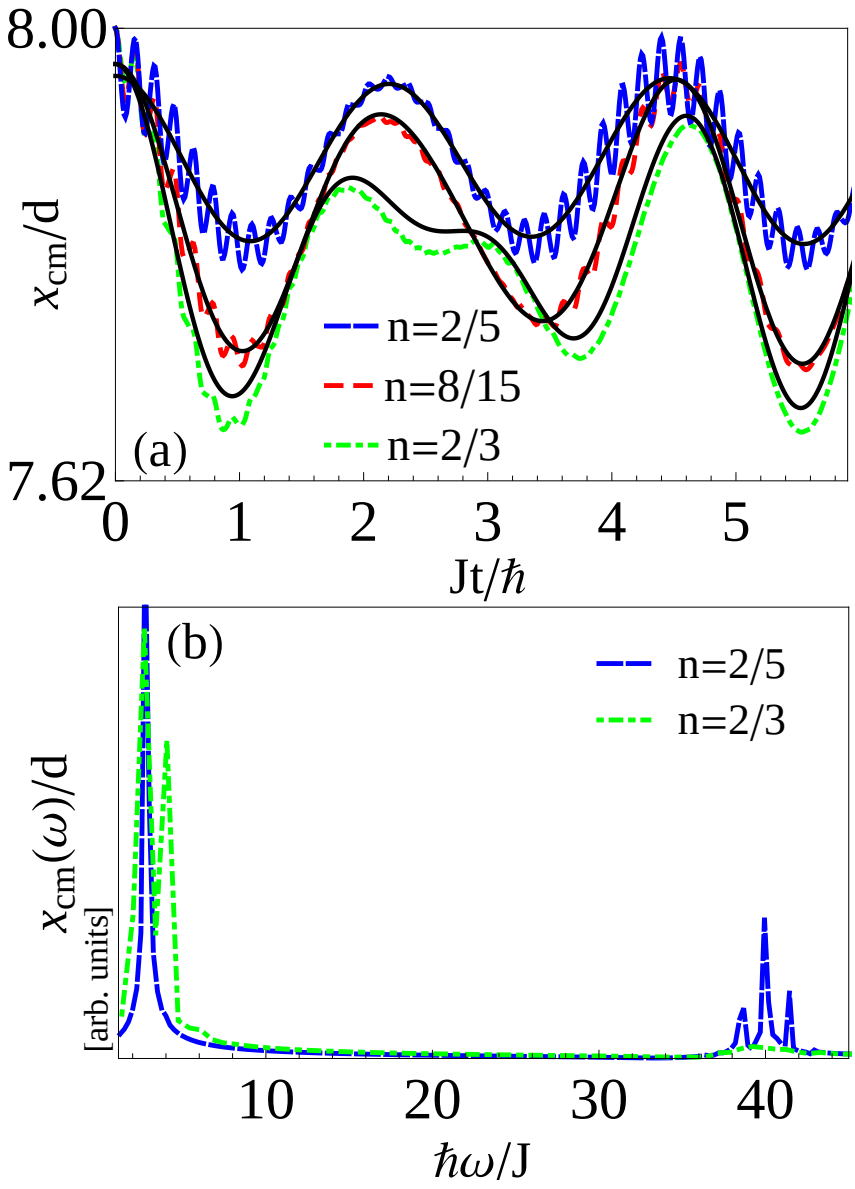

Figure 4.8: (a) CM motion for a system of $L = 15$ lattice sites at resonance at low fillings away from commensurability. The solid curves show the result of the analytic calculation, Eq. (4.23). Note that the analytic expression neglects the fast BO which are caused by population of non resonant states. (b) Spectral analysis of the CM motion. At low fillings, 2 particle cluster states dominate the dynamics. The high frequency BO are visible as peaks at $\Omega/J = 40$ which decrease upon increasing the filling. The additional low frequency peaks are due to larger cluster states which become relevant at higher fillings. The results for the BHM at $n = 2/5$ and $n = 8/15$ are obtained via Krylov-ED, the ones at $n = 2/3$ are adaptive t-DMRG results.

4.4.1 Accuracy of the effective spin dynamics at commensurate filling

In order to compare the dynamics of the effective spin model to the one of the BHM at commensurate filling, we use the mapping

$$\begin{aligned} \text{left boundary site:} \quad & n_1 \to (\hat{\sigma}_1^z + 3)/2, \\ \text{right boundary site:} \quad & n_{L'} \to (1 - \hat{\sigma}_L^z)/2, \\ \text{bulk:} \quad & n_i \to (\hat{\sigma}_i^z - \hat{\sigma}_{i-1}^z + 2)/2, \end{aligned} \tag{4.24}$$

where L is the size of the spin system and $L' = L + 1$ the size of the bosonic system, which has one lattice site more than the spin system, due to the fact that the dipoles are located on the bonds. This mapping is obtained by comparing individual site occupations in the presence or absence of a dipole; the different mapping at the boundary sites and in the bulk is due to the open boundary conditions. The difference between the mapping at the left and the right boundaries is due to the fact that the site at the highest potential (right boundary) will possess either zero or one particle, but the site at the lowest potential (left boundary) has either one or two particles.

The dynamics of the BHM is obtained by evolving an initial Mott insulating ground state with one particle per site. In the spin picture, this is equivalent to an initial state with all spins pointing downwards. In Figure 4.5 we show the time evolution of the BHM and the one of the effective spin model at $\lambda = 0$, $\lambda = -1$, and $\lambda = -5$. We find that the effective spin model reproduces the dynamics of the BHM even when detuning not too far off resonance. The evolution of the systems is essentially identical on short time scales ($Jt \lesssim 2.5$ for $\lambda = 0$, $Jt \lesssim 0.5$ for $\lambda = -1$, and $Jt \lesssim 0.3$ for $\lambda = -5$) but then differs increasingly in the course of the time evolution. In addition, for small detunings from resonance, the frequency of the oscillation is in excellent agreement to the exact solution, while it differs in the case of stronger detunings. Note that the detuning causes the system to be rigid in the sense that states that contain more dipoles are more costly in energy. This point was discussed previously. Hence, on sufficiently short times, the number of dipole states contributing to the dynamics is reduced so that the time evolution can be obtained by considering a smaller number of states (see Reference [106] for a detailed discussion).

4.4.2 Maximum of the CM amplitude at λ_c

Now we turn to the properties of the CM oscillations in the time evolution of the effective spin system given in Equation (4.12) upon changing λ. As before, we consider the time evolution of an initial state in which all spins are pointing downwards, which is equivalent to a Mott-insulator with one particle per site in the bosonic language. As shown in Reference [83], the effective spin model possesses a quantum critical point at $\lambda_c \approx -1.85$. We are interested in possible signatures of this critical point in the CM motion. In Figure 4.7 we present our adaptive t-DMRG results for the first oscillations $A1$, $A2$ and $A3$ [defined in the inset of Figure 4.7(a)] as a function of detuning λ for systems with $L = 20$, 30 and 50 sites. Interestingly, we find a local maximum of $A2$ at $\lambda \approx -1.85$, indicating that this quantity might indeed reveal the existence of a critical point in the time evolution of this system. This feature seems to persist upon changing the system size, and at λ_c we obtain after finite size extrapolation the value $A2(\lambda_c, L \to \infty) \approx 0.255$. This can be contrasted to the value of $A2(-0.05, L \to \infty) \approx 0.227$, so that the amplitude when increasing the detuning from resonance at $\lambda = 0$ to λ_c changes by $\approx 10\%$. Similarly, we find a maximum of $A3$ at $\lambda \approx -1.85$. However, such a maximum in the vicinity of λ_c does not show up in $A1(\lambda)$, a quantity which instead reaches its peak value at resonance $\lambda = 0$.

This puts forth the interesting possibility that one may be able to use the CM oscillations to identify quantum critical points of a generic phase transition.

4.4.3 Accuracy of the effective cluster dynamics at incommensurate fillings

In Figure 4.8 we compare the CM motion as obtained by the original BHM for a system of $L = 15$ sites at various fillings $n \leq 2/3$ to the one obtained in the approximate treatment using families of small cluster states. At fillings $n = 2/5$ and $n = 8/15$ the plot shows data obtained via the Krylov-ED approach, so that the results are essentially exact. At $n = 2/3$, we present data obtained via adaptive t-DMRG where the discarded weight is $> 10^{-9}$ for times $Jt > 2$, so that the results at later times might be affected by numerical errors larger than the width of the lines

shown in the graph. The overall behavior of the approximate solution given by Equation (4.23) is in good agreement with the numerical results in all cases shown. However, at low fillings, fast oscillations with frequency equal to Ω [Figure 4.8(b)] are superimposed onto the resonant frequency oscillations. These high frequencies are due to the single-particle BO and are not taken into account by our projection onto resonant families of states. However, these BO can be suppressed by increasing the filling [as seen in Figure 4.8(b)] or by using larger values of Ω while ensuring the resonant condition. This is explained by the fact that the amplitude of the BO is $\propto 1/\Omega$. At larger fillings, the approximation Equation (4.23) breaks down since clusters larger than the $|1111\rangle$ states become relevant.

With this, we conclude our treatment of the dynamics after a sudden tilt of an initial Mott-insulating state and turn now to the question of how to enhance transport in these systems.

4.5 Engineering Transport: A Slinky Scheme

In this section, we apply the projection onto resonant families of small cluster states to the problem of enhancing transport of atoms on optical lattices. In particular, we treat systems which are prepared so that only decoupled $|11\rangle$ clusters are present in the initial state. This can be realized using a pattern loading scheme in which an optical superlattice is generated by superimposing two lattices with different periodicity. Such a spatially selective loading of particles onto an optical lattice has been experimentally achieved, as discussed in Ref. [107]. Two independent lattices are formed by two pairs of lasers all of the same wavelength λ_L intersecting at angles, θ_1 and θ_2, shown in Figure 4.9. Each lattice maintains a nearest-neighbor distance $d_i = \lambda_L/\left(2\sin(\theta_i/2)\right)$. As an example, the angles can be tuned so that the lattice spacing d_2 is a multiple of d_1. When this occurs, "super" periodic structures are formed.

The transport through the system now is achieved by applying time-dependent fields. Driven tunneling by using time-depedent fields has been addressed at the single-particle level before [108, 109, 101, 110]. For instance, such an effect has been realized in Ref. [110], where shaking the

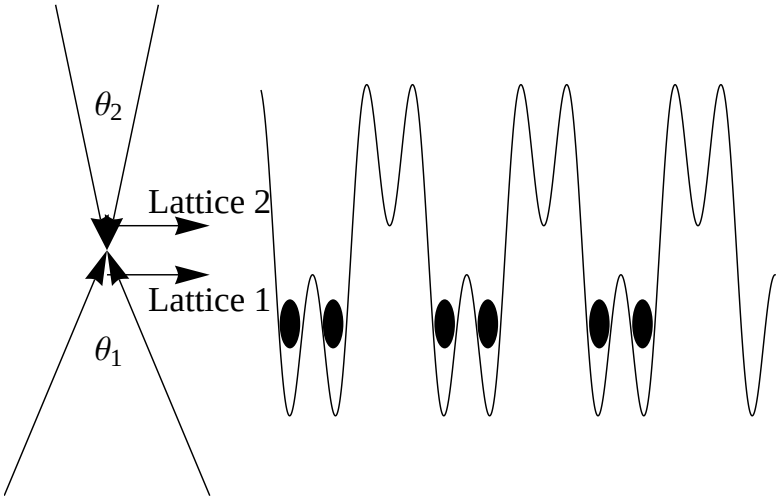

Figure 4.9: Two pairs of lasers intersect at different angles producing parallel lattices. After preparation, particles are loaded super periodically.

lattice, *i.e.*, by applying a time-dependent linear field $\Omega(t) = \Omega_0(1 + \gamma \sin(\omega t))$ and tuning the frequency close to that of the BO leads to an enhancement of the CM motion, called "super" Bloch oscillations. Similar to the approach of Ref. [19], we stroboscopically apply two oscillatory driving fields in order to enhance the amplitude of the oscillations. At the many-body level, we propose to enhance transport of the atoms by performing an amplitude modulation along the lattice direction, $V_x(t) = V_{0x}(1 + v \sin(\omega t))$ where $v \ll 1$ and V_x the amplitude of the lattice potential. The effect of the modulation can be addressed by assuming that the Wannier functions possess a Gaussian profile on each lattice site. Using the Gaussian approximation [6], the parameters of the BHM are modified and one obtains [111]

$$\begin{aligned} J &= J_0\, e^{-v \sin(\omega t)}, \\ U &= U_0\, \left[1 + v \sin\left(\omega t\right)\right]^{1/4}, \\ \Omega &= \Omega_0\, \left[1 + v \sin\left(\omega t\right)\right]. \end{aligned} \tag{4.25}$$

The linear approximation of the Hamiltonian around $v = 0$ results in $J(t) \approx J_0 + \tilde{J} \sin\left(\omega t\right)$, where $\tilde{J} = V_{0x} J_0 v (\frac{d \ln U}{d V_x}|_{v=0} - \frac{d \ln J}{d V_x}|_{v=0})$.

In the following, we apply the pattern loading scheme to realize an initial state at time t_0 as

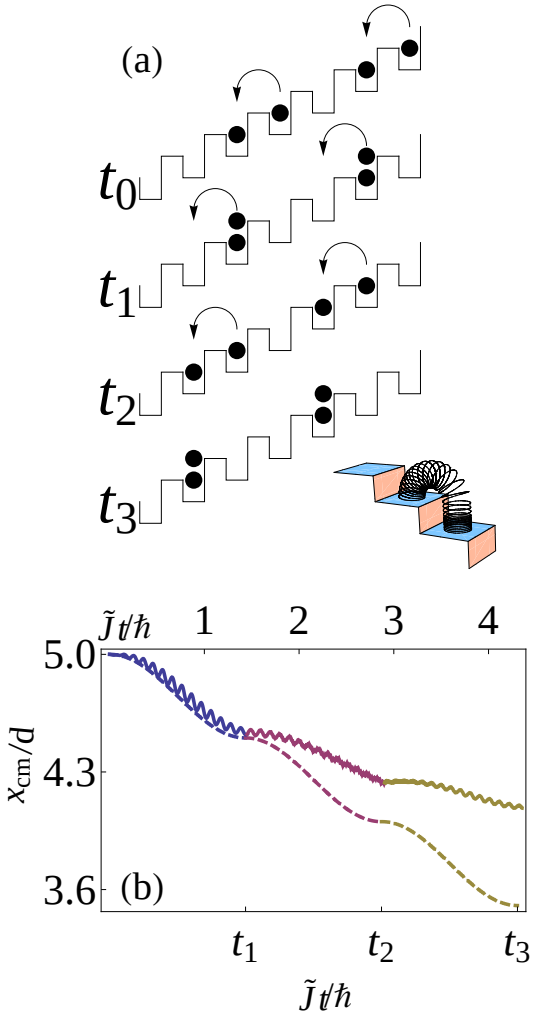

Figure 4.10: (a) Initial state at t_0 obtained by a pattern loading scheme and 'slinky motion' obtained by a stroboscopic modulation of the lattice depth with the two resonant frequencies, $\omega = U_0 \pm \Omega_0$. The time sequence at which ω is alternated is: $t_0 = 0$, $\tilde{J}t_1 = \frac{\pi}{\sqrt{2}}$, $t_2 = 2t_1$, and $t_3 = 3t_1$. One can compare the motion of the particles to that of a toy slinky tumbling down a set of stairs as depicted above. (b) CM motion due to the stroboscopic modulation of the lattice depth. The different colors indicate the intervals in which $\omega = U_0 \pm \Omega_0$, respectively. The dashed curve displays the dynamics obtained by fully diagonalizing a BHM, Eq. (4.1), with $L = 7$ and $N = 4$ in the approximation $U(t) = U_0$, $\Omega(t) = \Omega_0$, and $J(t) \approx \tilde{J}\sin(\omega t)$, captured by Eq. (4.28). The solid line displays results for the same system but in which $J(t)$, $U(t)$, and $\Omega(t)$ are obtained from Wannier orbitals for $V_{0,x} = 0.5$ and $v = 0.3$. The time sequence in this case is $\tilde{J}t_1 \approx 1.43$, $t_2 = 2t_1$, and $t_3 = 3t_1$, where $\tilde{J}t_1$ is identified numerically as the time at which the first minimum in $x_{\rm cm}(t)$ appears. The numbers on the top axis refer to the exact dynamics (solid lines).

shown in Figure 4.10(a). In this state, we position two adjacent particles on every three lattice sites. For $\Omega_0 \gg J$, BO are suppressed so that only resonant motion within the $|11\rangle$ cluster is possible. Hence, we can treat the dynamics to a good approximation by projecting onto $|11\rangle$ clusters. In addition, we require $U_0 \gg J$ and $|U_0 - \Omega_0| \gg J$. Then the two energies $U_0 - \Omega_0$ and $U_0 + \Omega_0$ are well separated from each other. Only by adjusting the frequency of the modulation to either $U_0 - \Omega_0$ or $U_0 + \Omega_0$, resonance of the $|11\rangle$ state with a particle hole excitation can be achieved; in this way, the $|11\rangle$ clusters can be resonant with either the $|20\rangle$ or the $|02\rangle$ configurations. Hence, it is possible to control the direction of the motion of the atoms by tuning the frequency accordingly, and the time evolution of the two particles in a cluster is either $|\psi(t)\rangle = c_g(t)|11\rangle + c_e(t)|20\rangle$ or $|\psi(t)\rangle = c_g(t)|11\rangle + c_e(t)|02\rangle$, respectively. Note that for a doubly occupied site, the effect is reversed, and applying the same driving frequency will lead to a motion in the direction opposite to the motion induced on a pair of neighboring particles. In the following, we explore this to formulate our proposal for a transport scheme.

In order to provide a more quantitative description of this behavior we first set $J(t) \approx \tilde{J}\sin(\omega t)$. Since we have only $|11\rangle$ clusters we can restrict the dynamics to a two-level system described by the effective spin model of Eq. (4.12) which in this case is

$$H_{\text{eff}} = -\sqrt{2}\tilde{J}\sin(\omega t)\,\sigma_x + \frac{\Delta\omega}{2}\sigma_z, \tag{4.26}$$

where $\Delta\omega = U_0 \pm \Omega_0$. In the rotating wave approximation the Hamiltonian is

$$H_{\text{eff}} = \frac{\delta}{2}\sigma_z + \frac{\sqrt{2}}{2}J\sigma_y, \tag{4.27}$$

where we have set $\delta = \Delta\omega - \omega$, and we assume $\delta \ll \Delta\omega$. In this two-state representation, the center of mass observable is $\hat{x}_{cm} \sim \frac{\sigma_z}{4}$. Assuming an initial state in which $c_g(0) = 1$, we obtain

$$x_{cm}(t) \sim \pm\frac{\tilde{J}^2\cos\left(t\sqrt{2\tilde{J}^2+\delta^2}\right)}{4\tilde{J}^2+2\delta^2}, \tag{4.28}$$

with the $\pm$ indicating motion up or down. Even though the CM amplitude is $2\tilde{J}^2/(4\tilde{J}^2+2\delta^2) \leq 1/2$, it is nevertheless possible to implement transport through the lattice by stroboscopically alternating

the modulation frequencies $\omega = U_0 \pm \Omega_0$ in intervals of $\Delta t = \pi/\sqrt{2}\tilde{J}$ at zero detuning: in this way, we transform the initial $|11\rangle$ cluster to a double occupancy, and due to the alternation of the frequency, this is further transformed into a $|11\rangle$ cluster *shifted* by one lattice spacing relative to the original cluster.

Alternating ω hence leads to a slinky like motion as depicted in Figure 4.10(a), inducing a net transport of particles through the system. Note that the net transport can also be uphill. In Figure 4.10(b) we show as a proof of principle results for such a slinky motion. We display the exact numerical time evolution for a Bose-Hubbard system of $L = 7$ sites and $N = 4$ particles when stroboscopically modulating ω and compare it to the result of an approximation in which U and Ω are constant in time and $J(t) \approx \tilde{J}\sin(\omega t)$. This approximation leads to a CM motion captured by Eq. (4.28). As can be seen, in both cases the CM motion on the time scale treated is strongly enhanced. At the end of the time evolution shown, the approximation shows transport by $\Delta x_{\mathrm{cm}} \approx 1.5$ lattice spacings, while the exact solution shows $\Delta x_{\mathrm{cm}} \approx 0.9$ lattice spacings - note that the usual CM motion is restricted to $\Delta x_{\mathrm{cm}} \leq 0.5$ lattice spacings. Despite the difference between the exact result and the approximate treatment, Figure 4.10 shows that the description in terms of the slinky motion compares qualitatively. We therefore expect that for larger systems transport through the lattice should be realizable. In addition, we expect that for our simple example, the transport can further be enhanced by optimizing the parameters.

As mentioned in Sec. 4.4.3, we have neglected the high-frequency BO which will lead to a dephasing of the slinky motion of the atoms. This, however, can be controlled by choosing Ω sufficiently large to dampen the BO as discussed in Sec. 4.4.3. Nevertheless, the tilt must be weak enough so that the description of the system by a one-band model remains valid.

4.6 Summary

In this chapter, we investigated resonant dynamics of strongly-interacting bosonic particles on a one-dimensional tilted optical lattice. At commensurate fillings when tuning to resonance $U = \Omega$, we found that CM oscillations enhanced compared to the standard BO exhibited by non-interacting

atoms. Following Ref. [83], the resonant dynamics can be captured by an effective spin-1/2 model. Interestingly, we detected signals of the critical point in the dynamics of the CM oscillations in the spin model which calls for further studies. We developed a method to describe the dynamics at low fillings based on projections onto small clusters. We find that this approach provides a good description of the dynamics up to fillings $n \approx 2/3$. Using this approximation, we developed a scheme to engineer transport in the lattice by stroboscopically applying amplitude modulated frequencies of the lattice and we envisage that this scheme can be realized in ongoing experiments on this system [84].

Chapter 5

Quantum Dynamics of Solitons in Strongly Interacting Systems on Optical Lattices

This chapter is based on C. Rubbo *et. al.*, Phys. Rev. A 85, 053617 (2012).

In the previous chapter, we focused on the transport of particles in strongly interacting systems. In this chapter, we focus on another aspect of transport: solitons in strongly interacting systems. Solitary waves (disturbances that propagate without changing shape) and solitons (solitary waves whose shape and speed remain unchanged even after collisions) are encountered in systems as diverse as classical water waves [112], magnetic materials [112, 113, 114, 115, 116, 117, 118, 119, 120, 121, 122, 123, 124, 125, 126, 127, 128], fiber-optic communication [112, 129, 130], and BECs [131, 112, 132, 133]. Rooted in the nonlinearity of the system which balances dispersive effects, solitons are fascinating non-linear waves that encode collective behavior in the system. In this chapter, we investigate solitons in strongly interacting systems in optical lattices. Solitons in a HCB system described in terms of hard core on-site repulsion and attractive nearest neighbor interaction have been studied using mean field equations obtained from mapping the HCB system to an anisotropic $S = 1/2$ Heisenberg spin system [134, 135]. The continuum limit of the lattice populated with HCB is described by a generalized Gross-Pitaevskii equation (GPE), which we will refer to as "HGPE" [See Equation (5.10)] as it describes hard core bosons in a mean field treatment. HGPE solitary waves are obtained as an analytic solution which was shown to provide an almost exact solution of the equations of motion [134]. These two species of solitons can be referred to as the GP-type and the non-GP-type as the former corresponds to a dark condensate fraction that

dies beyond sound velocity while the latter is associated with brightening of the condensate and persists all the way up to sound velocity and transforms into a soliton train for supersonic velocities.

An important question that we investigate here is whether these mean field solitons survive quantum fluctuations. In order to go beyond the mean-field treatment, the density matrix renormalization group methods discussed in Chapter 3 are used to study the effects of quantum fluctuations on these solitons. In previous work, the quantum dynamics of GPE dark solitons in the superfluid regime of the Bose-Hubbard Hamiltonian has been studied via TEBD methods by Mishmash *et al.* [136, 137]. The main findings are that for weak interactions the dark soliton is stable on a time-scale of the order of $\sim 20 - 40$ units of the hopping and is followed by decay due to two-particle scattering processes. The larger the on-site interaction, the stronger the scattering and the faster the decay of the solitons. In addition, these studies treated collisions between the solitary waves which confirm the soliton nature of the states on the time scales treated. These studies focused on the limit of small interactions. Here, we treat the strong coupling case and study the fate of the soliton solutions obtained in the HGPE framework. We do this by generalizing the Bose-Hubbard model of References [136, 137] to include on-site and nearest neighbor density-density interactions. As discussed in Ref. [134], in the continuum limit this gives rise to the two distinct types of solitons mentioned above, which, as we shall see, are found to be stable in both the mean field approximation to the lattice dynamics of the system, as well as in the full quantum dynamics on the lattice.

More specifically, we describe the exact quantum evolution of an initial mean field soliton solution on 1D lattice systems. The soliton and the Hamiltonian driving the dynamics are thereby formulated in terms of a $S = 1/2$ spin language. It is then possible to realize the described soliton solutions in both experiments with ultracold bosonic and spin polarized fermionic atoms, as well as in experiments with polar molecules [138, 139, 140, 141] on optical lattices which can be used to emulate spin-1/2 systems [12, 142]. We combine an analytic solution of the HGPE which provides a continuum approximation to the lattice problem, a numerical treatment of the mean-field equations on the lattice, and a full quantum treatment of the dynamics by applying the

time-dependent DMRG [13, 53, 14, 68, 143]. Both, mean-field and numerical results indicate that for a certain range of parameters the solutions found are indeed stable solitons on the time scale treated.

The chapter is organized as follows: The first section contains a heuristic review of soliton formation in a standard weakly interacting BEC. In Section 5.2, we introduce the effective spin model and its derivation from HCB and spinless fermions on a lattice, the dynamical equation (HGPE) that describes the continuum approximation to the mean-field equations of the lattice system, and we summarize the analytic solution of the HGPE. In Section 5.3 we describe the mean-field ansatz and the approach to the dynamics. In Section 5.4, we analyze the stability of the soliton solutions by comparing the mean-field results on a lattice to the DMRG results. As a measure for the quality of the soliton solution, we use the von Neumann or entanglement entropy as well as correlation functions which also should remain zero in the course of the time evolution if the mean field state were to survive quantum fluctuations. The non-GP-type soliton is found to be somewhat less tolerant of quantum effects compared to the GP-type. In Section 5.5 we propose possible experimental realizations of the HGPE solitons.

5.1 Solitons in a weakly-interacting BEC

We derive the qualitative features of a soliton in a BEC as discussed in Reference [40]. A uniform gas of weakly and repulsively interacting bosons is described by the Hamiltonian in Equation (2.39). We recall the Bogoliubov energy spectrum E_k of a BEC obtained in Equation (2.41),

$$E_k = \sqrt{(E_k^{(0)})^2 + 2U\rho_s E_k^{(0)}},$$

where ρ_s is the condensate density. From the form of the Bogoliubov spectrum, we can see how the interplay of nonlinearity (due to interactions) and dispersion (due to the quasi-momentum) give rise to the existence of solitons. Consider a localized disturbance with amplitude $\delta\rho_s$ and length L in the bulk condensate . Recall also that the velocity of the quasi-particle excitation of the BEC is determined from $v = \frac{1}{\hbar}\frac{dE_k}{dk}$. Then due to the nonlinearity caused by the interactions, the difference

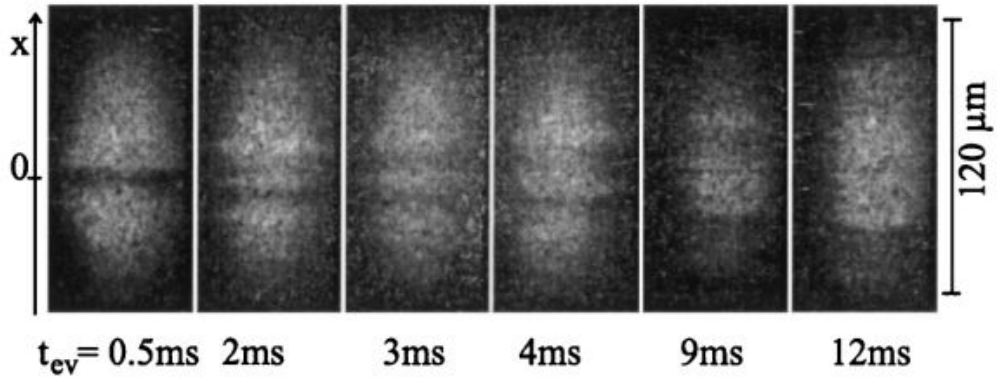

Figure 5.1: Absorption images of BEC's in a trap. A soliton is produced by imprinting a phase. The soliton then propagates along the x direction [Taken from S. Burger *et. al.*, Phys. Rev. Lett. **83**, 5198 (1999)].

between the sound velocity within the disturbance and the sound velocity of the bulk is

$$v(\rho_s + \delta\rho_s) - v_s \approx v_s \delta\rho_s/\rho_s, \tag{5.1}$$

where $v_s = \sqrt{\rho_s U/m}$ is the sound velocity of the bulk system and is derived by considering the behavior of the Bogoliubov spectrum for small k. Since $k \sim 1/L$, the correction to the sound velocity due to the disturbance is a velocity increase given by,

$$v(L) - v_s \approx v_s \xi^2/L^2, \tag{5.2}$$

where $\xi = \sqrt{\hbar^2/(2m\rho_s U)}$ is called the coherence length of the condensate. In order for the local disturbance to preserve its structure, the effects of nonlinearity and dispersion must cancel each other out,

$$\delta\rho_s/\rho_s \sim -\xi^2/L^2. \tag{5.3}$$

This relates the amplitude of the soliton to its length and also constrains the amplitude to be negative. Therefore, solitons in a BEC are typically described by density depressions (dark) in the bulk condensate. Furthermore, Equation (5.2) reveals that the velocity of the soliton is related to its width and density ratio $\delta\rho_s/\rho_s$.

The soliton is also characterized by a sharp phase gradient across the center of the soliton. A conceptual argument that explains the phase gradient is that a non-zero velocity of the local

perturbation indicates a non-zero superfluid velocity, $v = \frac{\hbar}{m}\nabla\phi$. However, this argument is flawed since the phase gradient across the soliton persists even at zero velocity. In the laboratory (see Figure 5.1), solitons have been created in condensates by imprinting a phase gradient [144]. A phase gradient can be created in the center of the condensate by illuminating half the condensate with a pulse of laser light [40]. The phase imprint causes the condensate in the near vicinity of the phase gradient to move, thereby producing a depression in the condensate density.

5.2 Hamiltonian and Equations of Motion

Throughout the rest of this chapter, we treat the dynamics of initial soliton states driven by the spin Hamiltonian

$$H_S = -\sum_j \left[J\ \hat{\mathbf{S}}_j \cdot \hat{\mathbf{S}}_{j+1} - g\ \hat{S}^z_j \hat{S}^z_{j+1} \right] - g \sum_j\ \hat{S}^z_j, \tag{5.4}$$

on a one-dimensional lattice, *i.e.*, we are treating the dynamics of a XXZ-chain with a global external magnetic field of magnitude g. One way to obtain this effective Hamiltonian is as the limiting case of the extended Bose Hubbard model,

$$\begin{aligned} H = &-\sum_j \left[\frac{J}{2}\ \left[\hat{a}^\dagger_j \hat{a}_{j+1} + h.c. \right] + V \hat{n}_j \hat{n}_{j+1} \right] \\ &+ \sum_j \left[\frac{U}{2} \hat{n}_j \left(\hat{n}_j - 1 \right) - (\mu - J)\, \hat{n}_j \right]. \end{aligned} \tag{5.5}$$

Here, $\hat{a}^{(\dagger)}_j$ are the annihilation (creation) operators for a boson at the lattice site j, $\hat{n}_j$ is the number operator, $J/2$ is the nearest neighbor tunneling strength, and μ is the chemical potential. An attractive nearest-neighbor interaction $V < 0$ is introduced to soften the effect of a strong on-site interaction $|U| \gg 0$. As described in Chapter 2, the HCB limit ($|U| \to \infty$) corresponds to the constraint that two bosons cannot occupy the same site. This HCB system can then be mapped to the model Equation (5.4), where the two spin states correspond to two allowed boson number states $|0\rangle$ and $|1\rangle$, and setting $g = J - V$. This is interesting since the existence of the proposed soliton solutions for this spin model has implications for further systems than the ultracold bosonic atoms usually considered when describing soliton phenomena in cold gases. In particular it should

be noted that the XXZ model in 1D can be obtained using the Jordan-Wigner transform from a system of spinless fermions

$$H_{\mathrm{SF}} = -\frac{J}{2}\sum_j \left[\hat{c}^\dagger_{j+1}\hat{c}_j + h.c.\right] + V\sum_j \hat{n}_j\hat{n}_{j+1} + \tilde{\mu}\sum_j \hat{n}_j, \tag{5.6}$$

with $\hat{c}_j^{(\dagger)}$ the fermionic annihilation (creation) operators on site j, and $\hat{n}_j = \hat{c}^\dagger_j\hat{c}_j$ the density on site j. Therefore, it should be possible to investigate the soliton dynamics in experiments with bosonic atoms, in spin systems, and in fermionic systems. In Section 5.5 we discuss possible implementations in experiments with cold gases.

For simplicity, we set up our discussion in the framework of bosonic systems, without losing generality. Then, the spin flip operators $\hat{S}^\pm = \hat{S}_x \pm i\hat{S}_y$ correspond to the annihilation and creation operators of the corresponding bosonic Hamiltonian, $\hat{a}_j \to \hat{S}^+_j$. Thus the order parameter that describes a BEC wave function is $\psi^s_j = \langle S^+_j\rangle$, where the expectation value is obtained using spin coherent states [145]. In this mean-field description, the evolution equation for the order parameter is obtained by taking the spin-coherent state average of the Heisenberg equation of motion,

$$i\hbar\partial_t\hat{S}^+_j = \left[\hat{S}^+_j, H\right]. \tag{5.7}$$

The spin coherent state $|\tau_j\rangle$ at each site j can be parametrized as:

$$|\tau_j\rangle = e^{i\frac{\phi_j}{2}}\left[e^{-i\frac{\phi_j}{2}}\cos\frac{\theta_j}{2}|\uparrow\rangle + e^{i\frac{\phi_j}{2}}\sin\frac{\theta_j}{2}|\downarrow\rangle\right]. \tag{5.8}$$

With this choice, the HCB system is mapped to a system of classical spins [134, 146] via $\mathbf{S} = \left(\frac{\mathbf{1}}{\mathbf{2}}\sin(\theta)\cos(\phi), \frac{\mathbf{1}}{\mathbf{2}}\sin(\theta)\sin(\phi), \frac{\mathbf{1}}{\mathbf{2}}\cos(\theta)\right)$. Note that the particle density ρ_j and the condensate density ρ^s_j satisfy the relation $\rho^s_j = \rho_j\,\rho^h_j$, with $\rho^h_j = 1-\rho_j$ the hole density. In this representation, $\psi^s_j = \sqrt{\rho^s_j}e^{i\phi}$. This mean field treatment is contrasted to the standard GPE derived from the Bose-Hubbard model by taking the expectation value of the Heisenberg equation of motion with Glauber coherent states [147]. We cast the equations of motion in terms of the canonical variables

ϕ_j and $\delta_j \equiv \cos(\theta_j) = (1 - 2\rho_j)$ and obtain

$$\begin{aligned}
\dot{\delta_j} &= \frac{J}{2}\sum_{i=\pm 1}\sqrt{(1-\delta_j^2)(1-\delta_{j+i}^2)}\sin(\phi_{j+i}-\phi_j) \\
\dot{\phi_j} &= \frac{J}{2}\frac{\delta_j}{\sqrt{(1-\delta_j^2)}}\sum_{i=\pm 1}\sqrt{1-\delta_{j+i}^2}\cos(\phi_{j+i}-\phi_j) \\
&\quad -\frac{V}{2}\sum_{i=\pm 1}\delta_{j+i} - (J-V)\delta_0 \quad .
\end{aligned} \tag{5.9}$$

5.2.1 Solitary Waves in the Continuum Approximation

In the continuum approximation, the equations for the order parameter are derived from a Taylor series in the lattice spacing a [146],

$$i\hbar\dot{\psi^s} = -\frac{\hbar^2}{2m}(1-2\rho)\nabla^2\psi^s - V_e\psi^s\nabla^2\rho + U_e\rho\psi^s - \mu\psi^s \tag{5.10}$$

where $Ja^2 = \frac{\hbar^2}{m}$, $U_e = 2(J-V)$ and $V_e = Va^2$. This equation can be viewed as a generalized-GPE and we will refer to it as the HGPE in view of its relation to HCBs. The corresponding discrete Equation (5.9) will be referred to as discrete HGPE. These equations have been shown to support solitary waves [134] riding upon a background density ρ_0: $\rho(z) = \rho_0 + f(z)$, with $z = x - vt$. We obtain for the soliton solution

$$f(z,\rho_0)^{\pm} = \frac{2\gamma^2\rho_0\rho_0^h}{\pm\sqrt{(\rho_0^h-\rho_0)^2 + 4\gamma^2\rho_0\rho_0^h}\,\cosh\frac{z}{\Gamma} - (\rho_0^h-\rho_0)}, \tag{5.11}$$

where $\gamma = \sqrt{1-\bar{v}^2}$, and $\bar{v}$ being the speed of the solitary wave in units of $c_s = \sqrt{2\rho_0^s(1-V/J)}$, which is the speed of sound of the Bose gas system determined from its Bogoliubov spectrum [146]. Γ is the width of the soliton,

$$\Gamma^{-1} = \gamma\sqrt{\frac{2(1-\frac{V}{J})\rho_0\rho_0^h}{\frac{1}{4}(\rho_0^h-\rho_0)^2 + \frac{V}{J}\rho_0\rho_0^h}}. \tag{5.12}$$

The characteristic phase jump associated with the solitary waves is

$$\Delta\phi_{\pm} = (\sqrt{1-2c_s^2})\cos^{-1}\frac{\bar{v}(1-2\rho_0)}{1-2\rho_0^s\bar{v}^2}. \tag{5.13}$$

This solution has some remarkable properties. One direct consequence of the particle-hole symmetry underlying the equations of motion is the presence of two species of solitary waves,

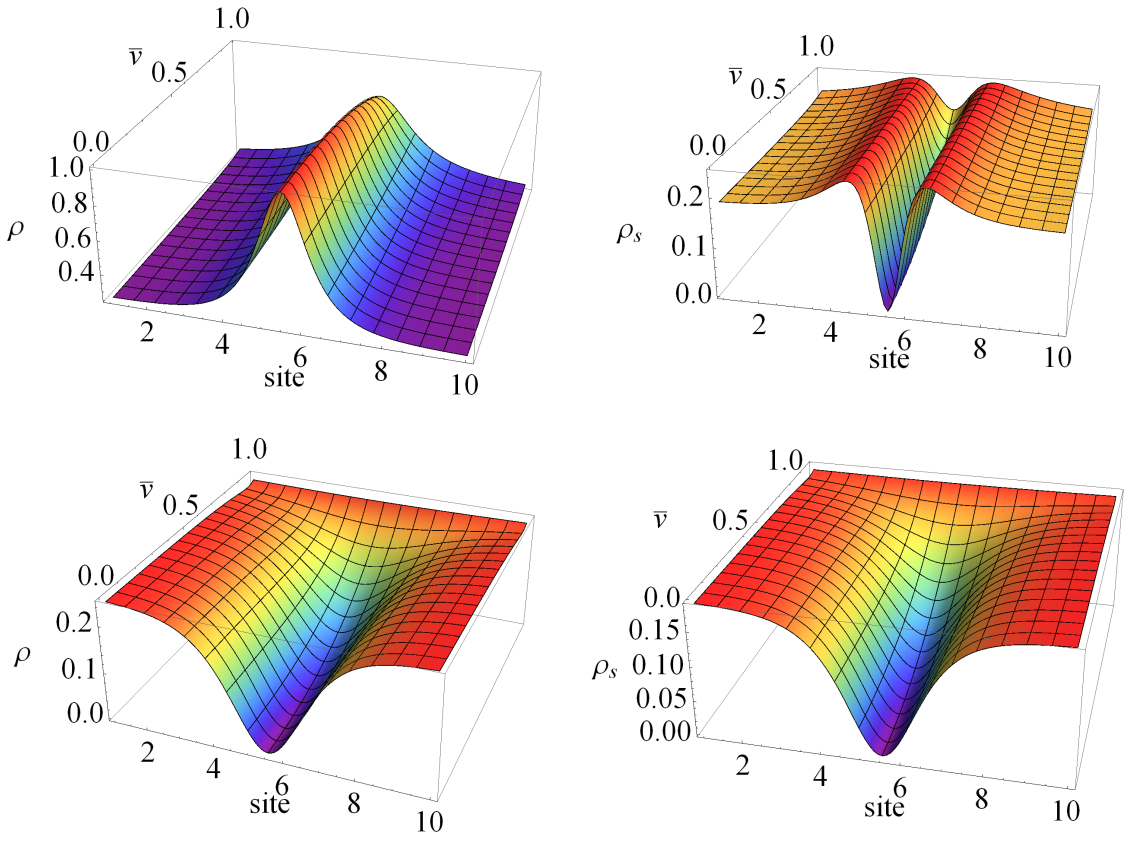

Figure 5.2: Bright (top) and dark (bottom) soliton solution in the continuum [Equation (5.11)] for $\rho_0 = 0.25$ and $V/J = 0.4$. Left panels show the density, right panels the condensate density as a function of position and speed. Note that the condensate density of the bright soliton shows a 'brightening', around the notch, i.e., it grows above the background value, whereas the dark soliton does not show this effect.

shown in Figure 5.2. The existence of $f(z, \rho_0)$ superposed on the background particle density ρ_0 implies the existence of a counterpart $f(x, \rho_0^h)$, superposed upon a corresponding hole density ρ_0^h. In fact it is easy to see that $f^{\pm}(z, \rho_0) = \pm f^{\mp}(z, \rho_0^h)$. For $\rho_0 < 1/2$, the $\pm$ corresponds to bright and dark solitons, respectively. The bright solitons have the unusual property of persisting at

speeds up to the speed of sound, in sharp contrast to the dark species that resembles the dark soliton of the GPE whose amplitude goes to zero at sound velocity. In the special case with background density equal to 1/2, the two species of solitons become mirror images of each other, as $f^+(z, \rho_0 = 1/2) = -f^-(z, \rho_0 = 1/2)$. In this case, the condensate density in fact describes the GPE-soliton [148, 149].

It should be noted that for $\rho_0 > 1/2$, the dark and bright solitons switch their roles. In other words, for $\rho_0 < 1/2$, it is the dark soliton that behaves like a GPE soliton while the bright soliton is the new type of soliton that persists all the way up to sound velocity. In contrast, for $\rho_0 > 1/2$, the bright soliton is GP-type while the dark one is the persistent soliton. In view of the particle-hole duality, we will present our results for $\rho_0 < 1/2$ in which the bright solitons have the persistent character noted above.

In the following sections, we will investigate for the existence and the lifetime of these solutions on lattice systems using mean-field equations and the time dependent DMRG. We will complement this analysis by investigating the stability of further initial states. In particular, we show that an initial Gaussian density distribution for a stationary soliton shows a similar stability if a phase jump is realized, but becomes unstable without a phase jump. This is of importance for experimental realizations indicating that imperfections in the creation of the initial state may not have a strong influence on the soliton dynamics.

5.3 Mean Field and DMRG methods

In this section, we compare the mean-field treatment of the soliton dynamics on a lattice [governed by Equations (5.9)] to the dynamics in the continuum [Equation (5.10)]. For the soliton dynamics on a lattice, we apply the equations of motion (5.9) to an initial state given by Equations (5.11) and (5.13) on a finite lattice. In Figure 5.3 we show the discrete HGPE solitons for different values of V/J at time $t = 20/J$. We compare the continuum solution (black dashed line) to the solution obtained on the lattice (symbols). As can be seen, for $V/J = 0.95$, the lattice approximation and the continuum solution show excellent agreement, up to small deviations at

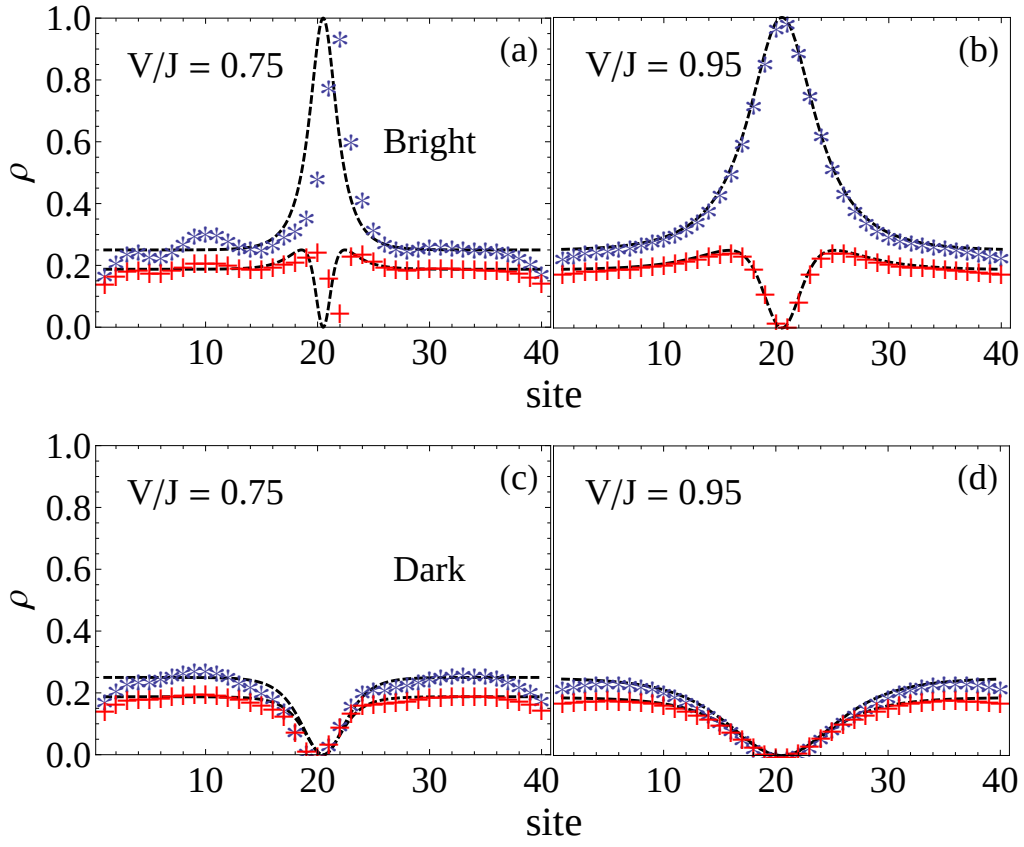

Figure 5.3: Comparison of the soliton profiles for a background density $\rho_0 = 0.25$ at times $t = 20/J$ obtained in the continuum [black dashed line, Equation (5.10)] and using the equations of motion approach Equation (5.9) on a lattice of $L = 40$ sites. The left panels show the results for $V/J = 0.75$ (narrow soliton), the right panels the case $V/J = 0.95$ (broad soliton). The top panels show the bright soliton, the bottom panels the dark soliton solution of Equation (5.11). Both, the particle density ρ $(*)$ and the condensate density ρ^s $(+)$ are shown.

the boundaries. For $V/J = 0.75$, however, significant deviations occur. We further analyze this behavior in Figure 5.4 where we compute the difference of the lattice solution to the continuum solution in the local observables (density ρ and condensate density ρ^s, respectively),

$$\Delta\rho^{(s)} = \frac{\sqrt{\sum_i \left(\left\langle \rho_i^{(s)} \right\rangle_{\text{continuum}} - \left\langle \rho_i^{(s)} \right\rangle_{\text{MF}} \right)^2}}{\sqrt{\sum_i \left\langle \rho_i^{(s)} - \rho_0^{(s)} \right\rangle^2_{\text{continuum}}}} \tag{5.14}$$

at $t = 20/J$ for a system of $L = 40$ sites as a function of V/J. As can be seen, the difference is significant for all values of $V/J \lesssim 0.8$. Only at larger values the difference is of the order of a few

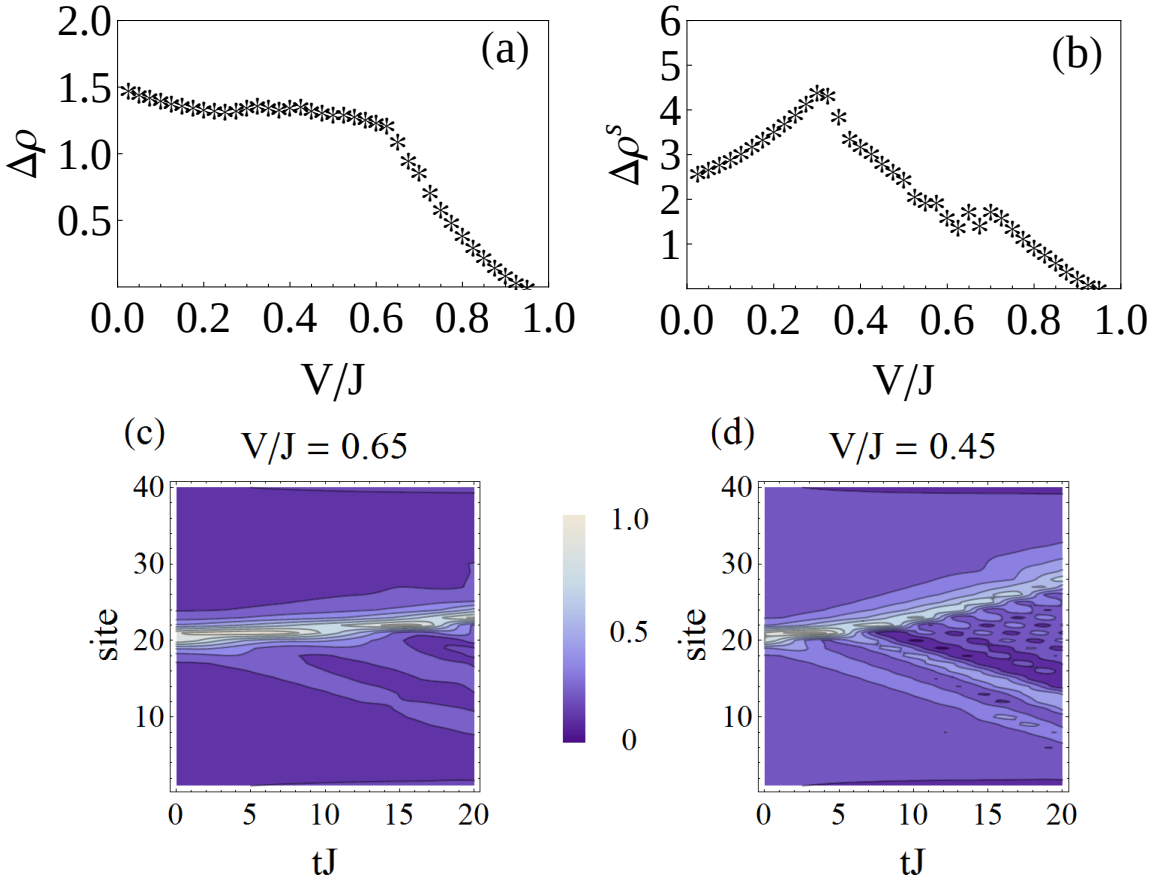

Figure 5.4: The differences resulting from Equation (5.14) of (a) the local density ρ and (b) the condensate density ρ^s between the mean-field continuum evolution and the mean-field lattice evolution on a lattice of $L = 40$ sites at times $t = 20/J$ as a function of V/J. (c) and (d): lattice mean-field evolution of the local density for a broad soliton (c) with $V/J = 0.65$ and a narrow soliton (d) with $V/J = 0.45$.

percent.

This discrepancy between the lattice and the continuum solution is to be expected: the continuum model is an approximation to the lattice model and its validity will break down when the size of features (*e.g.*, the width of the soliton) of the analytic continuum solutions becomes comparable to the lattice spacings. This breakdown of validity can be understood in terms of the emission of Bogoliubov quasi-particles [40] for solitons which are too narrow: Analogous to the excitations in a dilute bose gas, the Bogoliubov dispersion spectrum [146] shows that a narrow perturbation excites high energy modes. We further analyze this in Figures 5.4 (c) and (d). Quasi-

particles are emitted in the course of the time evolution, and due to momentum conservation the soliton gets a velocity in the opposite direction so that it starts to move away from the original position. The narrower the soliton, the stronger the emission of quasi-particles, and as expected the lattice approximation becomes more and more unstable as the width of the soliton decreases, *i.e.*, with decreasing the value of V/J.

Note that this behavior is reminiscent of the mechanism which leads to the 'light-cone' effect in correlation functions following a quantum quench [150, 151, 152, 153, 154, 155]. In this case, the quench creates entangled quasi-particles on each lattice site which then move ballistically through the system and lead to a linear signature in the time evolution of correlation functions. In this way, the velocity of the quasi-particle excitations can be obtained [153, 154, 155]. In a similar way, we propose that the linear signatures in Figure 5.4 can be used to further analyze the properties of the quasi-particles. However, this lies beyond the scope of this work so that we leave this issue open for future investigations.

Due to the necessity of having a width of the soliton larger than a few lattice spacings, we find that we need to investigate systems with $L \geq 30$ lattice sites. Since this cannot be achieved using exact diagonalization methods for the Hamiltonian matrix, we choose to apply the adaptive t-DMRG which is capable of treating sufficiently large systems efficiently. In the following we therefore compare the lattice mean-field solution to the full quantum dynamics obtained by the DMRG for systems with $L = 40$ and $L = 100$ lattice sites and $V/J \geq 0.9$.

We solely use open boundary conditions since the DMRG performs far better in this case than in the case of periodic boundary conditions, so that we can treat larger system sizes with up to the aforementioned $L = 100$ lattice sites. However, at this point it becomes necessary to discuss the effect of the boundaries: We choose system sizes and initial widths of the solitons so that there is a wide region between the soliton and the boundary which can be considered to be 'empty'. In Figure 5.5, we compare the initial state for a system with $L = 40$ and $L = 100$ sites. As can be seen, the effect of the boundaries on the soliton is completely negligible. This remains so on time scales on which perturbations either from the boundaries reach the soliton or from the soliton reach the

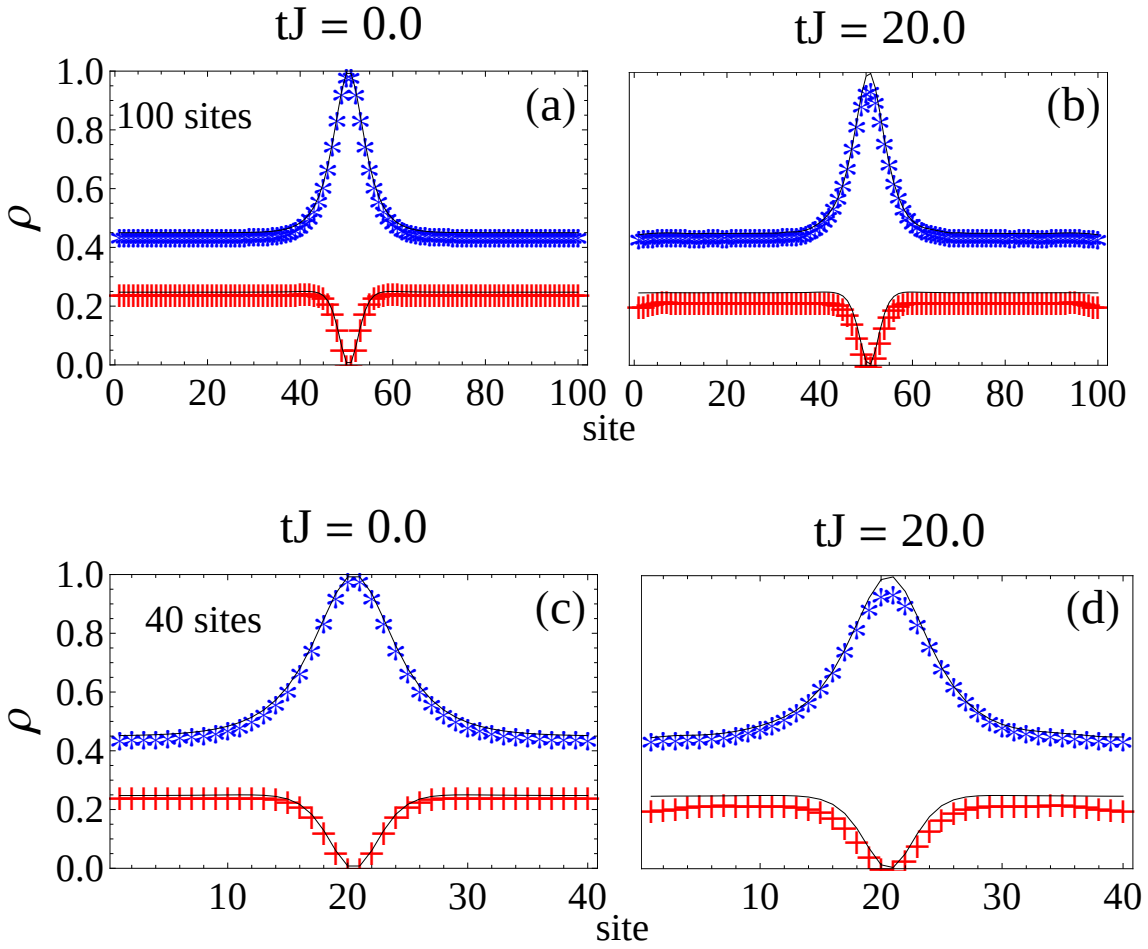

Figure 5.5: Local particle density ρ (blue $*$) and condensate density ρ^s (red $+$) obtained by DMRG (symbols) and by the mean-field ansatz (solid line) for a stationary bright soliton ($\overline{v} = 0$) at times $t = 0$ (left panels) and at times $t = 20/J$ (right panels). The plots show results for lattice sizes of $L = 100$ sites (top) and $L = 40$ sites (bottom). The parameters are $V/J = 0.95$ and $\rho_0 = 0.45$.

boundaries. At these instants of time, we stop the evolution and consider this to be the maximal reachable time for the given system size. We find that already for systems as small as $L = 40$ sites, the maximal reachable time is $t > 20/J$, so that we conclude that the analysis which we present in the following is not affected by boundary effects.

We work with the $S = 1/2$ spin system [Equation (5.4)] and engineer the initial state on the lattice by imprinting a phase and density profile by applying an external magnetic field. More

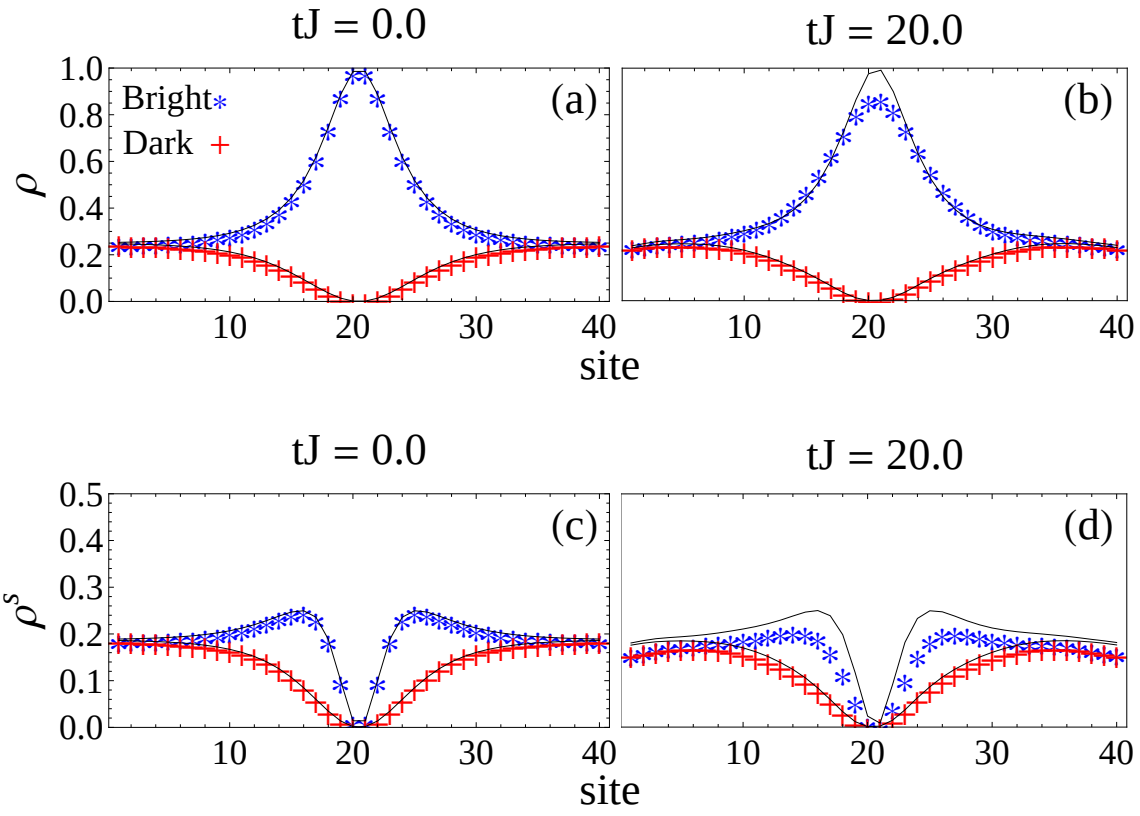

Figure 5.6: Local particle density ρ (top) and condensate density ρ^s (bottom) obtained by the DMRG (symbols) and by the mean-field (solid line) propagation of the stationary ($\overline{v} = 0$) bright (red $+$) and dark (blue $*$) solitons for times $t = 0$ and $20/J$ for a system with $L = 40$ sites. The parameters are $V/J = 0.95$ and $\rho_0 = 0.25$.

specifically, for the initial state we compute the ground state of

$$H_0 = -h \sum_j \vec{B}_j \cdot \vec{S}_j, \tag{5.15}$$

with h a large multiplicative factor (~ 100) and

$$\vec{B}_j = \left\{ \langle S_j^x \rangle = \sqrt{\rho_j(1-\rho_j)} \cos\phi_j, \langle S_j^y \rangle = \sqrt{\rho_j(1-\rho_j)} \sin\phi_j, \langle S_j^z \rangle = 0.5 - \rho_j \right\}. \tag{5.16}$$

5.4 Full Quantum Dynamics

5.4.1 Soliton Stability

The initial soliton state is prepared as discussed in the previous section and is propagated with the XXZ spin-1/2 Hamiltonian Equation (5.4) using the adaptive t-DMRG. Snapshots of the resulting time evolution for the density profile of both, the bright and the dark soliton, with speed $\overline{v} = 0$ are shown in Figure 5.6. Since our results for moving solitons ($\overline{v} > 0$) are similar, we restrict in the following to the case of static solitons. While the mean-field solution remains essentially unchanged in time, the full quantum evolution shows some deformation of the initial state: In the course of the evolution, the total density profile widens as the peak decreases. The amount of change depends on the parameters V/J and $\overline{v}$, and is different for the bright and the dark soliton. However, as further discussed below, for V/J close enough to unity the difference between the quantum solution and the initial state remains below a few percent on a time scale $t \sim 20/J$, where the hopping amplitude due to the mapping from the spin system is $J/2$. This has to be compared to time scales reachable by experiments on optical lattices. For typical lattice depths in which a tight binding description is valid, the tunneling rate varies from $0.1 - 1$ kHz, while the typical time scale of the experiments is on the order of 1-100 milliseconds. We therefore conclude that the density profile suggests a stable soliton on the experimentally accessible time scale in the full quantum evolution. Now we turn to the condensate density. Here, at $t = 20/J$, the deviation from the mean field solution is larger. Nevertheless, as shown in Figure 5.6, the change remains within a few percent for $V/t = 0.95$, so that we conclude that both quantities identify a stable soliton solution on this time scale.

To obtain a better measure for the life time of the solitons, we analyze in Figure 5.7 for the local observables (density ρ and condensate density ρ^s, respectively) the discrepancy between the

t-DMRG evolution and the mean-field solution

$$\delta\rho^{(s)} = \frac{\sqrt{\sum_i \left(\left\langle \rho_i^{(s)} \right\rangle_{\mathrm{DMRG}} - \left\langle \rho_i^{(s)} \right\rangle_{\mathrm{MF}}\right)^2}}{\sqrt{\sum_i \left\langle \rho_i^{(s)} \right\rangle_{\mathrm{MF}}^2}}, \tag{5.17}$$

similar to our analysis in Fig. 5.4 which was based on Equation (5.14). As shown in Figure 5.7, $\delta\rho^{(s)}$ decreases significantly as V/J approaches unity or as the speed of the soliton $\overline{v}$ (in units of the speed of sound) increases. This is associated to a widening of the initial density profile when increasing V/J and a reduction of the peak amplitude for larger $\overline{v}$, so that we conclude from this analysis that for a variety of initial conditions the GPE and discrete-HGPE solitons can survive quantum fluctuations on the time scales treated. This is further confirmed in the following by the behavior of the entanglement entropy and the correlation functions.

5.4.2 Entanglement entropy and nearest neighbor correlations

A quantity that reveals the quantum nature of a state is the von Neumann or entanglement entropy in the system [156] which was defined earlier in Chapter 3,

$$S_A^{vN} = -\mathrm{Tr}(\rho_A \log \rho_A), \tag{5.18}$$

with ρ_A the reduced density matrix of a subsystem A obtained by tracing out the degrees of freedom of the remaining part of the system B. We recall from the Schmidt decomposition

$$|\psi\rangle = \sum_i \lambda_i |\phi_A^i\rangle |\phi_B^i\rangle \tag{5.19}$$

it follows that

$$S^{vN} = -\sum_i \lambda_i^2 \log \lambda_i^2, \tag{5.20}$$

with $|\phi_A^i\rangle$ and $|\phi_B^i\rangle$ the eigenstates of the reduced density matrix of subsystem A or B, respectively, and λ_i^2 the eigenvalues of the corresponding eigenstates. Since the initial states are product states on the lattice, S^{vN} is exactly zero at the beginning of the time evolution since only one of the weights is finite with $\lambda_i = 1$ while the others are exactly zero. If $S^{vN}(t)$ remains zero (or very

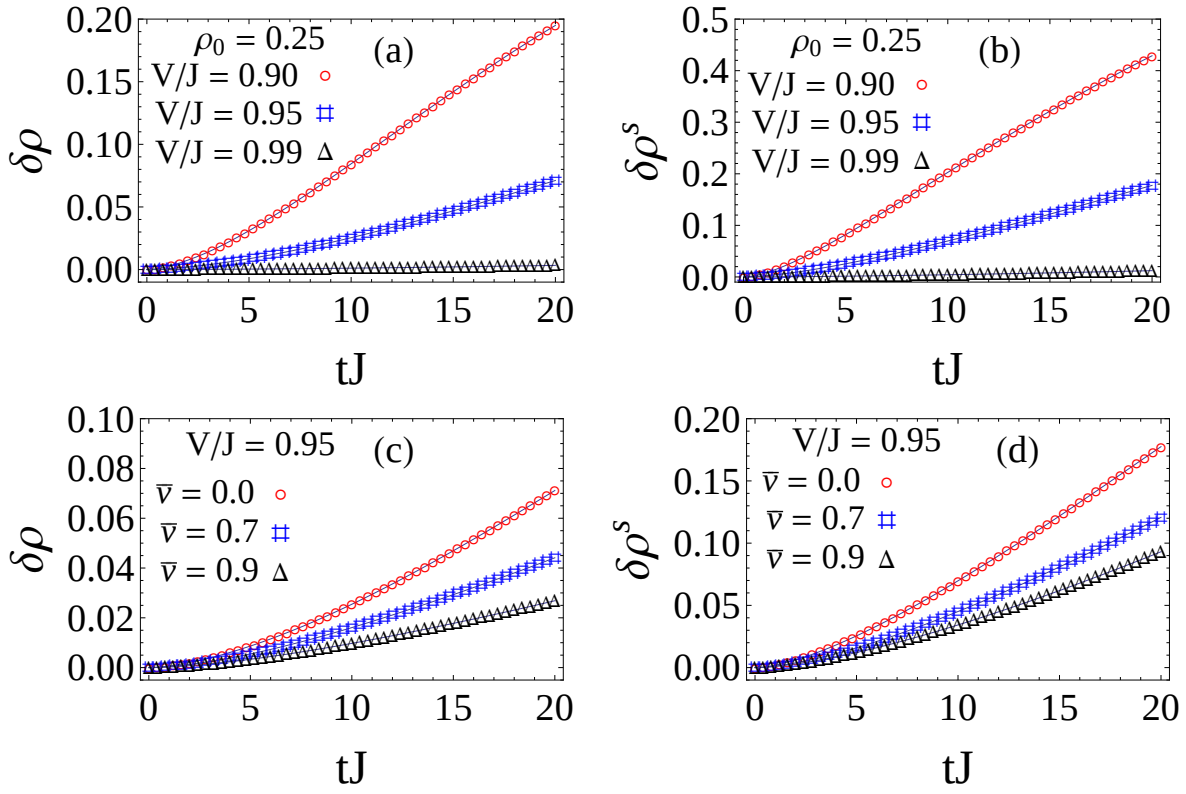

Figure 5.7: Differences using Equation (5.17) between the DMRG results and the lattice mean-field results for the total density (left) and for the condensate density (right) for a stationary (top) and for moving (bottom) bright solitons ($\rho_0 = 0.25$) on a system with $L = 40$ sites.

small) in the course of the time evolution, we conclude that quantum fluctuations do not strongly influence the nature of the initial product state, and so the value of $S^{vN}(t)$ gives an additional measure for the stability of the soliton solutions. Note that there are two variants of this analysis: in References [136, 137], the entanglement entropy for a subsystem of one single site is measured with respect to the remainder of the system. However, within the DMRG framework it is easier to consider the time evolution of the entanglement entropy for all bipartitions of the system as it is automatically computed in the course of the DMRG procedure. For simplicity, and since it gives a similar measure for the stability of the soliton, we consider here the latter. In addition, the behavior of this quantity for ground states of finite spin chains is well known from conformal field theory [61], and the numerical values can be obtained easily from the DMRG. This allows us to compare the values of the entanglement entropy during the time evolution to the ones of

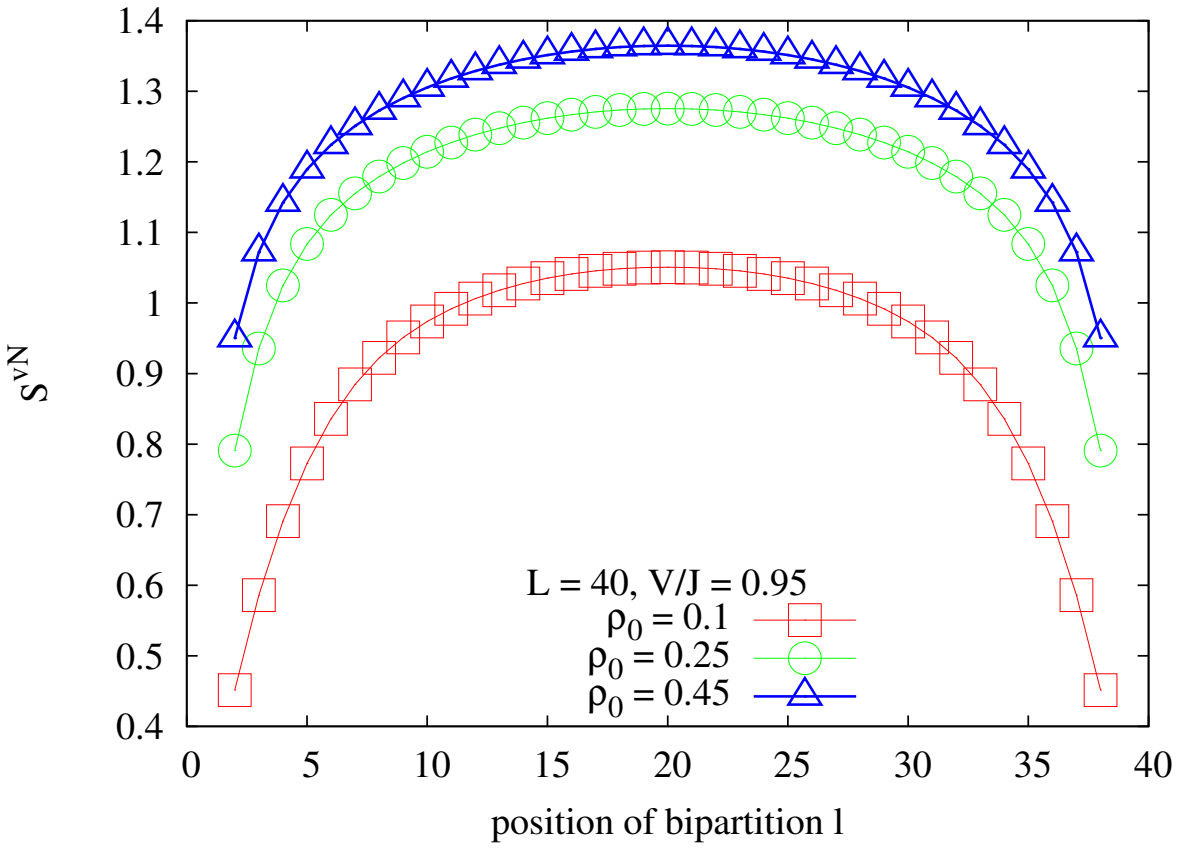

Figure 5.8: Entanglement entropy in ground states of the spin system Equation (5.4) for $V/J = 0.95$, $L = 40$ sites for values of S^z_{total} corresponding to the background density $\rho_0 = 0.1$, 0.25, and 0.45, respectively.

the strongly correlated ground state of the system which serves as a reference for how strongly entangled the state has become during the time evolution. In Figure 5.8 we show a typical result for the entanglement entropy in the ground states of the spin system Equation (5.4) with $L = 40$ sites, $V/J = 0.95$ and S_z^{total} corresponding to $\rho_0 = 0.1$, 0.25 and 0.45, respectively. As can be seen, the numerical value in the center of the system increases with ρ_0 and reaches $S^{vN,\,center} \approx 1.35$ for $\rho_0 = 0.45$.

A second estimate for the strength of the entanglement growth is to compare to the maximal possible entanglement entropy in a generic spin-1/2 chain with L sites. Consider a bipartition of the chain into M and $L - M$ spins with $M \leq L - M$. Since the dimension of the Hilbert space of

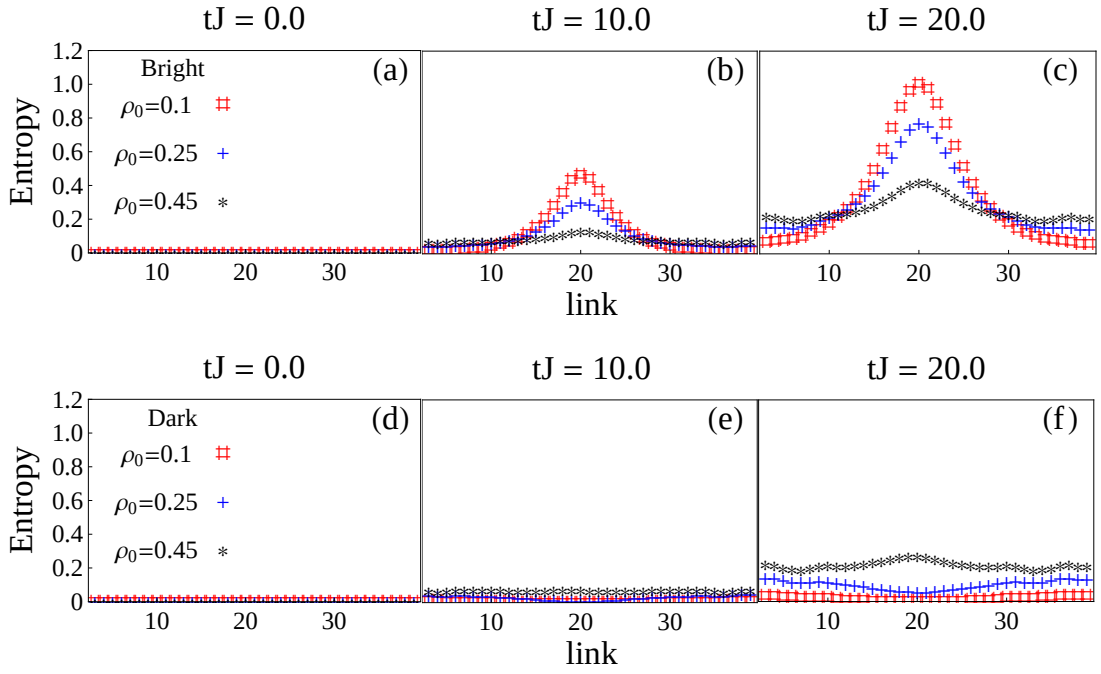

Figure 5.9: Entanglement entropies as a function of the subsystem size of the stationary bright soliton (top) and dark solitons (bottom) at different times for $V/J = 0.95$.

a chain of M spins is 2^M, a maximally entangled state is obtained when all $\lambda_j^2 = 1/2^M$. This state has an entropy

$$S^{vN,max} = -\sum_j \lambda_j^2 \log \lambda_j^2 = M \log 2.$$

For a system of $L = 40$ sites and a bipartition $M = L/2$ we therefore obtain $S^{vN,max} \approx 13.86$, *i.e.* it is a factor of ~ 10 larger than the one in the ground state for the same bipartition.

We now compare this values to the ones reached in the time evolution of the solitons. In Figure 5.9 we display the entanglement growth of both the dark and the bright soliton at $\rho_0 = 0.1$, 0.25 and 0.45, respectively. We obtain that the entanglement growth is strongest at low fillings ($\rho_0 = 0.1$), and it is larger for the bright soliton than for the dark one. For $\rho_0 = 0.45$, the maximum value for the bright soliton is $S^{vN} \approx 0.4$, and for the dark soliton $S^{vN} \approx 0.25$. Both values are significantly smaller than the one in the corresponding ground state, and much smaller than the one of the maximally entangled state. This shows that on the time scale treated, the state is significantly closer to a product state than to a strongly correlated ground state of the same system, or than

to a maximally entangled state. Since the entanglement is not negligible, quantum fluctuations play an important role for the characterization of the state towards the end of the considered time evolution, but they are not strong enough to fully destroy the product nature of the initial state.

Note that the entanglement growth for the bright soliton for $\rho_0 = 0.1$ is significantly larger than for $\rho_0 = 0.45$. This is connected to the fact that also for the local observables the corresponding initial state decays much faster. The entanglement entropy can be used as a measure to compare the stability of the initial states at $\rho_0 = 0.1$ and $\rho_0 = 0.45$: it appears that the bright soliton at $\rho_0 = 0.1$ is about half as stable as the one at $\rho_0 = 0.45$. This is reflected in the numerical values of $\delta\rho^{(s)}(t)$ which also show approximately a factor of two between the two cases.

While the entanglement entropy at the center of the system shows a peak for the bright soliton, it possesses a minimum for the dark soliton. This can be understood by the fact that the dark soliton has fewer particles at the center of the system and so quantum fluctuations are less pronounced. Due to particle-hole symmetry, the dark and bright soliton evolutions for $\rho_0 \geq 1/2$ possess the same behavior.

The behavior of the entanglement entropy can be compared to the local spin fluctuations and correlations in the system. In the mean field approach, at all times the coherent spin state enforces that $\rho_i^{s(MF)} = \rho_i(1 - \rho_i)$. This relation can be expressed in terms of spin observables, leading to $\langle S_i^x \rangle^2 + \langle S_i^y \rangle^2 + \langle S_i^z \rangle^2 = 1/4$ on each site, realizing a constraint on the local spin fluctuations. In the full quantum dynamics, this constraint is broken, so that the initial coherent state becomes modified, and entanglement is induced in the system [157].

The entanglement entropy is related to the long distance correlations and has been extensively studied in spin systems [60, 158, 159, 160, 161]. It is therefore interesting to consider the growth of correlations in our system in the course of the time evolution. For simplicity, and since they are the most relevant ones for experiments, we consider nearest neighbor spin correlations $\langle S_i \cdot S_{i+1} \rangle - \langle S_i \rangle \cdot \langle S_{i+1} \rangle$. The results shown in Fig. 5.10 show similar behavior to the entropy dynamics.

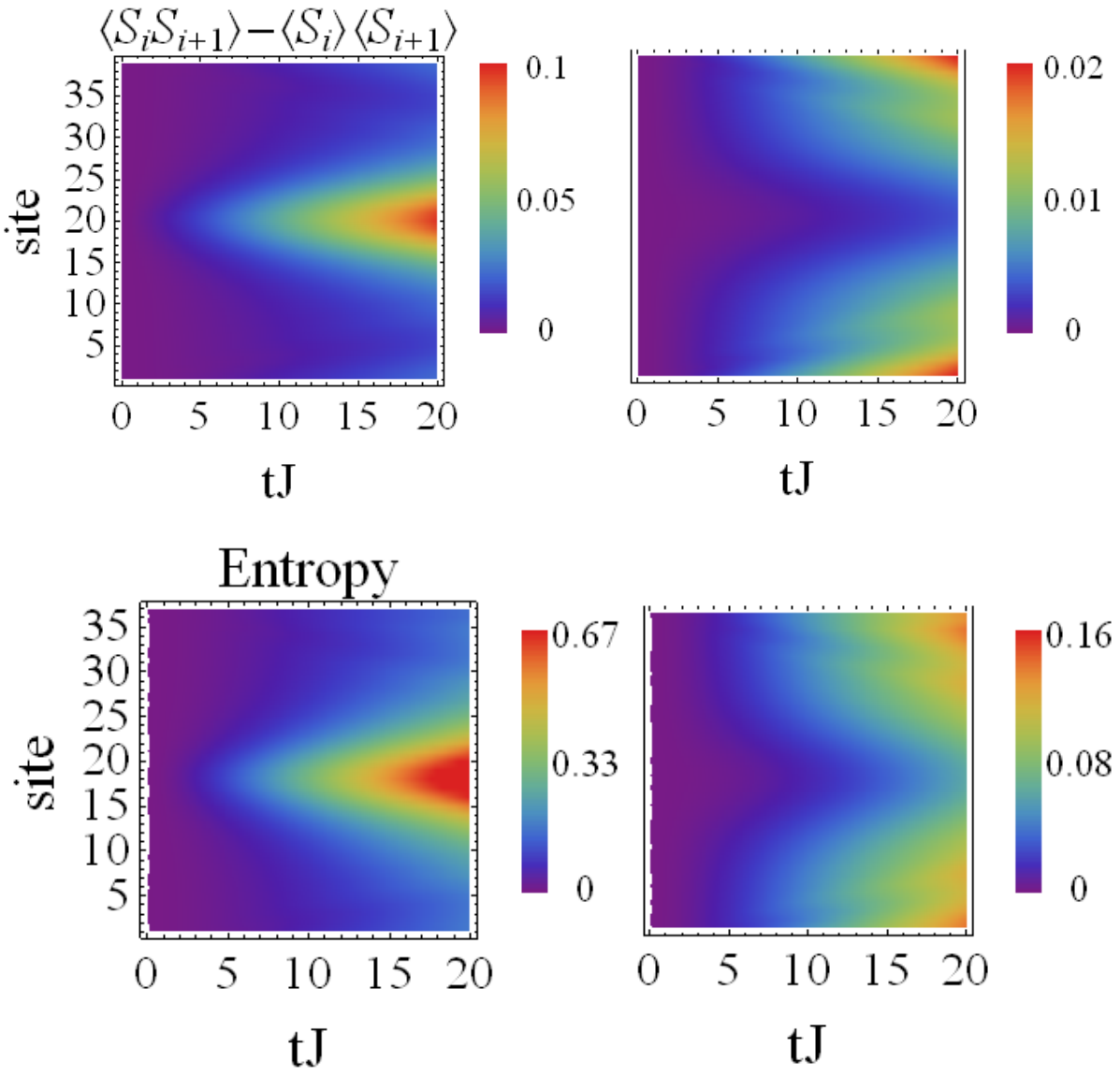

Figure 5.10: Top: contour plot of the time evolution of the nearest neighbor spin correlations $\langle S_i \cdot S_{i+1}\rangle - \langle S_i\rangle \cdot \langle S_{i+1}\rangle$ on the whole lattice for the stationary bright soliton (left) and the dark soliton (right) for $\rho_0 = 0.25$ and $V/J = 0.95$. Bottom: time evolution of the entanglement entropy for the same parameters.

5.4.3 Gaussian initial states

In this section, we test the stability of the discrete HGPE soliton solutions to modifications of the initial state. Specifically, we compare the time evolution of these solitons to that of a Gaussian

initial state (both obtained using the adaptive t-DMRG)

$$\rho(x) \sim e^{-\frac{x^2}{2\sigma^2}}, \tag{5.21}$$

which might be easier to implement in experiments [162, 144, 28]. We analyze the dynamics for initial states with and without a phase shift of π across the center in order to compare the evolution of an initial state with a similar shape and phase properties as the HGPE soliton to one which has only a similar shape. As discussed previously, the initial state is created via a Gaussian external field.

The obtained results are shown in Figure 5.11. As can be seen, the Gaussian state with a phase jump remains stable and appears to be a very good approximation to the discrete HGPE soliton. In contrast, without the phase jump, the initial wave packet quickly disperses. Note that due to the lattice the wave packet can disperse by creating two peaks moving in opposite directions. This is due to the deviation of the $\cos(k)$ dispersion of the lattice from the dispersion $\sim k^2$ of a free particle and comes into appearance if the number of particles is high enough.

We conclude, therefore, that once the phase jump is implemented, it is not necessary in the experiments to implement initial states which have exactly the form of the discrete HGPE solitons.

5.5 Experimental Realizations

In this section, we discuss possible realizations of the models introduced in Section 5.2. We start with the experimental implementation of the extended Bose Hubbard model, Equation (5.5), and its fermionic variant. The nearest neighbor interaction term V can be possibly generated in bosonic or spin polarized fermionic systems via long-range electric [163] or magnetic [164] dipolar interactions as discussed below or with a short-range interaction between atoms in higher bands of the lattice [165]. The hard-core constraint for bosons requires increasing the interactions so that there is a large energy difference between states with a different number of bosons per site. This can be achieved by tuning the scattering length via a Feshbach resonance [166]. Note that in this type of implementation, in which the spin 1/2 degrees of freedom correspond to sites with zero and

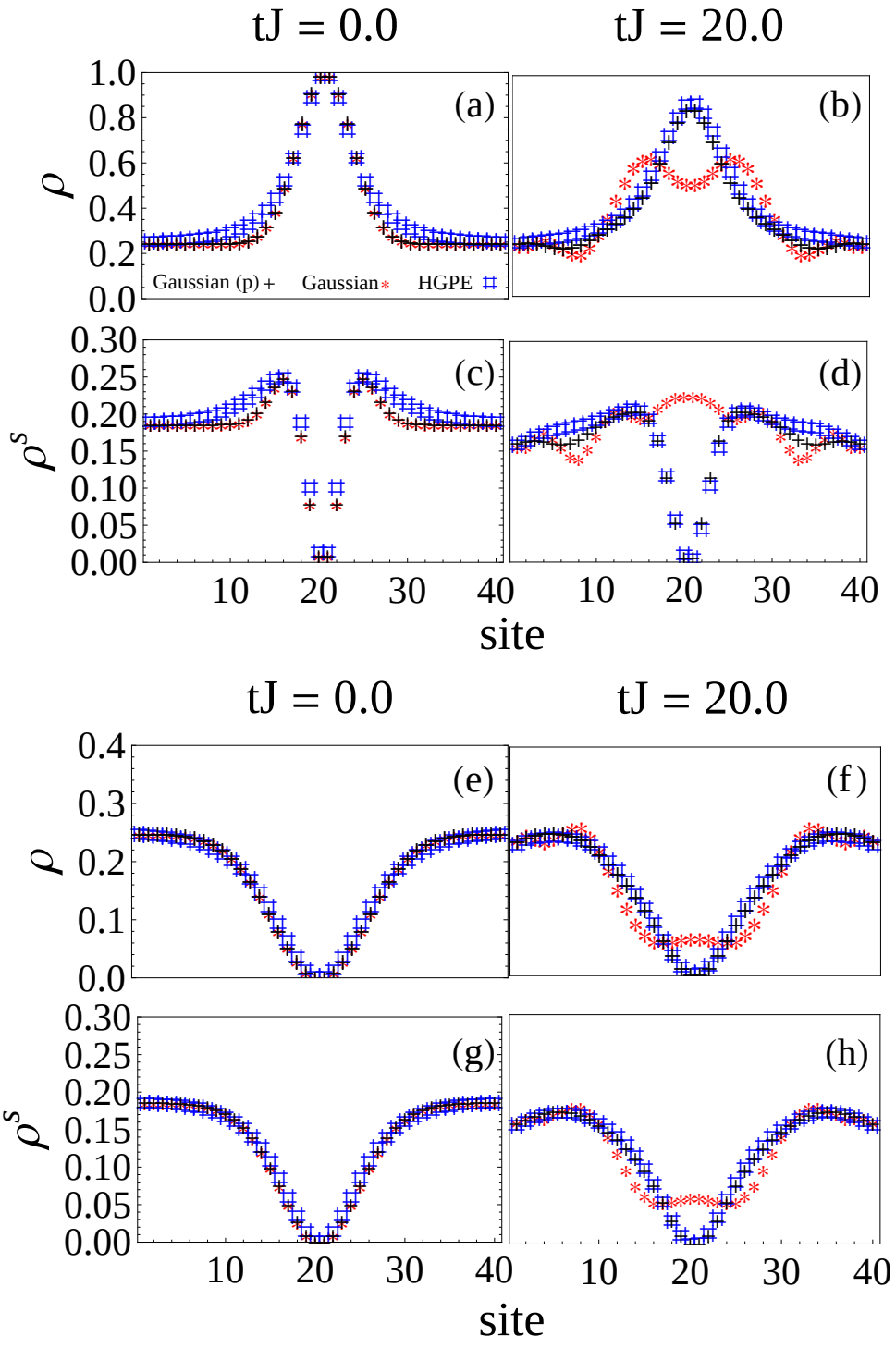

Figure 5.11: Comparison of the t-DMRG evolution of a bright (top) and dark (bottom) discrete HGPE soliton (#) to the evolution of an initial Gaussian state with (+) and without ($*$) phase imprinting for $\rho_0 = 0.25$ and $V/J = 0.95$.

one atom, the *sign* of the U and V interaction is determined by the scattering length and thus is the same for both. In our proposal, we need an attractive V interaction, so also the Hubbard U will be attractive. However, note that also in this case it is possible to realize the hard-core constraint: even though the states with one or zero atom per site do not belong to the ground state manifold, when prepared, they are metastable since there is no way to dump the excess energy, at least when prepared in the lowest band [167]. This is due to the fact that the bandwidth in a lattice is finite, which is known to lead also to repulsively bound pairs [168]. In our case, however, it prevents double occupancies, which for $|U| \to \infty$ corresponds to the HCB limit. A possible way to proceed then is to prepare the ground state in the repulsive side of the Feshbach resonance and then quickly ramp the magnetic field to the attractive side in which the evolution takes place. The atoms now are still in the lowest band and need to be promoted to higher bands using, *e.g.*, similar techniques to the ones discussed in Reference [169]. Note that the requirement of populating higher bands can indeed lead to an additional relaxation. In the fermionic system the decay to the lowest band can be blocked by filling the lowest band. The lifetime of bosons in higher bands on the other hand does require further investigation but at least recent experiments in 2D [169] reveal that it can be $10 - 100$ times longer than the characteristic time scale for intersite tunneling.

In a recent proposal, it is shown that the XXZ spin model Equation (5.4) and the spinless fermion model Equation (5.6) both can be realized in systems of polar molecules on optical lattices, even though with a long-range $1/r^3$ decay of the interactions rather than nearest-neighbor interactions only. Two different paths allow the study of the soliton dynamics in such experiments: First, as discussed in detail in References [12, 142], the spin model given in Equation (5.4) can be directly implemented in the case of unit filling (*i.e.*, one molecule per site of the optical lattice) by selecting two rotational eigenstates of the molecules which emulate the two spin degrees of freedom of the $S = 1/2$ chain. The parameters of the system can then be tuned via external DC electrical and microwave fields. The second implementation is by populating the lattice with molecules which are all in the same rotational eigenstate, emulating a spin polarized system. Since the dipolar interaction decays quickly, we presume that the effect of the interactions beyond nearest neighbor

on the soliton dynamics should be very small, so that both realizations can be used to study the soliton dynamics.

5.6 Summary

We have analyzed the stability and lifetime of HGPE solitons on 1D lattice systems driven by a XXZ-Hamiltonian which can model the behavior of bosonic atoms, fermionic polar molecules, spin systems, and spin-polarized itinerant fermions on optical lattices and in condensed matter systems. We compared the dynamics obtained in a mean field approximation to the full quantum evolution obtained using the adaptive t-DMRG and found that the solitons remain stable under the full quantum evolution on time scales $t \sim 20/J$, where $J/2$ is the unit of the hopping. This is quantified by the entanglement entropy which remained smaller than the one in the ground state of the corresponding spin system and significantly smaller then the one of a maximally entangled state on this time scale. Similar to the findings of References [136, 137], for longer times the soliton decays. However, given the time scales reachable by ongoing experiments with optical lattices, this should suffice to identify this effect in the lab. In addition, we found that imperfections in the creation of the initial state should be of minor importance, as long as the density profile and the phase jump are similar to the ones of the proposed soliton solutions. This was exemplified by a Gaussian initial state, which in the case of a phase jump showed good agreement with the soliton solution, while in the absence of the phase jump became completely unstable. Due to the tunability of parameters either via Feshbach resonances for atomic systems or via electric and microwave fields in the case of polar molecules, the possibility of realizing both bright and dark solitons in strongly interacting systems adds a new paradigm to the existence of coherent non-linear modes in systems of ultracold quantum gases.

Chapter 6

Collision Frequency Shift

There are many advantages to using ultracold atomic gases for precision measurements. For instance, they can have narrow linewidths and small Doppler shifts due to low velocities at cold temperatures. As a result, the frequency of the ground state hyperfine transition of Cesium-133 has been established as the timekeeping standard. However, the Cesium fountain clock has its limitiations. During the measurement process, the atoms interact. The clock frequency is highly sensitive to the interactions and this leads to frequency shifts which limit the precision of the clock measurement [170]. The endeavor to obtain better precision motivated the proposal for using fermionic atoms on optical lattices for clock spectroscopy. The idea is that interactions between identical fermions are suppressed by the Pauli exclusion principle: Two fermions in the same quantum state must have an antisymmetric spatial wave function. Fermionic alkaline-earth atoms, in particular ^{87}Sr, have been the candidate for use in optical lattice clocks due to its long-lived triplet excitation (^{3}P$_0$) an optical frequency above a ground singlet state (^{1}S$_0$) and the generation of state insensitive traps [32]. However, it was shown in the Sr optical lattice clock that density-dependent frequency shifts do arise [171, 33]. In fact, density shifts have provided the second largest contribution (after blackbody radiation shifts) to the uncertainty in optical lattice clocks [172].

Clock experiments based on Rabi spectroscopy [33] start with a nuclear-spin-polarized sample of atoms prepared in an excited state e, which is then transferred to the ground state g by illuminating the atoms during a time t_f with a probe beam detuned from the atomic resonance. The collision frequency shift is inferred by recording the final population in g as a function of the

detuning and looking for changes in the corresponding lineshape due to interactions. Although, treatment of the frequency shift was based on a static mean-field analysis [173, 174, 175, 171], this chapter aims to go beyond mean-field analysis in order to show the microscopic cause of the interaction-induced shifts in the framework of s-wave collisions based on Reference [176].

The chapter is organized as follows: In Section 6.1, we review the basic techniques of Rabi spectroscopy in the context of a dissipativeless two-level system. In Section 6.2, the mean-field treatment of the collisional frequency shift is reviewed. In Section 6.3, we formulate the microscopic model responsible for the collisonal frequency shift. This formulation goes beyond the static mean-field prescription and fully accounts for the many-body dynamics. The treatment confirms that motion-induced excitation inhomogeneity can lead to s-wave collision frequency shifts even in an initially polarized ensemble of fermions. In Section 6.4, we investigate the two-atom model in order to understand the interaction blockade mechanism of the frequency shift and we generalize the results to the many-body system in Section 6.5.

6.1 Rabi Spectroscopy

As an illustration of the Rabi method of interrogation, we consider a single two-level atom. We recall in Chapter 2, that a two-level atom ($|e\rangle$ and $|g\rangle$) in the presence of a light field is given by the Hamiltonian,

$$H = -\hbar\frac{\delta}{2}\sigma_z + \hbar\frac{\Omega}{2}\sigma_x, \tag{6.1}$$

where the Ω is Rabi frequency and the detuning δ is the difference in frequencies of the atomic transition and laser frequency. Consider an atom initially in the excited state $|e\rangle$. The time evolution of this state is $|\psi(t)\rangle = e^{-iHt}|e\rangle$ during the Rabi pulse time. The population of state $|g\rangle$, denoted by N_g, is determined by projecting the time-evolved state onto $|g\rangle$:

$$N_g(t) = |\langle g|\psi(t)\rangle|^2 = |\langle g|e^{-iHt}|e\rangle|^2. \tag{6.2}$$

Using the properties of the Pauli matrices, the population of $|g\rangle$ is easily obtained,

$$N_g(t) = \frac{\Omega^2}{\Omega^2+\delta^2}\sin^2(\frac{\hbar}{2}\sqrt{\Omega^2+\delta^2}t). \tag{6.3}$$

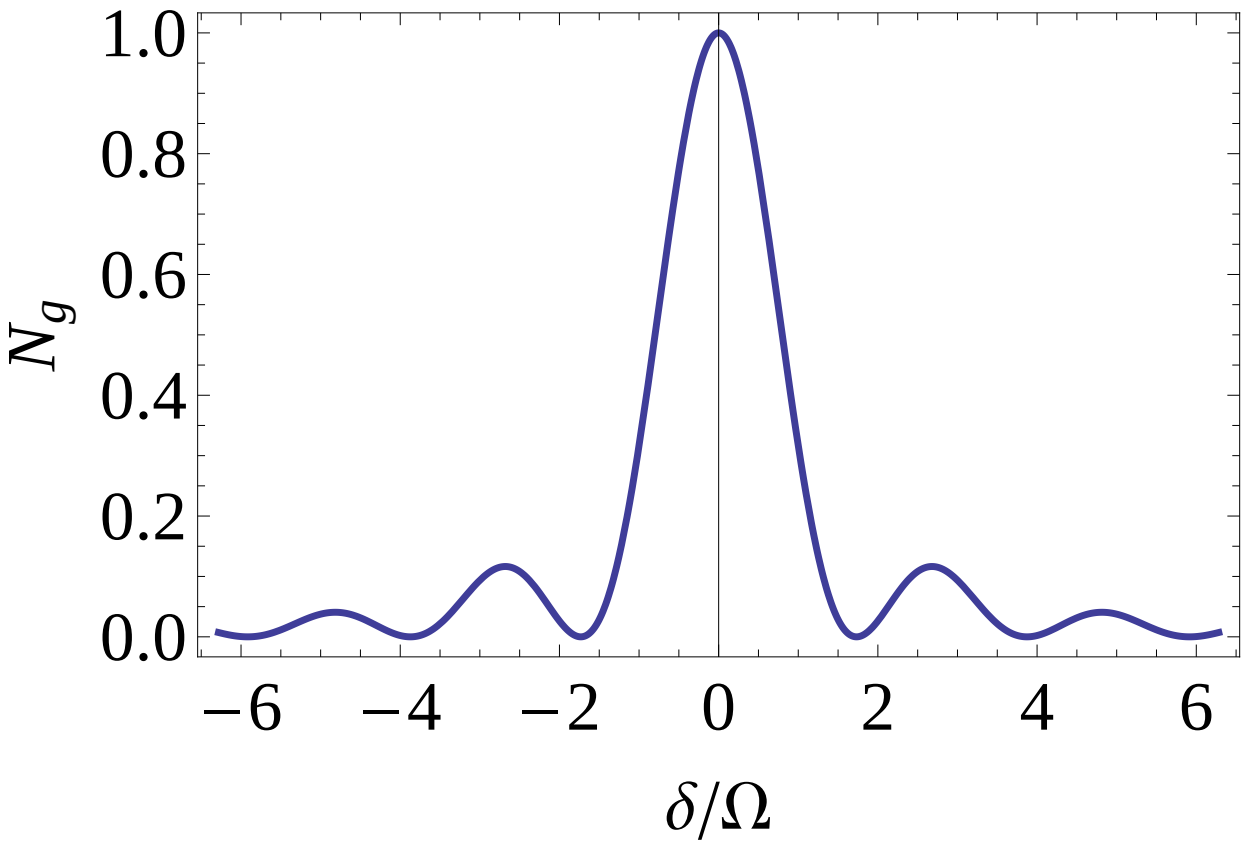

Figure 6.1: An illustration of the lineshape produced by Rabi spectroscopy after time $t = \pi/\Omega$. Maximum population of the state $|g\rangle$ occurs when the frequency of the laser δ is on resonance with the atomic transition frequency.

The form of $N_g(t)$ (see Figure 6.1) shows that the maximum population of the ground state occurs when the probe laser beam is on resonance with the atomic transition, $\delta = 0$. We will see that when Rabi spectroscopy is performed on interacting atoms, the maximum of the lineshape does not in general occur at zero detuning.

6.2 Mean-Field Treatment of Collisional Frequency Shift

We consider two-level fermions initially prepared in the electronic state $|e\rangle$ and occupy different vibrational states in the trap. Due to the inhomogeneous Rabi frequencies of fermions in different motional states [see Equation (6.10) below], the fermions do not evolve identically. This leads to an overlap which allows for collisions between fermions in different (vibrational) states.

The collision process increases the energy by,

$$E_{int} = UG_{ge}^{(2)}\rho_e\rho_g, \tag{6.4}$$

where $G_{ge}^{(2)} = \frac{\langle\hat{\rho}_e\hat{\rho}_g\rangle}{\langle\hat{\rho}_g\rangle\langle\hat{\rho}_e\rangle}$ is the two-atom correlation function and $\rho_{g,e}$ the corresponding atom densities. The correlation function is a measure of the overlap of the antisymmetrized wave function of two fermions at zero distance. The interaction strength is $U = \frac{4\pi\hbar^2 a_{eg}^-}{m}$, where a_{eg}^- is the s-wave scattering length between g and e atoms with mass m.

Atoms in state $|e\rangle$ will feel an energy shift $\mu_e = \frac{\partial E_{int}}{\partial\rho_e}$ and atoms in state $|g\rangle$ will feel an energy shift $\mu_g = \frac{\partial E_{int}}{\partial\rho_g}$ resulting in a shift between energy levels $\Delta E_{coll} = \mu_e - \mu_g$. The frequency shift due to the mean field treatment of the interactions is

$$\delta\omega_{eg} = \frac{\Delta E_{coll}}{\hbar} = \frac{4\pi\hbar a_{eg}^-}{m}G_{ge}^{(2)}(\rho_g - \rho_e) \tag{6.5}$$

For simplicity, consider a two-atom model [33]: The two fermion wave functions evolve, $|\psi_1\rangle = \alpha_1(t)|g\rangle + \beta_1(t)|e\rangle$ and $|\psi_2\rangle = \alpha_2(t)|g\rangle + \beta_2(t)|e\rangle$, during the pulse time. The antisymmetrized fermion wavefunction is

$$|\Psi\rangle = \frac{1}{\sqrt{2}}\left(|\psi_1\psi_2\rangle - |\psi_2\psi_1\rangle\right). \tag{6.6}$$

The two atom correlation function represents the overlap $G_{ge}^{(2)} = \langle\Psi|\Psi\rangle$ which is bounded between 0 and 1. The mean-field expression of the collisional frequency shift shows that an equal mixture of states will result in no shift. In addition, when inhomogeneities are not present, the fermions evolve indistinguishably and $G_{ge}^{(2)} = 0$, which also results in no shift. In the following, we will go beyond the mean-field analysis, and we will describe the microscopic effects that cause the collisional frequency shifts. We will then compare the results from the microscopic treatment and the mean field treatment.

6.3 Microscopic Model

We consider a system of nuclear-spin-polarized fermionic alkaline-earth atoms. The atoms are illuminated by a probe laser beam and they are trapped in an external potential $V(r)$ which is

indifferent to states $|e\rangle$ and $|g\rangle$ [32]. This system is represented by a single-site Hamiltonian given by [177, 11],

$$\begin{aligned}\hat{H} = &\sum_{\alpha} \int d^3r \hat{\Psi}_\alpha^\dagger \Big(\frac{-\hbar}{2m}\nabla^2 + V(r)\Big)\hat{\Psi}_\alpha + u_{eg}^- \int d^3r \hat{\rho}_e \hat{\rho}_g \\ &+ \frac{\hbar\omega_0}{2}\int d^3r\big(\hat{\rho}_e - \hat{\rho}_g\big) - \frac{\hbar\Omega_0}{2}\int d^3r\big(\hat{\Psi}_e^\dagger e^{-i(\omega_L t - k_p\cdot r)}\hat{\Psi}_g + \ h.c.\big).\end{aligned} \tag{6.7}$$

The fermionic field operator $\hat{\Psi}_\alpha$ annihilates an atom in the electronic state $\alpha = g$ ($^1S_0$) or e ($^3P_0$) while $\hat{\rho}_\alpha = \hat{\Psi}_\alpha^\dagger \hat{\Psi}_\alpha$ is the corresponding density operator. Since the nuclear spin is polarized, s-wave collisions between two fermions occur when the two atoms form an antisymmetric superposition of electronic states $|-\rangle = (|ge\rangle - |eg\rangle)/\sqrt{2}$. The interaction strength is then $u_{eg}^- = 4\pi\hbar^2 a_{eg}^-/m$, where a_{eg}^- is the s-wave scattering length between two fermions in the electronic state singlet. It is important to note that considering only s-wave collisions is an approximation that may not be valid in general. The lowest energy collisions of identical fermions are in fact p-wave. Therefore, a more accurate approximation can be made by incorporating p-wave interactions between two fermions in the electronic $|e\rangle$ state or two in the $|g\rangle$ [178]. In the third and fourth terms, $\hbar\omega_0$ is the energy splitting between the two electronic states and Ω_0 is the bare Rabi frequency.

For simplicity, we consider a 1D deep optical lattice along the z direction and isotropic confinement in the x and y transverse directions. We assume that the trap minima of the optical lattice can be approximated by harmonic potentials, and we assume the lattice in the z direction is deep enough such that the atoms occupy the lowest vibrational state in the z-direction. We then expand the field operator in terms of harmonic oscillator eigenstates,

$$\hat{\Psi}_\alpha = \sum_{\mathbf{n}} \hat{c}_{\alpha\mathbf{n}} \phi_{n_x}(x)\phi_{n_y}(y)\phi_0(z), \tag{6.8}$$

where ϕ_{n_i} is the harmonic oscillator eigenstate in the ith direction and $\hat{c}_{\alpha\mathbf{n}}^\dagger$ creates a fermion in a vibrational mode $\mathbf{n} = (n_x, n_y, n_z = 0)$ and electronic state α. Furthermore, we assume that the probe laser beam is slightly misaligned from the optical lattice axis, *i.e.*, $\mathbf{k_p} = k_z\hat{\mathbf{z}} + k_x\hat{\mathbf{x}}$ where $|k_x/k_z| \ll 1$. Using the field operator expansion above, the Hamiltonian written in the rotating

frame of the laser frequency is

$$\hat{H} = -\hbar\delta \sum_{\mathbf{n}} \hat{n}_{e\mathbf{n}} + \sum_{\alpha,\mathbf{n}} E_{\mathbf{n}} \hat{n}_{\alpha\mathbf{n}} - \sum_{\mathbf{n}} \frac{\hbar\Omega_{n_x}}{2} (\hat{c}^{\dagger}_{g\mathbf{n}} \hat{c}_{e\mathbf{n}} + \ h.c.) + u^{-}_{eg} \sum_{\mathbf{n_1 n_2 n_3 n_4}} A_{\mathbf{n_1 n_2 n_3 n_4}} \hat{c}^{\dagger}_{e\mathbf{n_1}} \hat{c}_{e\mathbf{n_2}} \hat{c}^{\dagger}_{g\mathbf{n_3}} \hat{c}_{g\mathbf{n_4}}. \tag{6.9}$$

In the first term, the detuning $\delta = \omega_L - \omega_0$ is the difference between the frequencies of the probe laser beam and clock transition. In the second term, $E_{\mathbf{n}}$ is the energy of the vibrational state $\mathbf{n}$. In the third term, $\Omega_{\mathbf{n}}$ is the motional-dependent Rabi frequency and its form is [179, 180]

$$\Omega_{n_x} = \Omega_0 \langle \phi_{n_x} \phi_0 | e^{i\mathbf{k_p}\cdot\mathbf{x}} | \phi_{n_x} \phi_0 \rangle = \Omega_0 e^{-\eta_z^2/2} e^{-\eta_x^2/2} L_{n_z}(\eta_z^2) L_{n_x}(\eta_x^2), \tag{6.10}$$

where the Lamb-Dicke parameter is $\eta_j = \frac{k_j}{2\pi}\sqrt{\frac{h}{2m\omega_j}}$ and L_{n_i} is a Laguerre polynomial. We also assume sideband transitions can be neglected. In the last term of the Hamiltonian in Equation (6.9), $A_{\mathbf{n_1 n_2 n_3 n_4}}$ is the overlap integral obtained from using the operator expansion in the density-density interaction term of the Hamiltonian in Equation (6.7) and is given by,

$$A_{\mathbf{n_1 n_2 n_3 n_4}} = \int dx \prod_{i=1}^{4} \phi_{n_{ix}}(x) \int dy \prod_{j=1}^{4} \phi_{n_{jy}}(y) \int dz \ \phi_0(z)^4. \tag{6.11}$$

The current Hamiltonian is unmanageable if we incorporate all motional eigenstates in the model. Therefore, we make further simplifications to the model:

(1) We require elastic collisions so that the indices $\mathbf{n_j}$ in the last term of the Hamiltonian in Equation (6.9) are constrained by energy conservation, $E_{\mathbf{n_1}} + E_{\mathbf{n_2}} = E_{\mathbf{n_3}} + E_{\mathbf{n_4}}$.

(2) Due to the presence of slight anharmonicity in the trap, the motional quantum numbers are forbidden to change after a collision. Therefore, the motional quantum numbers can only be exchanged after collisions. We further neglect exchanges of the motional quantum numbers along a single-axis direction.

From the above simplifications, we consider only collisions which conserve the particle number of the vibrational state $\mathbf{n}$,

$$\begin{gathered} \mathbf{n_1} = \mathbf{n_2} \quad \text{and} \quad \mathbf{n_3} = \mathbf{n_4}, \\ \text{or} \\ \mathbf{n_1} = \mathbf{n_4} \quad \text{and} \quad \mathbf{n_3} = \mathbf{n_2}. \end{gathered} \tag{6.12}$$

The allowed combinations of the motional quantum numbers reduce the calculation of the general overlap integral $A_{\mathbf{n_1 n_2 n_3 n_4}}$ for general $\mathbf{n_i}$ to the calculations of $A_{\mathbf{nnmm}}$ and $A_{\mathbf{mnnm}}$. Due to the symmetry of A, these two values are the same. We reserve the calculation of $A_{\mathbf{nnmm}}$ for appendix C.

The fermions initially prepared in a single electronic state ($|e\rangle$) must occupy different motional states $\mathbf{n}$ on a single lattice site. The Hamiltonian $\hat{H}$ can then be represented in a spin-1/2 basis where the electronic state degrees of freedom ($|e\rangle$ and $|g\rangle$) map to the spin-1/2 degrees of freedom ($|\uparrow\rangle$ and $|\downarrow\rangle$). The Hamiltonian written in the spin-1/2 basis is

$$\hat{H}_S = -\delta \sum_{\mathbf{n}} \hat{S}^z_{\mathbf{n}} - \sum_{\mathbf{n}} \Omega_{n_x} \hat{S}^x_{\mathbf{n}} - \sum_{\mathbf{n}\neq\mathbf{n}'} U_{\mathbf{nm}} (\hat{S}_{\mathbf{n}} \cdot \hat{S}_{\mathbf{m}} - 1/4), \tag{6.13}$$

where the second term in the Hamiltonian of Equation (6.9) was ignored since it introduces a constant shift when the occupied vibrational modes are conserved. The spin coupling is $U_{\mathbf{nm}} = u^-_{eg} A_{\mathbf{nnmm}}$ and the spin operator is $\hat{S}^j_{\mathbf{n}} = \frac{1}{2} \sum_{\alpha,\alpha'} \hat{c}^\dagger_{\alpha\mathbf{n}} \hat{\sigma}^j_{\alpha,\alpha'} \hat{c}_{\alpha'\mathbf{n}}$, where $\hat{\sigma}^j$ is the Pauli matrix in the $\{e, g\}$ basis along the j-th axis.

In order to illustrate how collisional frequency shifts occur, we will anlayze this model in the framework of Rabi spectroscopy of a two-atom system. This treatment is a gross simplification of the real experimental set-up where tens of atoms are trapped in each site of an optical lattice [33, 171]; nevertheless, we can develop some insight as to how collision frequency shifts arise.

6.4 Collisional Frequency Shift in Two-Atom System

We consider a system of only two atoms and in the formalism below, we set $\hbar = 1$. During the Rabi pulse, the initial state $|ee\rangle$ evolves with the Hamiltonian $\hat{H}_S$ for some time t_f , $|\psi(t_f)\rangle = e^{-i\hat{H}_S t_f}|ee\rangle$. The detuning δ, at which the maximum population of the g state occurs, determines the clock frequency. It is instructive to represent the Hamiltonian in the ordered basis, $\{|ee\rangle, |gg\rangle, (|eg\rangle +$

$|ge\rangle)/\sqrt{2}, (|eg\rangle - |ge\rangle)/\sqrt{2}\}$,

$$\hat{H}_S = \begin{pmatrix} -\delta & 0 & -\bar{\Omega}/\sqrt{2} & \Delta\Omega/\sqrt{2} \\ 0 & \delta & -\bar{\Omega}/\sqrt{2} & -\Delta\Omega/\sqrt{2} \\ -\bar{\Omega}/\sqrt{2} & -\bar{\Omega}/\sqrt{2} & 0 & 0 \\ \Delta\Omega/\sqrt{2} & -\Delta\Omega/\sqrt{2} & 0 & U_{12} \end{pmatrix}, \tag{6.14}$$

where we define $\bar{\Omega} = (\Omega_1 + \Omega_1)/2$ and $\Delta\Omega = (\Omega_1 - \Omega_2)/2$. The first three states in the ordered basis constitute the triplet manifold and the last state is the singlet state. Figure 6.2 shows the lineshape produced from Rabi spectroscopy for different values of the interaction strength. We see in the figure that when inhomogeneity of the Rabi frequencies is present, there are two limiting cases where the collision frequency shifts are absent: the noninteracting case ($U = 0$) and the strongly interacting case ($U \gg \sqrt{\bar{\Omega}^2 + \delta^2}$). For intermediate values of interaction strengths, the frequency shift is noticeable.

The collision shift arises from the inhomogeneity of the Rabi frequencies $\Delta\Omega$, which couples the initially prepared $|ee\rangle$ state to the singlet. It is the singlet state where collisions between the two atoms occur. For example, let us suppose that the Rabi frequencies are homogeneous, $\Omega_j = \bar{\Omega}$ and $\Delta\Omega = 0$. During the Rabi pulse, the evolution of the state remains within the triplet manifold since the Hamiltonian now commutes with $\hat{S}^2_{\text{total}}$. The $|g\rangle$ state population $N_g(t)$ can easily be shown to be,

$$N_g(t) = 2\frac{\bar{\Omega}^2}{\delta^2 + \bar{\Omega}^2} \sin^2\left(\frac{t\sqrt{\delta^2 + \bar{\Omega}^2}}{2}\right). \tag{6.15}$$

The $|g\rangle$ state population at any time t peaks when the detuning is $\delta = 0$ and therefore shifts are absent. Now we can qualitatively understand what happens to the collision shift when the interaction is nonzero. The Hamiltonian in the triplet manifold is diagonalized, producing a dressed triplet manifold with energies $-\sqrt{\delta^2 + \bar{\Omega}^2}$, 0, and $\sqrt{\delta^2 + \bar{\Omega}^2}$. The energy of the singlet state is separated from the middle state of the dressed triplet manifold by the interaction energy U. The inhomogeneity of the Rabi frequencies couples the triplet manifold and singlet state. When the energy gap between the singlet state and dressed triplet manifold is large, $U \gg \sqrt{\bar{\Omega}^2 + \delta^2}$, transition

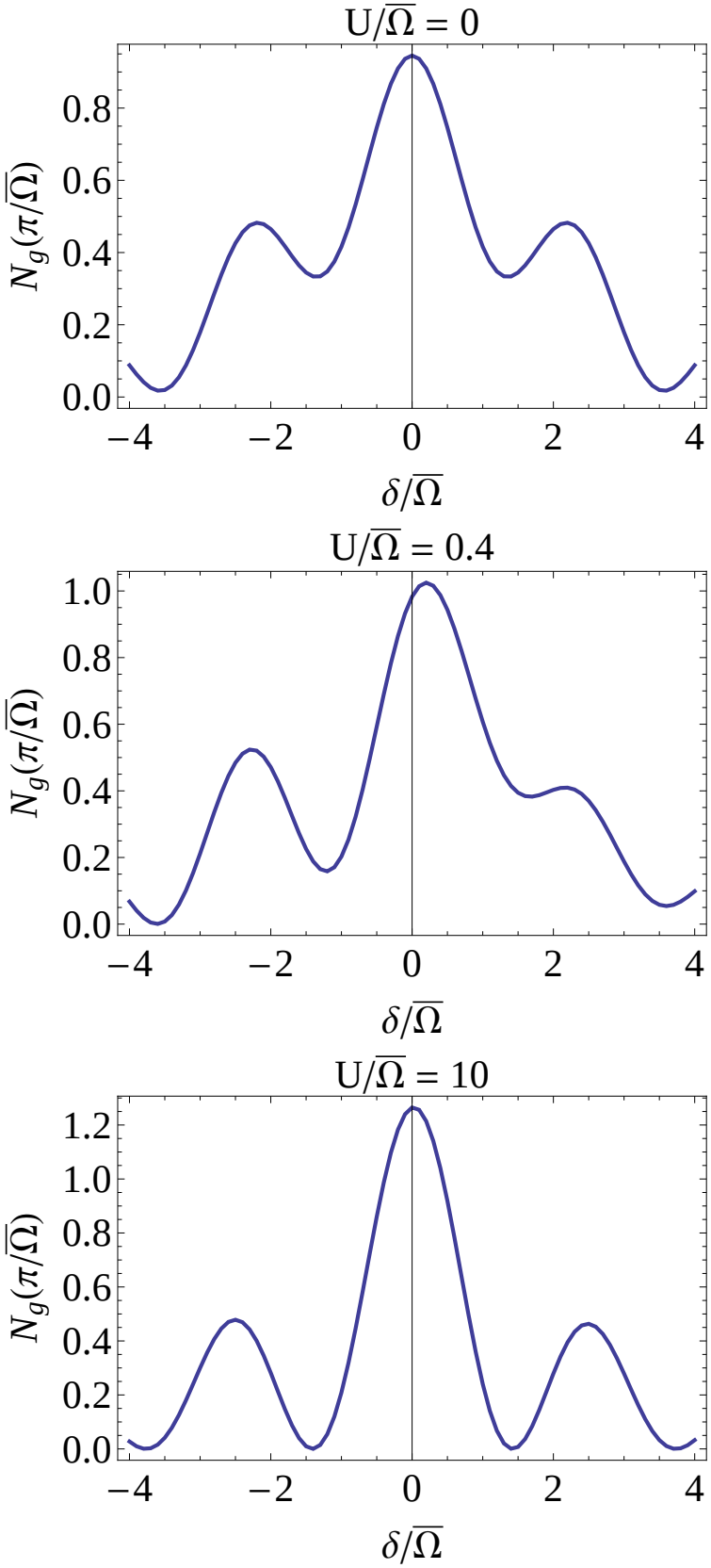

Figure 6.2: The lineshape produced from Rabi spectroscopy after time $t_f = \pi/\bar{\Omega}$ for different values of $U/\bar{\Omega}$ where $\Delta\Omega/\bar{\Omega} = 0.4$. The top and bottom plots show no collisonal frequency shift for no interaction and large interaction, respectively. The center plot show a noticeable collisional frequency shift for an intermediate interaction strength.

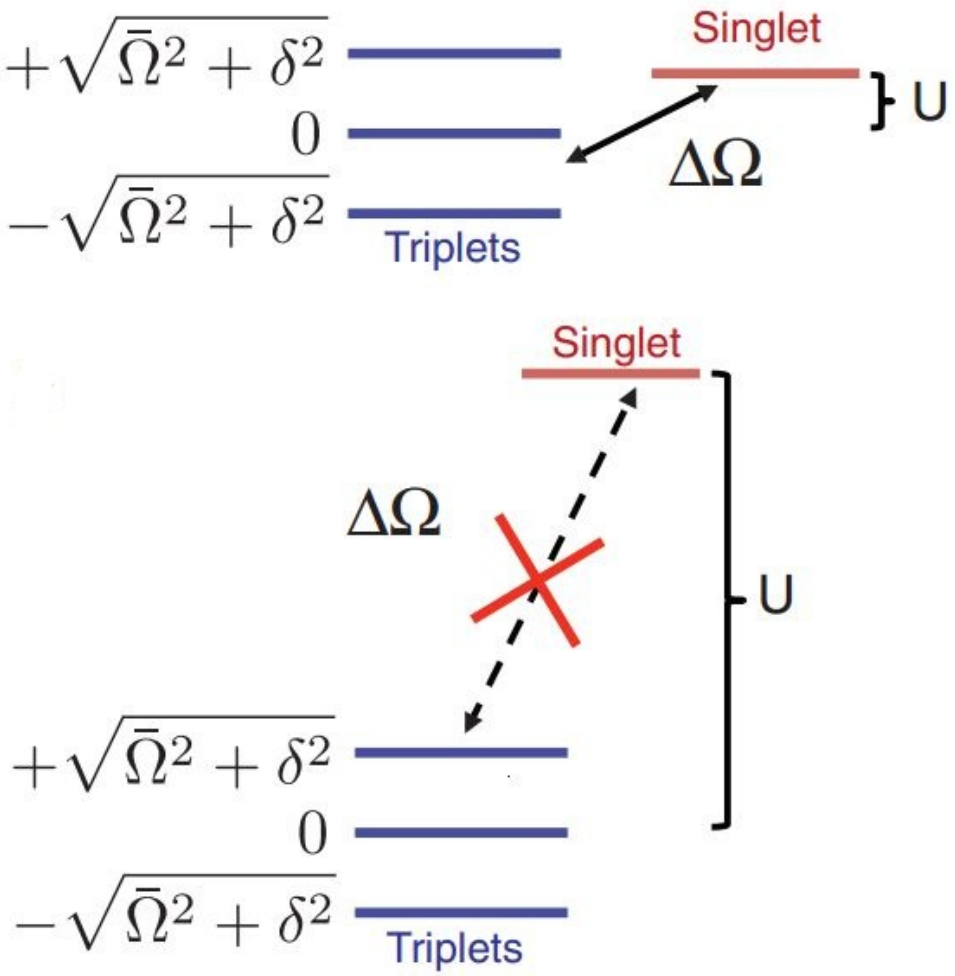

Figure 6.3: An illustration of the mechanism which suppresses collision frequency shifts in the two-atom system. When the interaction strength is comparable to the energies of the dressed triplet states, a weak inhomogeneity of the Rabi frequencies can induce transitions from the triplet to singlet manifolds. However, when the interaction strength is large compared to the dressed triplet state energies, transition from the triplet to singlet manifold is suppressed. In this case, the interaction induced frequency shifts are suppressed. [Taken from M.D. Swallows, *et. al.*, Science **331**, 1043 (2011).]

from the triplet manifold to the singlet state is suppressed during the Rabi pulse. The frequency shift is then suppressed. However, when U is comparable to the energies of the triplet manifold, inhomogeneity can cause transitions out of the triplet manifold, thereby inducing a collisional frequency shift. A diagram is shown in Figure 6.3 illustrating this mechanism [181].

6.5 Collisional Frequency Shift in the Many-Body System

The properties of the collisional frequency shift discussed in the two-atom model can be generalized to the N-atom model. In the experimental procedure for Rabi spectroscopy, the initially prepared state $|eee\ldots e\rangle$ is in the fully symmetric Dicke manifold ($S_{\text{total}} = N/2$). In the presence of excitation inhomogeneity, the Dicke manifold couples to the outside manifold of lower total spin $S_{\text{total}} = N/2 - 1$, the so called spin-wave states. In particular, collisions occur in this manifold. However, if there exists a large energy gap between states in the different manifolds, transitions outside of the Dicke manifold are suppressed [182], thereby reducing collision frequency shifts.

An analytic expression for the frequency shift $\delta\omega_{eg}$, with weak inhomogeneity of the Rabi frequencies and average interaction $\bar{U}$, has been obtained from first order time-dependent perturbation theory [176, 183]. We summarize the results of the analysis:

(1) For large interaction energies $N\bar{U} \gg \bar{\Omega}$ and Rabi pulse times $t_f N\bar{U} \gtrsim 1$, the frequency shift is $\delta\omega_{eg} \propto \frac{\sin(N\bar{U}t_f)}{(N\bar{U})^2}$ confirming the argument that in the strongly interacting limit, the shift is suppressed.

(2) In the limit $t_f \to 0$, the shift $\delta\omega_{eg} \to -\frac{(\Delta\Omega)^2 N\bar{U}}{\bar{\Omega}^2} \propto -N\bar{U}G^{(2)}_{ge}(t_f \to 0, \delta \to 0)$ consistent with the results from the mean field treatment [33, 171].

(3) $\delta\omega_{eg}$ depends on the time-averaged population difference, $\langle N_g - N_e\rangle_{t_f} = \frac{1}{t_f}\int_0^{t_f} d\tau |N_g(\tau) - N_e(\tau)|_{\delta=0,\Delta\Omega=0} = -\frac{N\sin(\bar{\Omega}t_f)}{\bar{\Omega}t_f}$ and exactly vanishes at $\bar{\Omega}t_f = \pi$ when $\langle N_g\rangle_{t_f} = \langle N_e\rangle_{t_f}$.

In the analysis above, we considered a zero temperature system. However, we can consider finite temperatures by replacing $\Delta\Omega \to \langle\Delta\Omega\rangle_T$, $\bar{\Omega} \to \langle\Delta\Omega\rangle_T$, and $\bar{U} \to \langle\bar{U}\rangle_T$. The thermal average $\langle\cdot\rangle_T$ is performed with respect to the Boltzmann weights $e^{-E_{\mathbf{n}}/(k_B T)}$. Experimental data has been fitted to the analytic results at finite temperatures as shown in Figure 6.4 demonstrating fair agreement.

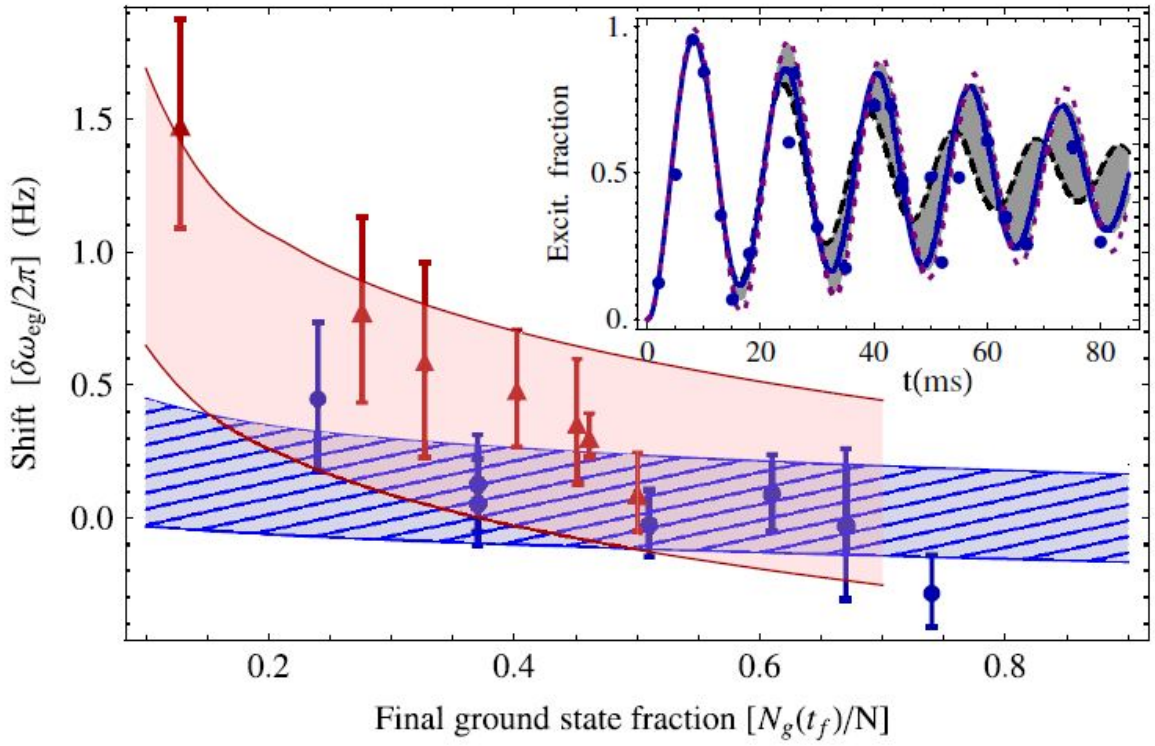

Figure 6.4: The shaded regions in the plot fit the experimental data (symbols) at different temperatures $T = 1(3)$ μK to the thermally averaged spin model. The blue circles were taken at temperature $T = 1$ μK and the red triangles at $T = 3$ μK. The area of the shaded regions indicates the variation of the pulse area $\langle\bar{\Omega}\rangle_T t_f$ in the spin model in order to account for the experimental uncertainties in the π-pulse. Inset: The solid blue (dashed black) lines are the Rabi flopping curves for $a_{eg}^- = 200a_0$ (0) with$\langle\Delta\Omega\rangle_T/\langle\bar{\Omega}\rangle_T = 0.15$. The dotted purple line is for $\langle\Delta\Omega\rangle_T/\langle\bar{\Omega}\rangle_T = 0.05$ and $a_{eg}^- = 0$. [Taken from A. M. Rey, *et. al.*, Phys. Rev. Lett. **103**, 260402 (2009).]

6.6 Summary

In this chapter, we described the microscopic model from which collisional frequency shifts arise. These shifts were shown to be caused by s-wave collisions of fermions in different motional states. Furthermore, we demonstrated from a qualitative standpoint of the two-atom system that inhomogeneity of the Rabi frequencies introduced this collisional shift. Not only does the microscopic theory capture the mean field results, it also shows that the shifts depend on the inter-particle interactions and can be suppressed by increased interactions.

The microscopic model derived in Reference [176] has been further extended to describe

experiments in 2D optical lattices and experiments in Yb optical lattice clocks. In a 1D optical lattice, the singlet state energy is comparable to the energies of the triplet manifold. A recent experiment demonstrated the suppression of collision frequency shifts in a 2D lattice, where the singlet state energy exceeds the energies of the triplet states [181]. Although the model of frequency shifts induced by s-wave collisions provided fair agreement with experiments which used Sr optical lattice clocks, it has been shown in Yb optical lattice clocks that p-wave collisions contribute a significant effect to collisional frequency shifts [178].

Chapter 7

Conclusion

In this thesis, we investigated the quantum dynamics of many-body systems in optical lattices described by the Bose-Hubbard and quantum spin models. In particular, we focused on topics related to transport and precision measurements. We used exact methods for small systems and mean field methods to gain insight into the dynamics of larger systems. Availing ourselves of the density matrix renormalization group (DMRG) method, we were able to probe the properties of the quantum dynamics for systems which could not be treated analytically. For instance, when we studied resonant dynamics on tilted optical lattices at low fillings in Chapter 4, we were able to confirm, using the DMRG time evolution of large systems, that the motion can be fully described by the dynamics of small, independent clusters of particles. The confirmation of this few-body picture allowed us to then devise a slinky-like transport scheme in these systems.

In Chapter 5, we used the same numerical method to study the quantum evolution of solitons in large systems. We demonstrated that the solitons, which were derived from a mean-field approach, were stable under quantum fluctuations for finite duration. Inherent in the numerical machinery of the DMRG method, we also found useful a quantum measure, called the entanglement entropy, to characterize how well the mean field soliton survived quantum fluctuations.

In Chapter 6, we were able to qualitatively understand with a simple two-atom picture the collisional frequency shifts which occur over the course of the quantum dynamics of the many-body system. In this case, the two-atom microscopic theory provided more insight than the mean field picture. The work reviewed in Ch. 6 has motivated further research to perform clock experiments in

the strongly interacting regime in order to suppress collisional frequency shifts, thereby increasing the accuracy and precision of optical lattice clocks.

7.1 Outlook

The systematic study of the dynamics in many-body models has revealed possibly interesting theoretical and experimental topics which can be described as a continuation of the present work. We point out natural extensions to the interesting results presented in this thesis.

In the transport study in Ch. 4, we studied resonant enhanced dynamics in a 1D system. In this case, the dynamics was reduced to a time evolution of an effective spin model which displays a quantum phase transition. We demonstrated that a signal of the quantum phase transition is present in the center-of-mass motion of the system. It would be interesting to study whether this signature also occurs in the dynamics of other systems which display a quantum phase transition. One such system of interest is the t-J model, which is used to describe high temperature superconductivity [12]. Another interesting direction includes an investigation of other resonances in the model: the resonant family was characterized as being degenerate in energy to zeroth order in the hopping when the interaction strength was equal to the linear potential strength. It would be interesting to investigate dynamics of higher-order resonances, where $U = n\Omega$ for $n = 2, 3, \ldots$ (see Appendix B.6 for a glimpse of the first steps to this subject). It would also be interesting to study the enhanced dynamics in more complex systems, such as optical lattices with higher dimensionality [184, 185] which have been studied previously in the context of quantum dimer models [85], or systems utilizing atoms that have internal structure (*e.g.*, spinor atoms) [186]. An important aspect of this work involves the development of the slinky-like transport scheme. Future work in this area should eventually involve incorporating this slinky-like transport scheme of particles into Atomtronic devices [24]. There has also been a tentative direction to possibly realize anyonic physics using the same oscillatory fields demonstrated in the slinky-scheme method of transport [187].

In Ch. 5, we studied the dynamics of a single soliton. A continuation of this work would be

to study the same quantum evolution with long-range dipolar interactions beyond nearest-neighbor sites. It would also be interesting to apply the same DMRG methods to simulate soliton collisions in the quantum evolution. The difficulty that arises when studying the collisions is twofold. First, there is an issue of finding the right parameters to produce two stable and isolated solitons. The solitons must be initially prepared so that they are sufficiently far apart. This will require either larger system sizes or narrower solitons; however, on the one hand, larger systems are numerically challenging, while on the other, the soliton is less stable as it becomes narrower. Second, the evolution must be extended for longer times. In order to retain accuracy in the DMRG evolution for larger systems and longer times, it requires more DMRG steps and a larger truncated basis. This means more computer memory and CPU time. In addition, we showed that a Gaussian wave profile evolves in a similar fashion to the soliton profile calculated from the mean field solutions. This was motivated by the presumption that a Gaussian profile would be easier to create in experiment. We further showed possible implementations of the system (for instance, with polar molecules) which will hopefully motivate an experimental investigation of these solitons.

With all the possible extensions and implications found in this work, we hope to stimulate research towards the transport of ultracold atoms in optical lattices and other unexplored directions.

Bibliography

[1] W. D. Phillips, Rev. Mod. Phys. **70**, 721 (1998).

[2] R. Pathria, Statistical Mechanics (Elsevier Butterworth-Heinemann, Oxford, 1996).

[3] M. Anderson, J. Ensher, M. Matthews, C. Wieman, and E. Cornell, Science **269**, 198 (1995).

[4] B. DeMarco and D. S. Jin, Science **285**, 1703 (1999).

[5] M. P. A. Fisher, P. B. Weichman, G. Grinstein, and D. S. Fisher, Phys. Rev. B **40**, 546 (1989).

[6] D. Jaksch, C. Bruder, J. I. Cirac, C. W. Gardiner, and P. Zoller, Phys. Rev. Lett. **81**, 3108 (1998).

[7] M. Greiner, O. Mandel, T. Esslinger, T. W. Hänsch, and I. Bloch, Nature **415**, 39 (2002).

[8] G. B. Jo, J. Guzman, C. K. Thomas, P. Hosur, A. Vishwanath, and D. M. Stamper-Kurn, Phys. Rev. Lett. **108**, 045305 (2012).

[9] M. Foss-Feig, M. Hermele, V. Gurarie, and A. M. Rey, Phys. Rev. A **82**, 053624 (2010).

[10] M. Foss-Feig, M. Hermele, and A. M. Rey, Phys. Rev. A **81**, 051603 (2010).

[11] A. Gorshkov, M. Hermele, V. Gurarie, C. Xu, P. S. Julienne, J. Ye, P. Zoller, E. Demler, M. D. Lukin, and A. M. Rey, Nature **6**, 289 (2010).

[12] A. V. Gorshkov, S. R. Manmana, G. Chen, J. Ye, E. Demler, M. D. Lukin, and A. M. Rey, Phys. Rev. Lett. **107**, 115301 (2011).

[13] S. R. White, Phys. Rev. Lett. **69**, 2863 (1992).

[14] U. Schollwöck, Rev. Mod. Phys. **77**, 259 (2005).

[15] G. Vidal, Phys. Rev. Lett. **91**, 147902 (2003).

[16] G. Vidal, Phys. Rev. Lett. **93**, 040502 (2004).

[17] M. Ben Dahan, E. Peik, J. Reichel, Y. Castin, and C. Salomon, Phys. Rev. Lett. **76**, 4508 (1996).

[18] S. R. Wilkinson, C. F. Bharucha, K. W. Madison, Q. Niu, and M. G. Raizen, Phys. Rev. Lett. **76**, 4512 (1996).

[19] C. E. Creffield, Phys. Rev. Lett. **99**, 110501 (2007).

[20] C. E. Creffield and F. Sols, Phys. Rev. Lett. **100**, 250402 (2008).

[21] C. Sias, H. Lignier, Y. P. Singh, A. Zenesini, D. Ciampini, O. Morsch, and E. Arimondo, Phys. Rev. Lett. **100**, 40404 (2008).

[22] H. Lignier, C. Sias, D. Ciampini, Y. Singh, A. Zenesini, O. Morsch, and E. Arimondo, Phys. Rev. Lett. **99**, 220403 (2007).

[23] B. T. Seaman, M. Krämer, D. Z. Anderson, and M. J. Holland, Phys. Rev. A **75**, 23615 (2007).

[24] R. A. Pepino, J. Cooper, D. Z. Anderson, and M. J. Holland, Phys. Rev. Lett. **103**, 140405 (2009).

[25] J. D. Joannopoulos, R. D. Meade, and J. N. Winn, Photonic Crystals: Molding the Flow of Light (Princeton University Press, Princeton, 1995).

[26] S. F. Mingaleev and Y. S. Kivshar, Phys. Rev. Lett. **86**, 5474 (2001).

[27] R. Slusher and B. Eggleton, Nonlinear Photonic Crystals (Springer-Verlag, Berlin, 2003).

[28] J. Denschlag, J. E. Simsarian, D. L. Feder, C. W. Clark, L. A. Collins, J. Cubizolles, L. Deng, E. W. Hagley, K. Helmerson, W. P. Reinhardt, S. L. Rolston, B. I. Schneider, and W. D. Phillips, Science **287**, 97 (2000).

[29] E. A. Ostrovskaya and Y. S. Kivshar, Phys. Rev. Lett. **90**, 160407 (2003).

[30] H. Katori, T. Ido, Y. Isoya, and M. Kuwata-Gonokami, Phys. Rev. Lett. **82**, 1116 (1999).

[31] T. W. Hänsch, Rev. Mod. Phys. **78**, 1297 (2006).

[32] J. Ye, H. J. Kimble, and H. Katori, Science **320**, 1734 (2008).

[33] G. K. Campbell, M. M. Boyd, J. W. Thomsen, M. J. Martin, S. Blatt, M. D. Swallows, T. L. Nicholson, T. Fortier, C. W. Oates, S. A. Diddams, N. D. Lemke, P. Naidon, P. Julienne, J. Ye, and A. D. Ludlow, Science **324**, 360 (2009).

[34] N. W. Ashcroft and N. D. Mermin, Solid State Physics (Holt, Rinehart, and Winston, New York, 1976).

[35] M. P. Marder, Condensed Matter Physics (John Wiley & Sons, Inc., New York, 2000).

[36] I. Abramowitz and I. A. Stegun, Handbook of Mathematical Functions (National Bureau of Standards, Washington DC, 1964).

[37] W. Kohn, Physics Review **115**, 809 (1959).

[38] J. C. Slater and G. F. Koster, Phys. Rev. **94**, 1498 (1954).

[39] J. Sakurai, Modern Quantum Mechanics (Addison-Wesley Publishing Company, Inc., Redwood City, California, 1985).

[40] C. Pethick and H. Smith, Bose-Einstein Condensation in Dilute Gases (Cambridge University Press, London, 2002).

[41] I. Bloch, J. Dalibard, and W. Zwerger, Rev. Mod. Phys. **80**, 885 (2008).

[42] S. Sachdev, Quantum Phase Transitions (Cambridge University Press, Cambridge, United Kingdom, 1999).

[43] W. S. Bakr, A. Peng, M. E. Tai, R. Ma, J. Simon, J. I. Gillen, S. Fölling, L. Pollet, and M. Greiner, Science **329**, 547 (2010).

[44] D. van Oosten, P. van der Straten, and H. T. C. Stoof, Phys. Rev. A **62**, 053601 (2002).

[45] B. Paredes, A. Widera, V. Murg, O. Mandel, S. Fölling, I. Cirac, G. V. Shlyapnikov, T. W. Hänsch, and I. Bloch, Nature **429**, 277 (2004).

[46] E. H. Lieb and W. Liniger, Phys. Rev. **130**, 1605 (1963).

[47] A. M. Rey, I. I. Satija, and C. W. Clark, Journal of Physics B: Atomic, Molecular and Optical Physics **39**, S177 (2006).

[48] E. Lieb, T. Schultz, and D. Mattis, Annals of Physics **16**, 407 (1961).

[49] M. Rigol and A. Muramatsu, Phys. Rev. A **72**, 013604 (2005).

[50] H. Bethe, Zeitschrift für Physik A Hadrons and Nuclei **71**, 205 (1931).

[51] E. Y. Loh, J. E. Gubernatis, R. T. Scalettar, S. R. White, D. J. Scalapino, and R. L. Sugar, Phys. Rev. B **41**, 9301 (1990).

[52] K. G. Wilson, Rev. Mod. Phys. **47**, 773 (1975).

[53] S. R. White, Phys. Rev. B **48**, 10345 (1993).

[54] I. Danshita and P. Naidon, Phys. Rev. A **79**, 043601 (2009).

[55] I. Danshita, J. E. Williams, C. A. R. Sá de Melo, and C. W. Clark, Phys. Rev. A **76**, 043606 (2007).

[56] I. Danshita, C. A. R. Sá de Melo, and C. W. Clark, Phys. Rev. A **77**, 063609 (2008).

[57] Y.-Y. Shi, L.-M. Duan, and G. Vidal, Phys. Rev. A **74**, 022320 (2006).

[58] G. Stewart, Introduction to Matrix Computations (Academic Press, New York, 1974).

[59] G. Vidal, J. I. Latorre, E. Rico, and A. Kitaev, Phys. Rev. Lett. **90**, 227902 (2003).

[60] A. Perales and G. Vidal, Phys. Rev. A **78**, 042337 (2008).

[61] P. Calabrese and J. Cardy, Journal of Statistical Mechanics: Theory and Experiment **2005**, P04010 (2005).

[62] S. R. Manmana, Ph.D. thesis, Universität Stuttgart, 2006.

[63] S. R. White and R. M. Noack, Phys. Rev. Lett. **68**, 3487 (1992).

[64] W. H. Press, S. A. Teukolsky, W. T. Vetterling, and B. P. Flannery, Numerical Recipes in C++, 2nd ed (Cambridge University Press, Cambridge, United Kingdom, 1993).

[65] M. A. Cazalilla and J. B. Marston, Phys. Rev. Lett. **88**, 256403 (2002).

[66] H. G. Luo, T. Xiang, and X. Q. Wang, Phys. Rev. Lett. **91**, 049701 (2003).

[67] A. E. Feiguin and S. R. White, Phys. Rev. B **72**, 020404 (2005).

[68] A. J. Daley, C. Kollath, U. Schollwöck, and G. Vidal, Journal of Statistical Mechanics: Theory and Experiment **2004**, P04005 (2004).

[69] A. J. Daley, Ph.D. thesis, University of Innsbruck, 2005.

[70] M. Suzuki, Phys. Lett. A **146**, 319 (1990).

[71] R. M. Noack and S. R. Manmana, AIP Conf. Proc. **789**, 93 (2005).

[72] T. J. Park and J. C. Light, The Journal of Chemical Physics **85**, 5870 (1986).

[73] M. Hochbruck and C. Lubich, SIAM Journal on Numerical Analysis **34**, 1911 (1997).

[74] S. R. Manmana, A. Muramatsu, and R. M. Noack, AIP Conf. Proc. **789**, 269 (2005).

[75] A. Alberti, V. V. Ivanov, G. M. Tino, and G. Ferrari, Nature Physics **5**, 547 (2009).

[76] N. Gemelke, E. Sarajlic, Y. Bidel, S. Hong, and S. Chu, Phys. Rev. Lett. **95**, 170404 (2005).

[77] V. V. Ivanov, A. Alberti, M. Schioppo, G. Ferrari, M. Artoni, M. L. Chiofalo, and G. M. Tino, Phys. Rev. Lett. **100**, 43602 (2008).

[78] C. Sias, A. Zenesini, H. Lignier, S. Wimberger, D. Ciampini, O. Morsch, and E. Arimondo, Phys. Rev. Lett. **98**, 120403 (2007).

[79] A. Micheli, A. J. Daley, D. Jaksch, and P. Zoller, Phys. Rev. Lett. **93**, 140408 (2004).

[80] A. J. Daley, S. R. Clark, D. Jaksch, and P. Zoller, Phys. Rev. A **72**, 43618 (2005).

[81] A. M. Rey, V. Gritsev, I. Bloch, E. Demler, and M. D. Lukin, Phys. Rev. Lett. **99**, 140601 (2007).

[82] A. V. Gorshkov, J. Otterbach, E. Demler, M. Fleischhauer, and M. D. Lukin, Phys. Rev. Lett. **105**, 60502 (2010).

[83] S. Sachdev, K. Sengupta, and S. M. Girvin, Phys. Rev. B **66**, 75128 (2002).

[84] J. Simon, W. S. Bakr, R. Ma, M. E. Tai, P. M. Preiss, and M. Greiner, Nature **472**, 307 (2011).

[85] S. Pielawa, T. Kitagawa, E. Berg, and S. Sachdev, Phys. Rev. B **83**, 205135 (2011).

[86] M. Glück, A. R. Kolovsky, and H. J. Korsch, Physics Reports **366**, 103 (2002).

[87] H. Moritz, T. Stöferle, M. Köhl, and T. Esslinger, Phys. Rev. Lett. **91**, 250402 (2003).

[88] C. D. Fertig, K. M. O'Hara, J. H. Huckans, S. L. Rolston, W. D. Phillips, and J. V. Porto, Phys. Rev. Lett. **94**, 120403 (2005).

[89] J. Mun, P. Medley, G. K. Campbell, L. G. Marcassa, D. E. Pritchard, and W. Ketterle, Phys. Rev. Lett. **99**, 150604 (2007).

[90] N. Strohmaier, Y. Takasu, K. Günter, R. Jördens, M. Köhl, H. Moritz, and T. Esslinger, Phys. Rev. Lett. **99**, 220601 (2007).

[91] D. McKay, M. White, M. Pasienski, and B. DeMarco, Nature **453**, 76 (2008).

[92] R. Battesti, P. Cladé, S. Guellati-Khélifa, C. Schwob, B. Grémaud, F. Nez, L. Julien, and F. Biraben, Phys. Rev. Lett. **92**, 253001 (2004).

[93] G. Ferrari, N. Poli, F. Sorrentino, and G. M. Tino, Phys. Rev. Lett. **97**, 60402 (2006).

[94] I. Carusotto, L. Pitaevskii, S. Stringari, G. Modugno, and M. Inguscio, Phys. Rev. Lett. **95**, 93202 (2005).

[95] G. H. Wannier, Physical Review **117**, 432 (1960).

[96] T. Hartmann, F. Keck, H. J. Korsch, and S. Mossmann, New Journal of Physics **6**, 2 (2004).

[97] A. Trombettoni and A. Smerzi, Phys. Rev. Lett. **86**, 2353 (2001).

[98] D. Witthaut, M. Werder, S. Mossmann, and H. J. Korsch, Phys. Rev. E **71**, 36625 (2005).

[99] A. R. Kolovsky, Phys. Rev. Lett. **90**, 213002 (2003).

[100] A. R. Kolovsky, E. A. Gómez, and H. J. Korsch, Phys. Rev. A **81**, 25603 (2010).

[101] C. Gaul, R. P. A. Lima, E. Díaz, C. A. Müller, and F. Domínguez-Adame, Phys. Rev. Lett. **102**, 255303 (2009).

[102] E. Brion, L. H. Pedersen, and K. Mølmer, Journal of Physics A: Mathematical and Theoretical **40**, 1033 (2007).

[103] M. P. Fewell, Optics Communications **253**, 125 (2005).

[104] A. R. Kolovsky, Phys. Rev. A **70**, 15604 (2004).

[105] R. H. Dicke, Physical Review **93**, 99 (1954).

[106] B. M. Peden, Ph.D. thesis, CU Boulder, 2010.

[107] S. Peil, J. V. Porto, B. L. Tolra, J. M. Obrecht, B. E. King, M. Subbotin, S. L. Rolston, and W. D. Phillips, Phys. Rev. A **67**, 51603 (2003).

[108] M. Grifoni and P. Hänggi, Physics Reports **304**, 229 (1998).

[109] A. Klumpp, D. Witthaut, and H. J. Korsch, Journal of Physics A: Mathematical and Theoretical **40**, 2299 (2007).

[110] E. Haller, R. Hart, M. J. Mark, J. G. Danzl, L. Reichsöllner, and H.-C. Nägerl, Phys. Rev. Lett. **104**, 200403 (2010).

[111] M. Hild, F. Schmitt, and R. Roth, Journal of Physics B: Atomic, Molecular and Optical Physics **39**, 4547 (2006).

[112] T. Dauxois and M. Peyrard, Physics of Solitons (Cambridge University Press, London, 2006).

[113] M. Oshikawa and I. Affleck, Phys. Rev. Lett. **79**, 2883 (1997).

[114] D. C. Dender, P. R. Hammar, D. H. Reich, C. Broholm, and G. Aeppli, Phys. Rev. Lett. **79**, 1750 (1997).

[115] F. H. L. Eßler, Phys. Rev. B **59**, 14376 (1999).

[116] I. Affleck and M. Oshikawa, Phys. Rev. B **60**, 1038 (1999).

[117] I. Affleck and M. Oshikawa, Phys. Rev. B **62**, 9200 (2000).

[118] T. Asano, H. Nojiri, Y. Inagaki, J. P. Boucher, T. Sakon, Y. Ajiro, and M. Motokawa, Phys. Rev. Lett. **84**, 5880 (2000).

[119] R. Feyerherm, S. Abens, D. Gnther, T. Ishida, M. Meiner, M. Meschke, T. Nogami, and M. Steiner, Journal of Physics: Condensed Matter **12**, 8495 (2000).

[120] M. Kohgi, K. Iwasa, J.-M. Mignot, B. Fåk, P. Gegenwart, M. Lang, A. Ochiai, H. Aoki, and T. Suzuki, Phys. Rev. Lett. **86**, 2439 (2001).

[121] A. U. B. Wolter, H. Rakoto, M. Costes, A. Honecker, W. Brenig, A. Klümper, H.-H. Klauss, F. J. Litterst, R. Feyerherm, D. Jérome, and S. Süllow, Phys. Rev. B **68**, 220406 (2003).

[122] F. H. L. Essler, A. Furusaki, and T. Hikihara, Phys. Rev. B **68**, 064410 (2003).

[123] M. Kenzelmann, Y. Chen, C. Broholm, D. H. Reich, and Y. Qiu, Phys. Rev. Lett. **93**, 017204 (2004).

[124] S. A. Zvyagin, A. K. Kolezhuk, J. Krzystek, and R. Feyerherm, Phys. Rev. Lett. **93**, 027201 (2004).

[125] H. Nojiri, Y. Ajiro, T. Asano, and J.-P. Boucher, New Journal of Physics **8**, 218 (2006).

[126] I. Umegaki, H. Tanaka, T. Ono, H. Uekusa, and H. Nojiri, Phys. Rev. B **79**, 184401 (2009).

[127] M. A. Hoefer, T. J. Silva, and M. W. Keller, Phys. Rev. B **82**, 054432 (2010).

[128] S. A. Zvyagin, E. Čižmár, M. Ozerov, J. Wosnitza, R. Feyerherm, S. R. Manmana, and F. Mila, Phys. Rev. B **83**, 060409 (2011).

[129] Y. Kivshar and G. Agrawal, Optical Solitons: From Fibers to Photonic Crystals (Academic Press, San Diego, 2003).

[130] L. Yin, Q. Lin, and G. P. Agrawal, Optics Letters **32**, 391 (2007).

[131] F. Dalfovo, S. Giorgini, L. P. Pitaevskii, and S. Stringari, Rev. Mod. Phys. **71**, 463 (1999).

[132] L. Pitaevskii and S. Stringari, Bose-Einstein Condensation (Oxford University Press, Oxford, 2003).

[133] P. Kevrekidis, D. Frantzeskakis, and R. Carretero-González, Emergent Nonlinear Phenomena in Bose-Einstein Condensates (Springer, Berlin-Heidelberg, 2008).

[134] R. Balakrishnan, I. I. Satija, and C. W. Clark, Phys. Rev. Lett. **103**, 230403 (2009).

[135] E. Demler, A. Maltsev, and A. Prokofiev, arXiv:cond-mat/1201.6400v1 (2012).

[136] R. V. Mishmash and L. D. Carr, Phys. Rev. Lett. **103**, 140403 (2009).

[137] R. V. Mishmash, I. Danshita, C. W. Clark, and L. D. Carr, Phys. Rev. A **80**, 053612 (2009).

[138] L. D. Carr, D. DeMille, R. V. Krems, and J. Ye, New Journal of Physics **11**, 055049 (2009).

[139] K.-K. Ni, S. Ospelkaus, M. H. G. de Miranda, A. Pe'er, B. Neyenhuis, J. J. Zirbel, S. Kotochigova, P. S. Julienne, D. S. Jin, and J. Ye, Science **322**, 231 (2008).

[140] K. Aikawa, D. Akamatsu, M. Hayashi, K. Oasa, J. Kobayashi, P. Naidon, T. Kishimoto, M. Ueda, and S. Inouye, Phys. Rev. Lett. **105**, 203001 (2010).

[141] J. Deiglmayr, A. Grochola, M. Repp, K. Mörtlbauer, C. Glück, J. Lange, O. Dulieu, R. Wester, and M. Weidemüller, Phys. Rev. Lett. **101**, 133004 (2008).

[142] A. V. Gorshkov, S. R. Manmana, G. Chen, E. Demler, M. D. Lukin, and A. M. Rey, Phys. Rev. A **84**, 033619 (2011).

[143] S. R. White and A. E. Feiguin, Phys. Rev. Lett. **93**, 76401 (2004).

[144] S. Burger, K. Bongs, S. Dettmer, W. Ertmer, K. Sengstock, A. Sanpera, G. V. Shlyapnikov, and M. Lewenstein, Phys. Rev. Lett. **83**, 5198 (1999).

[145] T. Matsubara and H. Matsuda, Progress of Theoretical Physics **16**, 569 (1956).

[146] R. Balakrishnan, R. Sridhar, and R. Vasudevan, Phys. Rev. B **39**, 174 (1989).

[147] J. S. Langer, Phys. Rev. **167**, 183 (1968).

[148] I. I. Satija and R. Balakrishnan, Physics Letters A **375**, 517 (2011).

[149] R. Balakrishnan and I. Satija, Pramana **77**, 929 (2011).

[150] P. Calabrese and J. Cardy, Phys. Rev. Lett. **96**, 136801 (2006).

[151] P. Calabrese and J. Cardy, Journal of Statistical Mechanics: Theory and Experiment **2007**, P06008 (2007).

[152] P. Calabrese and J. Cardy, Journal of Statistical Mechanics: Theory and Experiment **2007**, P10004 (2007).

[153] A. M. Luchli and C. Kollath, Journal of Statistical Mechanics: Theory and Experiment **2008**, P05018 (2008).

[154] S. R. Manmana, S. Wessel, R. M. Noack, and A. Muramatsu, Phys. Rev. B **79**, 155104 (2009).

[155] M. Cheneau, P. Barmettler, D. Poletti, M. Endres, P. Schauß, T. Fukuhara, C. Gross, I. Bloch, C. Kollath, and S. Kuhr, Nature **481**, 487 (2012).

[156] L. Amico, R. Fazio, A. Osterloh, and V. Vedral, Rev. Mod. Phys. **80**, 517 (2008).

[157] G. Tóth, C. Knapp, O. Gühne, and H. J. Briegel, Phys. Rev. A **79**, 042334 (2009).

[158] J. I. Latorre and A. Riera, Journal of Physics A: Mathematical and Theoretical **42**, 504002 (2009).

[159] V. Alba, M. Fagotti, and P. Calabrese, Journal of Statistical Mechanics: Theory and Experiment **2009**, P10020 (2009).

[160] B. Nienhuis, M. Campostrini, and P. Calabrese, Journal of Statistical Mechanics: Theory and Experiment **2009**, P02063 (2009).

[161] J. Sato and M. Shiroishi, Journal of Physics A: Mathematical and Theoretical **40**, 8739 (2007).

[162] W. P. Reinhardt and C. W. Clark, Journal of Physics B: Atomic, Molecular and Optical Physics **30**, L785 (1997).

[163] K. Góral, L. Santos, and M. Lewenstein, Phys. Rev. Lett. **88**, 170406 (2002).

[164] A. Griesmaier, J. Werner, S. Hensler, J. Stuhler, and T. Pfau, Phys. Rev. Lett. **94**, 160401 (2005).

[165] V. W. Scarola and S. Das Sarma, Phys. Rev. Lett. **95**, 033003 (2005).

[166] I. Bloch, J. Dalibard, and W. Zwerger, Rev. Mod. Phys. **80**, 885 (2008).

[167] R. Sensarma, D. Pekker, A. M. Rey, M. D. Lukin, and E. Demler, Phys. Rev. Lett. **107**, 145303 (2011).

[168] K. Winkler, G. Thalhammer, F. Lang, R. Grimm, J. H. Denschlag, A. Daley, A. Kantian, H. Büchler, and P. Zoller, Nature **441**, 853 (2006).

[169] T. Müller, S. Fölling, A. Widera, and I. Bloch, Phys. Rev. Lett. **99**, 200405 (2007).

[170] K. Gibble and S. Chu, Phys. Rev. Lett. **70**, 1771 (1993).

[171] S. Blatt, J. W. Thomsen, G. K. Campbell, A. D. Ludlow, M. D. Swallows, M. J. Martin, M. M. Boyd, and J. Ye, Phys. Rev. A **80**, 052703 (2009).

[172] A. D. Ludlow, T. Zelevinsky, G. K. Campbell, S. Blatt, M. M. Boyd, M. H. G. de Miranda, M. J. Martin, J. W. Thomsen, S. M. Foreman, J. Ye, T. M. Fortier, J. E. Stalnaker, S. A. Diddams, Y. Le Coq, Z. W. Barber, N. Poli, N. D. Lemke, K. M. Beck, and C. W. Oates, Science **319**, 1805 (2008).

[173] D. M. Harber, H. J. Lewandowski, J. M. McGuirk, and E. A. Cornell, Phys. Rev. A **66**, 053616 (2002).

[174] S. Gupta, Z. Hadzibabic, M. W. Zwierlein, C. A. Stan, K. Dieckmann, C. H. Schunck, E. G. M. van Kempen, B. J. Verhaar, and W. Ketterle, Science **300**, 1723 (2003).

[175] M. W. Zwierlein, Z. Hadzibabic, S. Gupta, and W. Ketterle, Phys. Rev. Lett. **91**, 250404 (2003).

[176] A. M. Rey, A. V. Gorshkov, and C. Rubbo, Phys. Rev. Lett. **103**, 260402 (2009).

[177] A. V. Gorshkov, A. M. Rey, A. J. Daley, M. M. Boyd, J. Ye, P. Zoller, and M. D. Lukin, Phys. Rev. Lett. **102**, 110503 (2009).

[178] N. D. Lemke, J. von Stecher, J. A. Sherman, A. M. Rey, C. W. Oates, and A. D. Ludlow, Phys. Rev. Lett. **107**, 103902 (2011).

[179] D. J. Wineland and W. M. Itano, Phys. Rev. A **20**, 1521 (1979).

[180] D. Leibfried, R. Blatt, C. Monroe, and D. Wineland, Rev. Mod. Phys. **75**, 281 (2003).

[181] M. D. Swallows, M. Bishof, Y. Lin, S. Blatt, M. J. Martin, A. M. Rey, and J. Ye, Science **331**, 1043 (2011).

[182] A. M. Rey, L. Jiang, M. Fleischhauer, E. Demler, and M. D. Lukin, Phys. Rev. A **77**, 052305 (2008).

[183] A. M. Rey, A. V. Gorshkov, and C. Rubbo, Phys. Rev. Lett. **105**, 049901 (2010).

[184] D. Witthaut, F. Keck, H. J. Korsch, and S. Mossmann, New Journal of Physics **6**, 41 (2004).

[185] H. Trompeter, W. Krolikowski, D. N. Neshev, A. S. Desyatnikov, A. A. Sukhorukov, Y. S. Kivshar, T. Pertsch, U. Peschel, and F. Lederer, Phys. Rev. Lett. **96**, 053903 (2006).

[186] D. Witthaut, Phys. Rev. A **82**, 033602 (2010).

[187] T. Keilmann, S. Lanzmich, I. McCulloch, and M. Roncaglia, Nature Communications **2**, 361 (2011).

[188] B. N. Parlett, The Symmetric Eigenvalue Problem (Society for Industrial and Applied Mathematics, Philadelphia, PA, 1998).

[189] L. Komzsik, The Lanczos Method: Evolution and Application (Society for Industrial and Applied Mathematics, Philadelphia, PA, 2003).

[190] B. P. Anderson and M. A. Kasevich, Science **282**, 1686 (1998).

Appendix A

A.1 Lanczos Algorithm for Iterative Diagonalization

The DMRG method involves the diagonalization of a superblock Hamiltonian during each step in the procedure. Therefore, an efficient diagonalization method is required for large matrices which arise from large physical systems with many degrees of freedom. We discuss in particular a commonly used diagonalization method called the Lanczos method. For a thorough discussion, we suggest the references [188, 189]. Suppose we are interested in diagonalizing a Hamiltonian $\mathbf{H}$ which is Hermitian. If one takes a random vector $\mathbf{x}$, which has overlap with the ground state but is not an eigenvector, the Krylov subspace $\mathbf{K^m(x)}$ is spanned by the set of states $\{\mathbf{x}, \mathbf{Hx}, \mathbf{H^2x}, \ldots, \mathbf{H^{m-1}x}\}$. The set of states determined in this way takes advantage of the fact that raising higher powers of $\mathbf{H}$ effects convergence in the direction of the eigenvector associated with the largest eigenvalue. The Lanczos algorithm is used to determine an orthonormal basis of the Krylov subspace. Based on the Arnoldi algorithm for general matrices, the Lanczos algorithm is tailored to the eigenvalue problem of symmetric and Hermitian matrices. The Lanczos basis is created by orthogonalizing using the Gram-Shmidt process. The new basis of the subspace is created by the following procedure:

(1) Randomly assign a vector $\mathbf{y_0}$. The set of orthogonal vectors $\{\mathbf{y_i}\}$ will be created but will not be immediately normalized.

(2) Set $\mathbf{y_1} = \mathbf{Hy_0} - \alpha_0\mathbf{y_0}$, where $\alpha_0 = \frac{\mathbf{y_0}^T\mathbf{Hy_0}}{\mathbf{y_0}^T\mathbf{y_0}}$. Conceptually, in the Gram-Schmidt method, one is subtracting off the projection of $\mathbf{y_0}$ onto $\mathbf{Hy_0}$ and is equivalent to choosing α_0 such

that $\mathbf{y_1}^T\mathbf{y_1}$ is a minimum.

(3) One then computes the vector, $\mathbf{y_2} = \mathbf{H}\mathbf{y_1} - \alpha_1\mathbf{y_1} - \beta_0\mathbf{y_0}$, where $\alpha_1 = \frac{\mathbf{y_1}^T\mathbf{H}\mathbf{y_1}}{\mathbf{y_1}^T\mathbf{y_1}}$ and $\beta_0 = \frac{\mathbf{y_1}^T\mathbf{H}\mathbf{y_0}}{\mathbf{y_0}^T\mathbf{y_0}}$.

(4) In the same vein, one defines the vector $\mathbf{y_3} = \mathbf{H}\mathbf{y_2} - \alpha_2\mathbf{y_2} - \beta_1\mathbf{y_1} - \gamma_0\mathbf{y_0}$, where $\gamma_0 = \frac{\mathbf{y_0}^T Hy_2}{\mathbf{y_0}^T\mathbf{y_0}}$. However, from the symmetry of $\mathbf{H}$ and the orthogonality of $\mathbf{y_2}$ to the previous vectors $\mathbf{y_1}$ and $\mathbf{y_0}$, one can easily show $\gamma_0 = 0$.

(5) Due to the symmetry of $\mathbf{H}$, the recurrence relation of the basis vectors $\{\mathbf{y_i}\}$ is in general only a three member recurrence,

$$\mathbf{y_i} = \mathbf{H}\mathbf{y_{i-1}} - \alpha_{i-1}\mathbf{y_{i-1}} - \beta_{i-2}\mathbf{y_{i-2}}. \tag{A.1}$$

The number of basis vectors is determined by the rank of $\mathbf{H}$. However, the above procedure causes the norm of each successively determined $\mathbf{y_i}$ to decrease. Due to this fact, an approximation scheme is possible by introducing a truncation at some n smaller than the rank. The Hamiltonian in the Lanczos basis has a tri-diagonial form

$$\mathbf{T_n} = \begin{pmatrix} \alpha_0 & \beta_0 & 0 & \dots & & \\ \beta_0 & \alpha_1 & \beta_1 & 0 & & \\ 0 & \beta_1 & \alpha_2 & \beta_3 & 0 & \vdots \\ \vdots & & & \ddots & & \\ & & \dots & 0 & \beta_{n-1} & \alpha_n \end{pmatrix}. \tag{A.2}$$

Diagonalization produces the eigenvectors and eigenvalues of the Hamiltonian in the Lanczos basis. Finally, the states are obtained in terms of the original Hilbert space by a standard basis transformation which is denoted $\mathbf{V_n}$ in the text in Ch. 3.

The Lanczos procedure can be used in the time evolution of a state. For a Hamiltonian with no explicit time dependence, consider the propagator $\hat{U}(\delta t) = e^{-i\delta t\hat{H}/\hbar}$ which evolves a state from time t to $t + \delta t$,

$$|\psi(t + \delta t)\rangle = e^{-i\delta t\hat{H}/\hbar}|\psi(t)\rangle. \tag{A.3}$$

In the Krylov-space approach, one performs the Lanczos procedure discussed above with $\mathbf{x} = |\psi(t)\rangle$ and $\mathbf{H} = \hat{H}$. The procedures yields the symmetric tridiagonal $n \times n$ matrix $\hat{T}_n(t) = V_n(t)^T \hat{H} V_n(t)$. The inclusion of t in the notation of the tridiagonal $\hat{T}_n(t)$ and basis transformation $V_n(t)$ matrices is not due to explicit time dependence. It is there only to indicate that the Krylov subspace was generated by $|\psi(t)\rangle$. The evolution over a single time step can now be approximated,

$$|\psi(t+\delta t)\rangle \approx |\psi(t+\delta t)\rangle_{\text{approx}} = V_n(t) e^{-i\delta t \hat{T}_n(t)/\hbar} V_n(t)^T |\psi(t)\rangle. \tag{A.4}$$

The error, given by the norm of the difference between the approximate and exact time-evolved states, decays rapidly for larger n if $n \geq |E_{\max} - E_{\min}|\, \delta t/(2\hbar)$, where $E_{\max(\min)}$ is the maximum (minimum) eigenvalue of the Hamiltonian $\hat{H}$ [73]. The appropriate choice of the time step δt should be of the order of the characteristic time scale $\hbar/|E_{\max} - E_{\min}|$ of the system. However, in order to achieve a specified accuracy in the time evolution, the number of Lanczos vectors and the time interval δt ultimately depend on the spectrum of the Hamiltonian.

Appendix B

Bloch Oscillations and Resonant Dynamics

B.1 Bloch Oscillations in the Weakly Interacting Regime

It is important to understand the mechanism by which Bloch oscillations are damped due to the introduction of weak interactions. For this, we present a review of the formalism in reference [97] but now with an additional nearest-neighbor interaction. Though nearest-neighbor interactions will be neglected when we consider resonant dynamics, the inclusion of it solely here may seed the interest of future readers in considering the effect of longer-range interactions on the dynamics. In a BEC loaded onto an optical lattice similar to the conditions in experiment [190], the system is well described by the Hamiltonian

$$H = \int \Psi^\dagger(x)(-\frac{\hbar^2}{2M}\nabla^2 + V_{ext}(x))\Psi(x)dx + \frac{1}{2}\int \Psi^\dagger(x)\Psi^\dagger(y)V(|x-y|)\Psi(y)\Psi(x)dxdy. \quad \text{(B.1)}$$

In the BEC, particles macroscopically occupy a single state which is captured in the mean-field approximation by setting the $\Psi(x)$ field operators as c-number functions. Decomposing the state operator into a linear combination of Wannier functions, $\Psi(x) = \sum \psi_n(t)\phi(x-x_n)$, the discrete nonlinear Schrödinger equation (DNLSE) is obtained,

$$H = \sum -J(\psi_n^*\psi_{n+1} + \psi_{n+1}^*\psi_n) + \epsilon_n|\psi_n|^2 + \frac{U}{2}|\psi_n|^4 + V|\psi_n|^2|\psi_{n+1}|^2, \quad \text{(B.2)}$$

where the tunneling J, external tilt potential $\epsilon_n = \Omega n$, on-site interaction U, and nearest-neighbor interaction V are integrals with respect to the localized wavefunctions. The dynamics of this system is inspected by assuming a Gaussian wavepacket ansatz,

$$\psi_n = \sqrt{k}e^{-\frac{(n-\xi)^2}{\gamma^2} + ip(n-\xi) + i\frac{\delta(n-\xi)^2}{2}},$$

where k is a normalization such that $\int_{-\infty}^{\infty}|\psi_n|^2 dn = k\gamma\sqrt{\pi/2} = N$ is the number of particles. The wavepacket is controlled by its density width γ, center ξ, momentum p, and momentum width δ. The continuum approximation is made only when the width of the Gaussian packet is large, $\gamma > 1$, which converts the sum into integrals,

$$\begin{aligned}
\int \dot{\psi}_n \psi_n^* dn &= -iNp\dot{\xi} + iN\dot{\delta}\frac{\gamma^2}{8}, \\
\int n|\psi_n|^2 dn &= N\xi, \\
\int |\psi_n|^4 dn &= \frac{N^2}{\gamma\sqrt{\pi}}, \\
\int \psi_n^* \psi_{n+1} dn &= Ne^{-ip}e^{-\eta}, \\
\int |\psi_n|^2|\psi_{n+1}|^2 dn &= \frac{N^2}{\gamma\sqrt{\pi}e^{-1/\gamma^2}}.
\end{aligned}$$

Here, $\eta = \frac{1}{2\gamma^2} + \frac{\gamma^2\delta^2}{8}$. The Lagrangian, $L = \sum i\dot{\psi}_n\psi_n^* - H$, is calculated to be,

$$L = N(p\dot{\xi} - \frac{\gamma^2}{8}\dot{\delta} + 2Je^{-\eta}\cos p - \Omega\xi - \frac{UN}{2\gamma\sqrt{\pi}} - \frac{VN}{\gamma\sqrt{\pi}}e^{-1/\gamma^2}),$$

and the Langrange equations of motion for the variables ξ, δ, γ, and p are the following,

$$\begin{aligned}
\dot{p} &= -\Omega, \\
\dot{\gamma} &= 2J\cos(p)e^{-\eta}\gamma\delta, \\
\dot{\delta} &= 2J\cos(p)e^{-\eta}(\frac{4}{\gamma^4} - \delta^2) + \frac{2UN}{\gamma^3\sqrt{\pi}} - \frac{4VN}{\sqrt{\pi}}(\frac{2}{\gamma^5} - \frac{1}{\gamma^3})e^{-1/\gamma^2}, \\
\dot{\xi} &= 2Je^{-\eta}\sin p.
\end{aligned}$$

We note that energy is conserved, $H_0 = N(-2Je^{-\eta}\cos p + \Omega\xi + \frac{UN}{2\gamma\sqrt{\pi}} + \frac{VN}{\gamma\sqrt{\pi}}e^{-1/\gamma^2})$. The equation of motion for the center of the wavepacket is given by the following,

$$\ddot{\xi} + \dot{\eta}\dot{\xi} + \Omega\cot(p)\xi = 0$$

or

$$\ddot{\xi} + N(\frac{U\delta}{2\sqrt{\pi}\gamma} + \frac{V\delta(\gamma^2-2)e^{-1/\gamma^2}}{\sqrt{\pi}\gamma^3})\dot{\xi} + \Omega^2\xi = \frac{\Omega H_0}{N} - \frac{NU\Omega}{2\gamma\sqrt{\pi}} - \frac{NV\Omega}{\gamma\sqrt{\pi}}e^{-1/\gamma^2}.$$

It can be numerically shown that γ tends to a constant for a sufficiently long time t, $\gamma \to \gamma_f$, and also $\delta(t) \to (2UN/\gamma_f^3 - 4VN(2/\gamma_f^5 - 1/\gamma_f^3)e^{-1/\gamma_f^2})t$. Therefore, in the limit of large t, the coefficient of $\dot{\xi}$ is given by,

$$\alpha = \frac{e^{-\frac{2}{\gamma_f^2}} N^2 \left(e^{\frac{1}{\gamma_f^2}} U\gamma_f^2 + 2V\left(-2+\gamma_f^2\right)\right)^2}{\pi\gamma_f^8} t.$$

We point out that $\alpha \sim t$. The time evolution of the center is then approximated as,

$$\xi(t) \sim e^{-\alpha t}\cos\Omega t$$

This approximation comes from the expansion of the hypergeometric solution for $\Omega \gg \alpha/t$ to the general differential equation, $\ddot{y} + bx\dot{y} + \omega^2 y = A$. The general solution is $y = A/\omega^2 + e_1^{-bx^2/2} F_1(1/2 - \omega^2/(2b), 1/2, bx^2/2)$. The effective mass is

$$m_*^{-1} = \frac{\partial^2 H}{\partial^2 p} = 2NJe^{-\eta}\cos p$$

Therefore, the effective mass diverges as $m_* \sim e^{\alpha(t)t}$ and is the apparent cause for the damping. We also find that V contributes to an effective onsite interaction by, $\tilde{U} = U + 2V$.

B.2 CM Motion in the Fermionized Regime

Here, we derive Eq. (4.9). We assume a lattice of infinite size centered at site $j = 0$; the time evolution of an initial single particle wavefunction $|\psi^q(t=0)\rangle$ then is

$$|\psi^q(t)\rangle = \sum_{n=-\infty}^{\infty} |\phi_n\rangle e^{-in\Omega t} \underbrace{\langle\phi_n|\psi^q(0)\rangle}_{\equiv f_n^q}, \tag{B.3}$$

with the Wannier-Stark states $|\phi_n\rangle = \sum_{j=-\infty}^{\infty} J_{j-n}(\alpha)|j\rangle$ and $\alpha = 2J/\Omega$. With this we obtain for the CM motion,

$$\begin{aligned} x_{\rm cm}^q(t) &= \frac{1}{N}\sum_j j\langle\psi^q(t)|n_j|\psi^q(t)\rangle \\ &= \frac{1}{N}\sum_j \sum_{n,m} f_m^{q*} f_n^q \langle\phi_m|n_j|\phi_n\rangle e^{-i(n-m)\Omega t} \\ &= \frac{1}{N}\sum_{n,m}\sum_j j f_m^{q*} f_n^q J_{j-m}(\alpha) J_{j-n}(\alpha) e^{-i(k-m)\Omega t}. \end{aligned} \tag{B.4}$$

Using the recurrence relation, $J_{n-1}(\alpha) + J_{n+1}(\alpha) = \frac{2n}{\alpha} J_n(\alpha)$, and the completeness relation of Bessel functions, $\sum_j J_{j-n}(\alpha) J_{j-m}(\alpha) = \delta_{n,m}$, we obtain the identity

$$\delta_{m,n+1} + \delta_{m,n-1} + \frac{2}{\alpha} n \delta_{m,n} = \frac{2}{\alpha} \sum_j j J_{j-n}(\alpha) J_{j-m}(\alpha). \tag{B.5}$$

With this, the CM motion of Eq. (B.4) takes the form

$$\begin{aligned} & x^q_{\mathrm{cm}}(t) \\ &= \frac{\alpha}{2N} \sum_{n,m} f^{q*}_m f^q_n \left(\delta_{m,n+1} + \delta_{m,n-1} + \frac{2}{\alpha} n \delta_{m,n} \right) e^{-i(n-m)\Omega t} \\ &= \sum_n \frac{n}{N} |f^q_n|^2 + \frac{J}{\Omega N} \sum_n \left(f^{q*}_{n+1} f^q_n e^{i\Omega t} + f^{q*}_{n-1} f^q_n e^{-i\Omega t} \right) \\ &= \sum_n \frac{n}{N} |f^q_n|^2 + \frac{2J}{\Omega N} \sum_n \mathrm{Re}[f^{q*}_{n+1} f^q_n e^{i\Omega t}]. \end{aligned} \tag{B.6}$$

The CM motion for the N-body system is obtained by summing over the single particle states q, resulting in Eq. (4.9). This expression is exact for an infinite system. However, for finite systems for $\Omega \gg J$ we find that this provides an excellent approximation even for system sizes as small as $L = 10$. Hence, the results from directly diagonalizing the single particle Hamiltonian shown in Fig. 4.1 and the results obtained from Eq. (4.9) are essentially identical.

B.3 Time-Dependent Perturbation Theory for a Double Well System

The time evolution of the double-well system at resonance and for strong interactions $J \ll \Omega$ is obtained by solving a set of coupled differential equations,

$$\begin{aligned} i\dot{c}_0(t) &= -\sqrt{2}\left[J c_1(t) + c_2(t) \right], \\ i\dot{c}_1(t) &= -\sqrt{2} J c_0(t), \\ i\dot{c}_2(t) &= -\sqrt{2} J c_0(t) + 2\Omega c_2(t), \end{aligned} \tag{B.7}$$

with initial conditions $c_0(0) = 1$ and $c_1(0) = c_2(0) = 0$. The non-resonant state possesses a very small population ($\sim J^2/\Omega^2$) throughout the time evolution [see Fig. B.1(b)] which justifies the zeroth-order approximation $c^{(0)}_2(t) = 0$. The set of equations then simplifies to

$$\begin{aligned} i\dot{c}^{(0)}_0(t) &= -\sqrt{2} J c^{(0)}_1(t) \\ i\dot{c}^{(0)}_1(t) &= -\sqrt{2} J c^{(0)}_0(t), \end{aligned} \tag{B.8}$$

with the initial condition $c_0^{(0)}(0) = 1$. Hence, $c_0^{(0)}(t) = \cos\left(\sqrt{2}Jt\right)$ and $c_1^{(0)}(t) = i\sin\left(\sqrt{2}Jt\right)$. With this, the first order correction on $c_2(t)$ is

$$i\dot{c}_2^{(1)}(t) = -\sqrt{2}Jc_0^{(0)}(t) + 2\Omega c_2^{(1)}(t), \tag{B.9}$$

with the initial condition $c_2^{(1)}(0) = 0$. This gives

$$\begin{aligned} c_2^{(1)}(t) &= \frac{e^{-2it\Omega}J}{\sqrt{2}\left(J^2 - 2\Omega^2\right)} \\ &\times \left[2\Omega - 2e^{2it\Omega}\Omega\cos\left(\sqrt{2}Jt\right) + i\sqrt{2}e^{2it\Omega}J\sin\left(\sqrt{2}Jt\right)\right]. \end{aligned} \tag{B.10}$$

Finally, we address the first order correction to $c_0(t)$ due to $c_2^{(1)}(t)$ by going back to the initial set of equations,

$$i\dot{c}_0^{(1)}(t) = -\sqrt{2}Jc_2^{(1)}(t) \tag{B.11}$$

with the initial conditions $c_0^{(1)}(0) = 0$. The solution with the corrections gives

$$\begin{aligned} c_0(t) &= \cos\left(\sqrt{2}Jt\right) + \frac{Je^{-2it\Omega}}{J^2 - 2\Omega^2} \\ &\times \left[-J + e^{2it\Omega}J\cos\left(\sqrt{2}Jt\right) - i\sqrt{2}e^{2it\Omega}\Omega\sin\left(\sqrt{2}Jt\right)\right] \\ c_1(t) &= i\sin\left(\sqrt{2}Jt\right) \\ c_2(t) &= \frac{Je^{-2it\Omega}}{\sqrt{2}\left(J^2 - 2\Omega^2\right)} \\ &\times \left[2\Omega - 2e^{2it\Omega}\Omega\cos\left(\sqrt{2}Jt\right) + i\sqrt{2}e^{2it\Omega}J\sin\left(\sqrt{2}Jt\right)\right]. \end{aligned} \tag{B.12}$$

The CM evolution then is

$$\begin{aligned} x_{CM}(t) &= \frac{3|c_0(t)|^2 + 2|c_1(t)|^2 + 4|c_2(t)|^2}{2} \\ &= \frac{1}{2\left(J^2 - 2\Omega^2\right)^2}\left[12J^4 - J^2\Omega^2 + 10\Omega^4\right. \\ &+ \left(3J^4 - 7J^2\Omega^2 + 2\Omega^4\right)\cos\left(2\sqrt{2}Jt\right) \\ &- 4J^2\left(3J^2 + \Omega^2\right)\cos\left(\sqrt{2}Jt\right)\cos\left(2t\Omega\right) \\ &\left.-14\sqrt{2}J^3\Omega\sin\left(\sqrt{2}Jt\right)\sin\left(2t\Omega\right)\right]. \end{aligned} \tag{B.13}$$

Since we are in the regime $J \ll \Omega$, we neglect terms beyond J^2/Ω^2 to finally obtain Eq. (4.10),

$$\begin{aligned} x_{\mathrm{cm}}(t) &\sim \frac{5}{4} + \frac{\cos\left(2\sqrt{2}Jt\right)}{4} \\ &- \frac{J^2}{8\Omega^2}\left[1 + 7\cos\left(2\sqrt{2}Jt\right) + 4\cos\left(\sqrt{2}Jt\right)\cos\left(2t\Omega\right)\right]. \end{aligned}$$

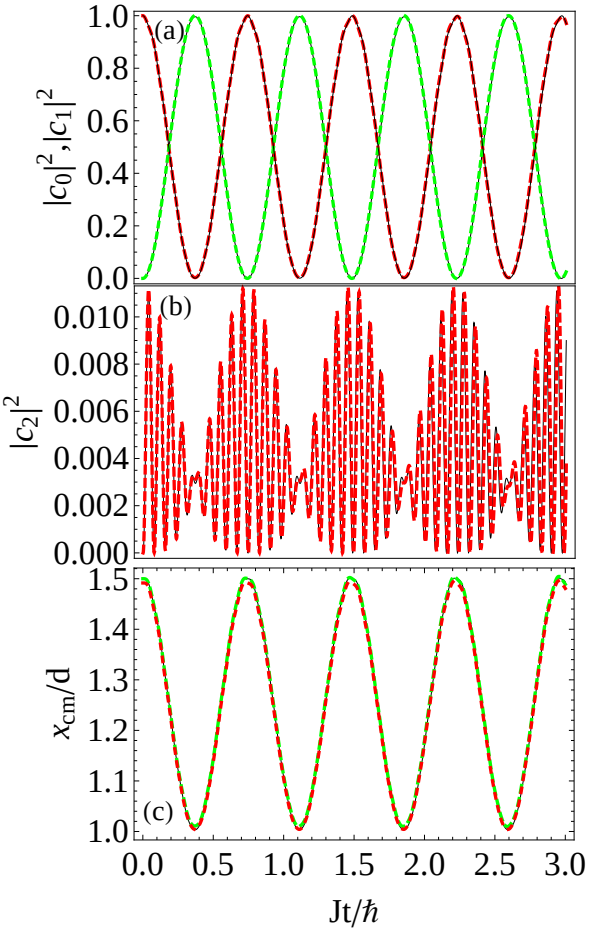

Figure B.1: Coefficients (a) $|c_0(t)|^2$, $|c_1(t)|^2$ and (b) $|c_2(t)|^2$ obtained by solving Eq. (B.7) with $J = 3.0$ and $\Omega = 40$. Note that in (b) the magnitude of $|c_2(t)|^2$ is $\sim 1\%$ of the values shown in (a). The black solid lines depict the exact numerical results whereas the dashed colored lines depict the approximate analytic solutions. The CM motion in (c) compares the exact results [black solid line], results of Eq. (B.13) which keeps terms higher than $O(J^2/\Omega^2)$ [green dashes], and the results of Eq. (4.10) which keeps only terms up to $O(J^2/\Omega^2)$ [red dashes].

B.4 Symmetric Dipole States

In order to study the symmetric states, we assume the system is fixed at L sites, drop the superscript L in Eq. (4.13), and define the states

$$|M_q\rangle = \frac{1}{\sqrt{N_M}} \sum_{k_1,..,k_M} e^{iqn_{k_1,...,k_M}} |M; k_1, ...k_M\rangle \tag{B.14}$$

where k_i denotes the position of the ith two-particle occupation and $n_{k_1,\ldots k_M} = 1 + \sum_{j=1}^{M} \binom{k_j - j}{j}$ counts each state $|M; k_1, \ldots, k_M\rangle$ from 1 to $\binom{L-M}{M}$. The components of $\vec{k}$ satisfy the constraints $k_i < k_{i+1}$, where $2i-1 \leq k_i \leq k_{i+1}-2$ and $2M-1 \leq k_M \leq L-1$. The symmetric states are denoted by $|M_{q=0}\rangle$ whereas the non-symmetric states are denoted by $|M_{q\neq 0}\rangle$. The matrix elements of the Hamiltonian (on resonance $U = \Omega$) in terms of these states is found by performing the following:

$$\begin{aligned}
\hat{H}_{\alpha,\beta} &= -J|M_\alpha\rangle\langle M_\alpha| \sum_i \hat{a}_i^\dagger \hat{a}_{i+1} + \hat{a}_{i+1}^\dagger \hat{a}_i |M+1_\beta\rangle\langle M+1_\beta| \\
&= \frac{-J|M_\alpha\rangle\langle M+1_\beta|}{\sqrt{N_M N_{M+1}}} \sum_{\vec{k},\vec{q}} e^{-i\frac{2\pi\alpha}{N_M} n_{\vec{k}}} e^{i\frac{2\pi\beta}{N_{M+1}} n_{\vec{q}}} \langle M; \vec{k}| \sum_i \hat{a}_{i+1}^\dagger \hat{a}_i |M+1; \vec{q}\rangle + h.c. \\
&= \frac{-\sqrt{2}J|M_\alpha\rangle\langle M+1_\beta|}{\sqrt{N_M N_{M+1}}} \sum_{\vec{q}} \sum_i^{M+1} e^{-i\frac{2\pi\alpha}{N_M} n_{q_1,\ldots,q_{i-1},q_{i+1},\ldots,q_{M+1}}} e^{i\frac{2\pi\beta}{N_{M+1}} n_{\vec{q}}} + h.c.,
\end{aligned}$$

where $n_{q_1,\ldots,q_{j-1},q_{j+1},\ldots,q_{M+1}} = 1 + \sum_{m=1}^{j-1} \binom{q_m - m}{m} + \sum_{m=j}^{M} \binom{q_{m+1}-m}{m}$. The form of the Hamiltonian shows that the symmetric states $|M_0\rangle$ are coupled with the non-symmetric states. It can be shown that the overlap $\omega_{M+1\to M,A} \equiv \sum_\alpha |\langle M_q|\hat{H}_{\alpha,0}|M+1_0\rangle|^2$ is largest when $M = \lfloor L/2 \rfloor$ but also that $\omega_{M+1\to M,A}$ decays as the system size increases [106].

We hypothesized that at short times, the symmetric states ($\alpha = \beta = 0$) are populated since the unit-filled states are symmetrically connected to all single dipole states. The Hamiltonian within this symmetric subspace is,

$$H_{SYM} = -\sqrt{2}J \sum_i (i+1)\sqrt{\frac{N_{i+1}}{N_i}} |i+1_0\rangle\langle i_0| + h.c. \tag{B.15}$$

The coupling term,

$$-\sqrt{2}J(M+1)\sqrt{\frac{N_{M+1}}{N_M}} = -\sqrt{2}J\sqrt{\frac{(N-2M)(N-2M-1)(M+1)}{N-M}}, \tag{B.16}$$

is plotted in Fig. B.2 for 1000 sites.

B.5 Coefficients in the Cluster Dynamics

We consider a homogeneous system of hard-core bosons at incommensurate filling ($N < L$). Using open boundary conditions, the single-particle wavefunctions are $\psi_n(x_i) = \sqrt{\frac{2}{L+1}} \sin(\frac{n x_i \pi}{L+1})$

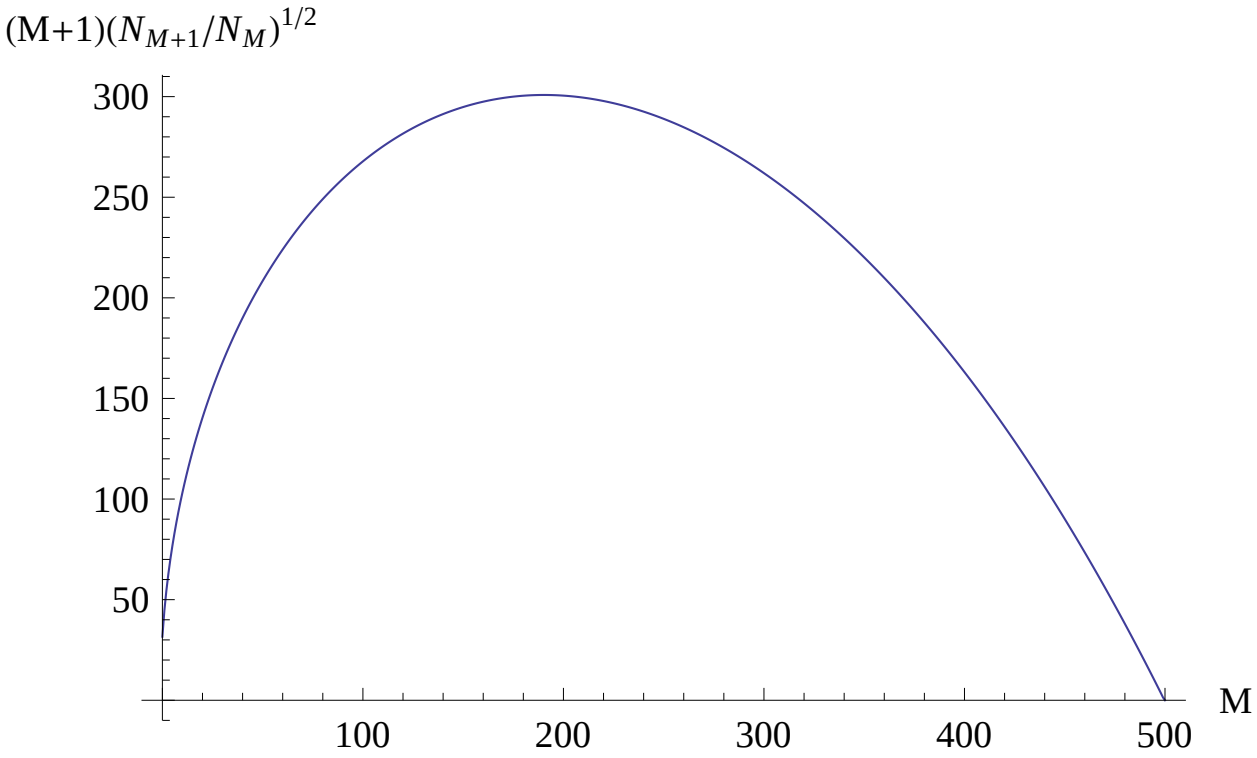

Figure B.2: Symmetric coupling for N = 1000

where $n = 1, 2, \ldots, L$. The many-body ground state then is

$$|\psi_0\rangle = \sum_{\{\vec{k}\}} \left| \det_{n,i=1}^{N} \psi_n(k_i) \right| |\vec{k}\rangle \equiv \sum_{\{\vec{k}\}} c_{\{\vec{k}\}} |\vec{k}\rangle, \tag{B.17}$$

where the sum is over all permutations of the positions of the particles $\{\vec{k}\}$ and the determinant is

$$\det_{n,i=1}^{N} \psi_n(k_i) = \begin{vmatrix} \psi_1(k_1) & \psi_1(k_2) & \ldots & \psi_1(k_N) \\ \psi_2(k_1) & \psi_2(k_2) & \ldots & \psi_2(k_N) \\ \vdots & \vdots & \ddots & \vdots \\ \psi_N(k_1) & \psi_N(k_2) & \ldots & \psi_N(k_N) \end{vmatrix}. \tag{B.18}$$

For a given $\vec{k}$, the determinant of this alternant matrix takes the form

$$\begin{aligned} \det_{n,i=1}^{N} \psi_n(k_i) &= \left(\frac{2}{L+1} \right)^{1/N} (-2)^{N(N-1)/2} \\ &\times \prod_{i<j} \left(\cos \frac{k_i \pi}{L+1} - \cos \frac{k_j \pi}{L+1} \right) \times \prod_{i=1}^{N} \sin \frac{k_i \pi}{L+1}. \end{aligned} \tag{B.19}$$

At low filling factors, Eq. (B.19) shows that particles tend not to form large clusters, validating the approximation used in Eq. (4.22). The coefficients in Eqs. (4.22) and (4.23) are then obtained as

$$c_{\{\vec{k}\}} = \left| \det_{n,i=1}^{N} \psi_n(k_i) \right|. \tag{B.20}$$

The coefficient $D_{\vec{k}}^{|n\rangle}$ defined in Sec. 4.3 is obtained numerically by taking a configuration $\vec{k}$ and counting the occurence of clusters $|n\rangle$. The n particle clusters are identified by their contiguous empty sites.

B.6 Higher-Order Resonance Processes

The previous discussion has been dedicated to first order tunneling processes for $U = \Omega$. In this section, we introduce higher-order resonant tunneling processes which occur when $U = n\Omega$ for $n > 1$. As was argued, at a first-order resonance $U = \Omega$, the dynamics from an initial Mott insulator shows that the time-evolved state remains within a resonant manifold comprised of states with doublon-hole (or "dipole") excitations. At second-order resonance ($U = 2\Omega$), the resonant manifold is comprised of a Mott insulator and those states which contain dipole excitations, where the hole is now located two sites away from the two-particle occupied site. These dipole excitations are described as being second-order tunneling processes. The spin Hamiltonian derived from the first-order resonance does not capture the second-order tunneling processes because the higher-order resonant manifold cannot be represented in the spin Hilbert space. Second-order perturbation theory is required to calculate the matrix elements of the effective Hamiltonian $\hat{H}_{\text{eff}}$ within this second-order resonant manifold. As an example, we consider the Mott state $|MI\rangle$ and a single second-order dipole state $|D\rangle$, where the dipole is located away from the edge of a finite lattice. The tunneling matrix element is

$$\langle D|\hat{H}_{\text{eff}}|MI\rangle = \langle D| \sum_m \frac{\hat{H}_J|m\rangle\langle m|\hat{H}_J}{\epsilon_{MI,D}^{(0)} - \epsilon_m^{(0)}} |MI\rangle, \tag{B.21}$$

where the sum is over the intermediate states $|m\rangle$ not equal to $|MI\rangle$ or $|D\rangle$, and $\hat{H}_J$ denotes the tunneling term in the Bose-Hubbard Hamiltonian. The matrix elements of the effective Hamiltonian

can be constructed with states which belong to the second-order resonant manifold. For instance, one can identify two intermediate channels in order to calculate the off-diagonal matrix element, $\langle D|H_{\text{eff}}|MI\rangle = -\frac{(2+\sqrt{2})J^2}{\Omega}$. Here, we set the zeroth order energy $\epsilon^{(0)}_{MI,D} = 0$. In the same vein, we can calculate all diagonal and off-diagonal matrix elements which couple each successive dipole excitation. Similar to what was done in Ch. 4, the effective Hamiltonian $\hat{H}_{\text{eff}}$ can be used to describe the dynamics when $U = 2\Omega$. As expected, the dynamics at a second-order resonance displays a time scale proportional to J^2/Ω (see Fig. B.3). We should also be aware that the second-order resonant manifold does not only consist of states with only dipole excitations: states where adjacent sites are both occupied by two particles with two adjacent unoccupied sites is also connected to $|MI\rangle$ via second-order tunneling processes. These "unwanted" states must be taken into account, which add to the complexity of the dynamics of higher-order resonances.

Similar analysis for $U = 3\Omega$ shows that doublon-hole excitations where the hole is located 3 lattice sites away from the two-particle occupied site is resonantly connected to $|MI\rangle$ via third-order tunneling processes. The dynamics of generally higher-order resonances remains an open subject.

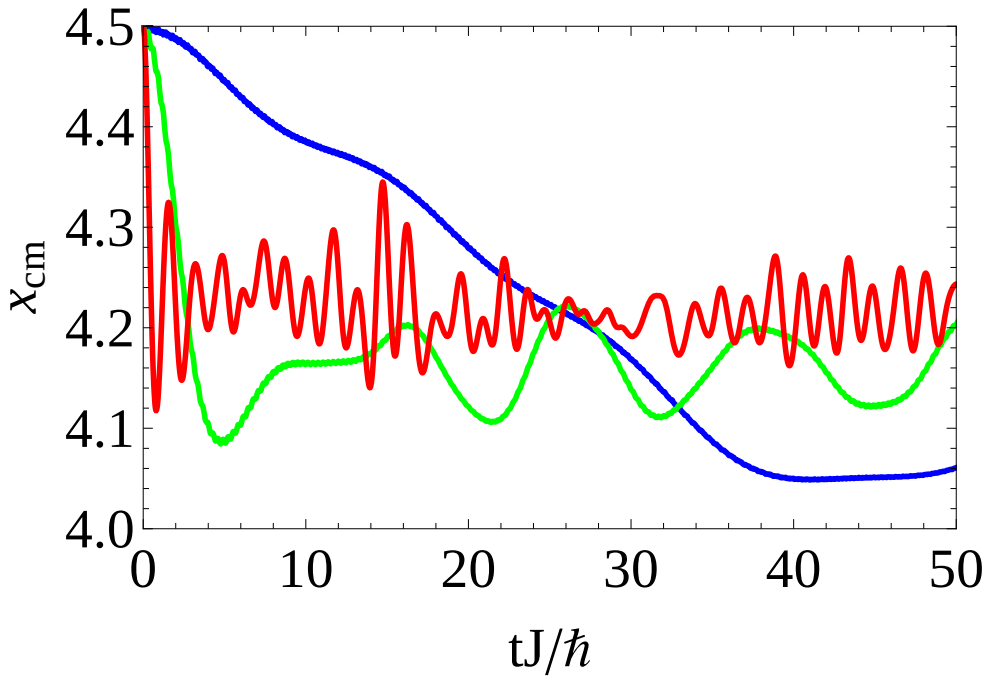

Figure B.3: CM dynamics at higher-order resonances at a system size of 8 sites: (blue) $U = 3\Omega$, (green) $U = 2\Omega$, and (red) $U = \Omega$. The dynamics was simlulated with the Bose-Hubbard Hamiltonian using adaptive t-DMRG, with a local Hilbert space of 3 particles. The parameters are $J = 1$ and $U = 40$.

Appendix C

Calculation of the Overlap Integral $A_{\nu\nu\nu'\nu'}$

We define the abbreviated notation $A_{\nu\nu\nu'\nu'} \equiv A_{\nu\nu'}$, where the quantity represents the overlap between harmonic oscillator eigenstates as shown in Eq. (6.11),

$$A_{\nu\nu'} = \int dz|\phi_0(z)|^4 \int dy|\phi_0(y)|^4 \int dx|\phi_\nu(x)|^2|\phi_{\nu'}(x)|^2. \tag{C.1}$$

Recall that the harmonic oscillator eigenfunctions are

$$\phi_\nu(x) = \Big(\frac{m\omega}{\pi\hbar 2^{2\nu}(\nu!)^2}\Big)^{1/4} e^{-\frac{m\omega x^2}{2\hbar}} H_\nu\left((\frac{m\omega}{\hbar})^{1/2}x\right), \tag{C.2}$$

where H_ν are Hermite polynomials. The result fromperforming the integral of the ground state oscillator mode is

$$\int |\phi_0(x)|^4 dx = \sqrt{\frac{m\omega}{2\pi\hbar}}. \tag{C.3}$$

Setting the oscillator length $\alpha \equiv \sqrt{m\omega/\hbar}$, the form of A reduces to,

$$A_{\nu\nu'} = \frac{\alpha^4}{2\pi^2}\Big(\frac{1}{2^{2\nu}(\nu!)^2}\Big)^{1/2}\Big(\frac{1}{2^{2\nu'}(\nu'!)^2}\Big)^{1/2} \int dx H_\nu^2(\alpha x) H_{\nu'}^2(\alpha x) e^{-2\alpha^2 x^2}. \tag{C.4}$$

In order to simplify the last integral above, we require a reduction formula for the Hermite polynomials. Using the generating function for the Hermite polynomials, $e^{-t^2+2tx} = \sum_{\nu=0}^{\infty} H_\nu(x)t^n/n!$,

$$\begin{aligned} e^{-(t_1+t_2)^2+2(t_1+t_2)x+2t_1t_2} = e^{-t_1^2+2t_1x-t_2^2+2t_2x} &= \sum_{\nu,\nu'=0}^{\infty} H_\nu(x)H_{\nu'}\frac{t_1^\nu t_2^{\nu'}}{\nu!\nu'!} \\ &= \sum_{N=0}^{\infty}\sum_{m=0}^{N}\sum_{\ell} 2^\ell H_N(x)\binom{N}{m}\frac{t_1^{N-m}t_2^m t_1^\ell t_2^\ell}{N!\ell!}. \end{aligned} \tag{C.5}$$

The above property derives the reduction formula,

$$H_\nu(x)H_{\nu'}(x) = \sum_{\ell=0}^{\min(\nu,\nu')} H_{\nu+\nu'-2\ell}(x)2^\ell \ell! \binom{\nu}{\ell}\binom{\nu'}{\ell}. \tag{C.6}$$

The last integral is evaluated using the following identity,

$$\begin{aligned}\int_{-\infty}^{\infty} dx e^{-ax^2} H_\nu(x)H_{\nu'}(x) = \\ \frac{1}{2}\Big(\frac{2}{a}\Big)^{\nu+\nu'+1}(1-a^2)^{(\nu+\nu')/2}\Gamma(\frac{\nu+\nu'+1}{2})_2\mathrm{F}_1(-\nu,-\nu';\frac{1-\nu-\nu'}{2};\frac{a^2}{2(a^2-1)}),\end{aligned} \tag{C.7}$$

where the Gamma function is defined as $\Gamma(z) = \int_0^\infty dt e^{-t}t^{z-1}$ and the Gaussian hypergeometric function is ${}_2F_1(-m,-n;\frac{1-m-n}{2};\frac{a^2}{2(a^2-1)}) = \sum_\ell^{\min(m,n)} \frac{(-m)_\ell(-n)_\ell}{\ell!(\frac{1-m-n}{2})_\ell}(\frac{a^2}{2(a^2-1)})^\ell$. The final form of $A_{\nu\nu'}$ is

$$\begin{aligned}A_{\nu\nu'} = \frac{\alpha^3}{2\pi^2 2^{\nu+\nu'}\nu!\nu'!}\times \\ \sum_{n=0}^{\nu}\sum_{m=0}^{\nu'}(-1)^{\nu+\nu'-m-n}m!n!\binom{\nu}{n}^2\binom{\nu'}{m}^2 2^{\nu+\nu'-1/2}\times \\ \Gamma(\nu+\nu'-m-n+1/2)_2F_1(2m-2\nu',2n-2\nu;\frac{1+2(\nu+\nu'-m-n)}{2};1).\end{aligned} \tag{C.8}$$